# Experimental Measurements by Antilocalization of the Interactions between Two-Dimensional Electron Systems and Magnetic Surface Species

Yao Zhang

Dissertation submitted to the Faculty of the
Virginia Polytechnic Institute and State University
in partial fulfillment of the requirements for the degree of

Doctor of Philosophy
in
Physics

Jean J. Heremans, Chair
Victoria Soghomonian
Randy Heflin
Kyungwha Park

May 5, 2014
Blacksburg, Virginia

Keywords: magnetoresistance, antilocalization, two-dimensional electron system, magnetic surface species, InAs, InGaAs, phase coherence, inelastic scattering, spin-orbit, magnetic spin-flip scatering

# Experimental Measurements by Antilocalization of the Interactions between Two-Dimensional Electron Systems and Magnetic Surface Species

Yao Zhang

(ABSTRACT)

Low-temperature weak-localization (WL) and antilocalization (AL) magnetotransport measurements are sensitive to electron interference, and thus can be used as a probe of quantum states. The spin-dependent interactions between controllable surface magnetism and itinerant electrons in a non-magnetic host provide insight for spin-based technologies, magnetic data storage and quantum information processing. This dissertation studies two different host systems, an $In_{0.53}Ga_{0.47}As$ quantum well at a distance from the surface of a heterostructure, and an accumulation layer on an InAs surface. Both the systems are two-dimensional electron systems (2DESs), and possess prominent Rashba spin-orbit interaction caused by structural inversion asymmetry, which meets the prerequisites for AL. The surface local moments influence the surrounding electrons in two ways, increasing their spin-orbit scattering, and inducing magnetic spin-flip scattering, which carries information about magnetic interactions. The two effects modify the AL signals in opposing directions: the spin-flip scattering of electrons shrinks the signal, and requires a close proximity to the species, whereas the increase of spin-orbit scattering broadens and increases the signal. Accordingly, we only observe an increase in spin-orbit scattering in the study of the interactions between ferromagnetic $Co_{0.6}Fe_{0.4}$ nanopillars and the relatively distant InGaAs quantum well. With these CoFe nanopillars, a decrease in spin decoherence time is observed, attributed to the spatially varying magnetic field from the local moments. A good agreement between the data and a theoretical calculation suggests that the CoFe nanopillars also generate an appreciable average magnetic field normal to the surface, of value $\sim 35$ G. We also performed a series of comparative AL measurements to experimentally investigate the interactions and spin-exchange between InAs surface accumulation electrons and local magnetic moments of rare earth ions $Sm^{3+}$, $Gd^{3+}$, $Ho^{3+}$, of transition metal ions $Ni^{2+}$, $Co^{2+}$, and $Fe^{3+}$, and of $Ni^{2+}$-, $Co^{2+}$-, and $Fe^{3+}$-phthalocyanines deposited on the surface. The deposited species generate magnetic scattering with magnitude dependent on their electron configurations and effective moments. Particularly for $Fe^{3+}$, the significant spin-flip scattering due to the outermost 3d

shell and the fairly high magnetic moments modifies the AL signal into a WL signal. Experiments indicate a temperature-independent magnetic spin-flip scattering for most of the species except for $Ho^{3+}$ and $Co^{2+}$. $Ho^{3+}$ yields electron spin-flip rates proportional to the square root of temperature, resulting from transitions between closely spaced energy levels of spin-orbit multiplets. In the case of $Co^{2+}$, either a spin crossover or a spin-glass system forms, and hence spin-flip rates transit between two saturation regions as temperature varies. Concerning the spin-orbit scattering rate, we observe an increase for all the species, and the increase is correlated with the effective electric fields produced by the species. In both 2DESs, the inelastic time is inversely proportional to temperature, consistent with phase decoherence via the Nyquist mechanism. Our method provides a controlled way to probe the quantum spin interactions of 2DESs, either in a quantum well, or on the surface of InAs.

# Dedication

I dedicate this dissertation work to my loving parents, Ailian and Shucun Zhang, whose support and encouragement help to build my perseverance, determination, and confidence since I was little. I also dedicate this dissertation to my wife Wenchun Wu, and my son Alexander Jiru Zhang, who give me endless support and love. I am very grateful to my family. In the past 7 years, throughout joy and pain, my family members have always stood by my side. Without them, I would not have achieved my goal. They are my power and motivation.

# Acknowledgements

I would like to express my special appreciation and thanks to my advisor Prof. Jean Joseph Heremans, he has been a tremendous mentor to me. I would like to thank him for encouraging my research and allowing me to grow as a research scientist. His advice on both research as well as on my career have been priceless. I would also like to thank my committee members, Prof. Victoria Soghomonian, Prof. Randy Heflin, and Prof. Kyungwha Park for serving as my committee members. I also want to thank them for ensuring that my defense was an enjoyable moment, and for brilliant comments and suggestions. I want to specifically single out Prof. Soghomonian, who put tremendous hard work into my Ph.D. project. She spent countless hours discussing my research, searching proper solvents, preparing sample solutions, and reviewing my papers and thesis. I am thankful to all of my lab colleagues, Dr. Raymond Kallaher, Dr. Robert Lillianfeld, Dr. Yong-Jae Kim, Dr. Martin Rudolph, Lingling Xu, Qifan Yuan, Shaola Ren, and Yuantao Xie, for the discussions we have had and the help they have provided. Over the past few years, I enjoyed studying and working in the Virginia Tech Quantum Transport Group at Department of Physics. The group is like a family, we support, cheer for, encourage, and help each other.

# Contents

# List of Figures

# List of Tables

# Chapter 1

# Introduction

## 1.1 Overview

Probing and understanding spin interactions are crucial in advancing fundamental knowledge in spin physics and paving the way for newer concepts and capabilities in technological areas such as device applications. Briefly, electronic devices are shrinking in size to maintain what the industry classifies as Moore's law, and the last decades have seen the size of the transistor shrink down to few tens of nm, with the goal of 7 nm features in the future [8]. Numerous challenges arise from the ever reducing physical sizes of these devices propelling the drive, named beyond CMOS [9], to rethink the current status of electronic devices and materials, and embark on novel materials and concepts to overcome the inherent quantum mechanical limitations that will be eventually reached with the current Si based devices. Usual electronic devices rely on the electronic charge distribution within the semiconductor that is controlled to generate logic gates. Since the gate switching and intercommunication rates limit the

device speed, efforts to improve computational power and speed have led researchers to explore the possibility of using the spin of the electron in addition to its charge as the basis of new electronic devices referred to as spintronics [10]. This thesis investigates spins in semiconductor systems and their interactions with local moments to further understanding in the field of spintronics.

Quantum interference of electrons in low temperature electronic transport leads to the phenomena of antilocalization (AL) [11, 12, 13] and weak-localization (WL) [12, 13]. Thus quantum properties of surface states may be probed by WL and AL measurements of interactions between localized surface spins and itinerant carriers [14, 15, 16, 17]. Modified magnetic and transport properties due to surface moments allow access to the fundamental parameters of spintronics and quantum information processing. Antilocalization measurements on metallic surfaces of bulk materials are reported [12, 18, 19, 20, 14, 15, 21], demonstrating the potential of this quantum interference spectroscopic probe. In this dissertation, we use more sensitive and controlled (InAs surface) and controllable (InGaAs heterostructures with buried quantum wells) two-dimensional electron systems (2DESs), allowing us to extract detailed information regarding the various contributions to the quantum decoherence of electron systems due to their interactions with neighboring spin systems. Surfaces states and consequently methods of probing surface states are of great fundamental and technological importance, with relevance ranging from topological insulators to semiconductors for beyond CMOS applications [22, 9, 23].

Quantum interference measurements convey information about the quantum coherence of the electron system under study. Electron waves possess both spin and orbital components. Decoherence of electron waves, due to their interaction with their environment influences both components via different scattering mechanisms each characterized by a decoherence

or scattering time $\tau$. Scattering times that influence the spin component are the spin-flip time $\tau_s$ and the spin-orbit time $\tau_{SO}$. The spin-orbit decoherence time enters the expression we use in our analysis quite differently than the spin-flip time (Section 1.4). The inelastic scattering time $\tau_i$ relates to the orbital component. All times, $\tau_s$, $\tau_{SO}$, and $\tau_i$ are lowered by the environment and interactions of the electron system with their environment. These interactions with the environment give rise to scattering rates, a spin-flip rate $\tau_s^{-1}$, a spin-orbit rate $\tau_{SO}^{-1}$, and an orbital or quantum phase decoherence rate $\tau_i^{-1}$. The presence and contributions of these various scattering rates may be extracted from low temperature localization experiments, AL or WL, each with its characteristic signature in the measured magnetoresistance data.When the spin-orbit scattering is non-existent, i.e. $\tau_{SO} \to \infty$, resulting in $\tau_{SO}^{-1} = 0$, WL is observed. In spin-orbit coupling materials, $\tau_{SO}^{-1} \neq 0$, and then AL is observed. Thus localization measurements provide a sensitive tool to probe various decoherence mechanisms. These decoherence mechanisms carry information about the interaction of electron systems with neighboring spins.

## 1.2 Two Dimensional Electron Systems

The itinerant carrier systems in this dissertation are 2DESs, either found at the surface of the III-V semiconductor InAs or as a quantum well (QW) in a III-V semiconductor InGaAs heterostructure. The local surface spins arise from rare earth ions, transition metal ions or magnetic $Co_{0.6}Fe_{0.4}$ nanopillars deposited on the surface or at close proximity to the 2DESs. Thus we obtain tunable artificial structures of magnetic moments on a reduced-dimensionality electron system wherein we probe quantum interference effects via AL or WL.

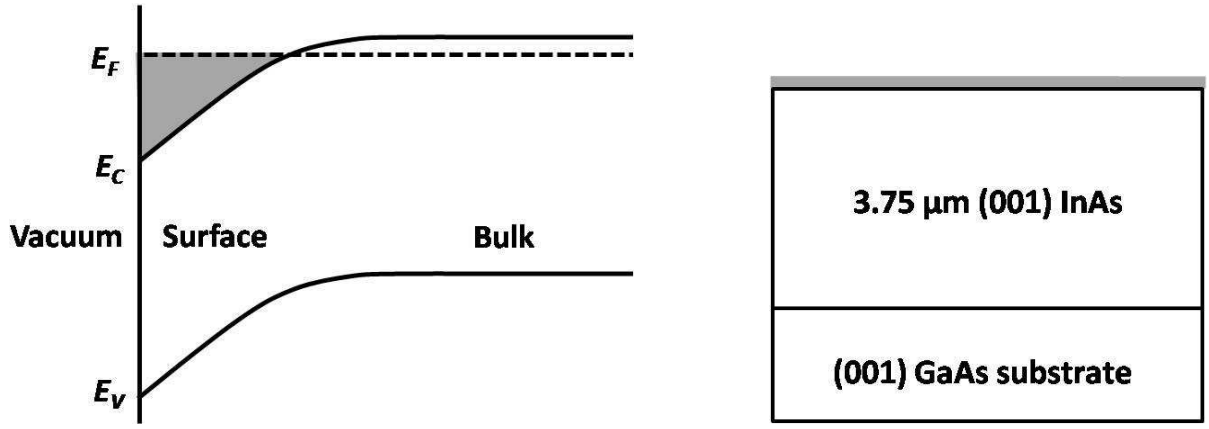


(a) (b)

Figure 1.1: (a) Schematic band structure at the surface of $n$-type InAs. Fermi level is above the conduction band at the surface but within the band gap in the bulk. The shaded area is the accumulation layer. (b) Schematic of the InAs structures.

Rare earth ions [24, 6], transition metal ions and transition metal phthalocyanine solutions deposited on the surface of InAs films induce magnetic spin-flip scatterings, indicating spin-exchange interactions of the local moments with the two-dimensional surface accumulation electron layer. We tune the interaction between surface species and the 2DES in a more controlled geometry, between lithographically delineated CoFe nanopillars on the surface of an $In_{0.53}Ga0.47As/In_{0.52}Al_{0.48}As$ heterostructure and the 2DES quantum well located about one Fermi wavelength below the surface [4]. By increasing the separation between the magnetic moments and the nonmagnetic host we expect to weaken the magnetic spin-flip scattering so observed by quantum interferometry.

It is well established that at the surfaces of InAs the Fermi level $E_F$ is pinned above the conduction band, forming a surface electron accumulation layer and hence a 2DES at the surface, as shown in Fig. 1.1(a) [25, 26, 27, 28, 29, 30]. Our experiments require electrons in close proximity to the local moments, satisfied by the InAs surface 2DES. We also note that the InAs surface 2DES has substantial Rashba SOI [31]. The InAs samples where grown on (001) GaAs substrates by metal organic vapor chemical deposition (MOCVD), with a 3.75

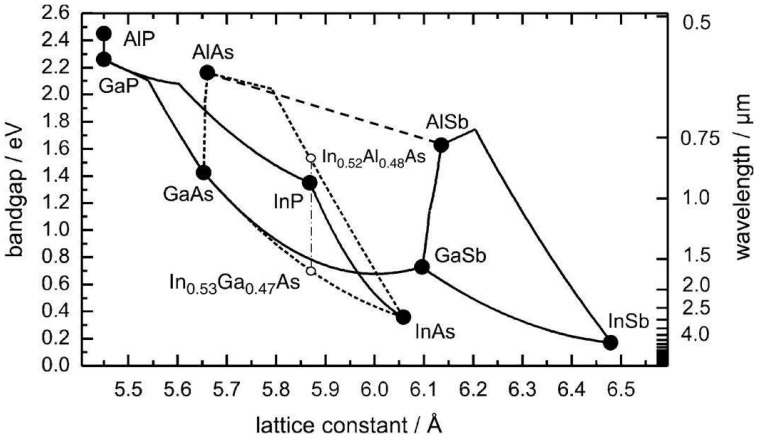


Figure 1.2: Band gap and lattice constant for various III–V compound semiconductors (solid line: direct band gap; broken line: indirect band gap; dotted vertical line between InGaAs and InP/InAlAs: lattice-matched quaternary compositions) (Ref. [1]).

$\mu$m thick InAs layer as shown in Fig. 1.1(b). The location of the Fermi level, above the conduction band minimum due to donor-like surface states forming the 2DES at the surface, yet below the conduction band in the bulk, results in two type of carries, surface and bulk. The InAs films are unintentionally doped with the bulk behaving as a degenerate $n$-type semiconductor, a conduction layer parallel to the surface 2DES conducting layer. Thus, a simple Hall measurement is not adequate to determine the carrier density. To differentiate between these two types of electrons, a two-band analysis is required [32, 33], which is described in Section 1.3.

The 2DES in the case of InAs is at the surface, and these surface electrons interact with surface species. The interaction is distance dependent, and in order to increase the distance between a 2DES and surface species, a quantum well within a heterostructure is used. Heterostructures are grown by properly selecting materials with different band gaps, and where the band offsets at specific interfaces form quantum wells, and hence a 2DES. In Fig. 1.2, the band gap and lattice constants of some binary and tertiary III-V semiconductors are depicted. To grow high crystal quality heterostructures, substitutions into the binary sys-

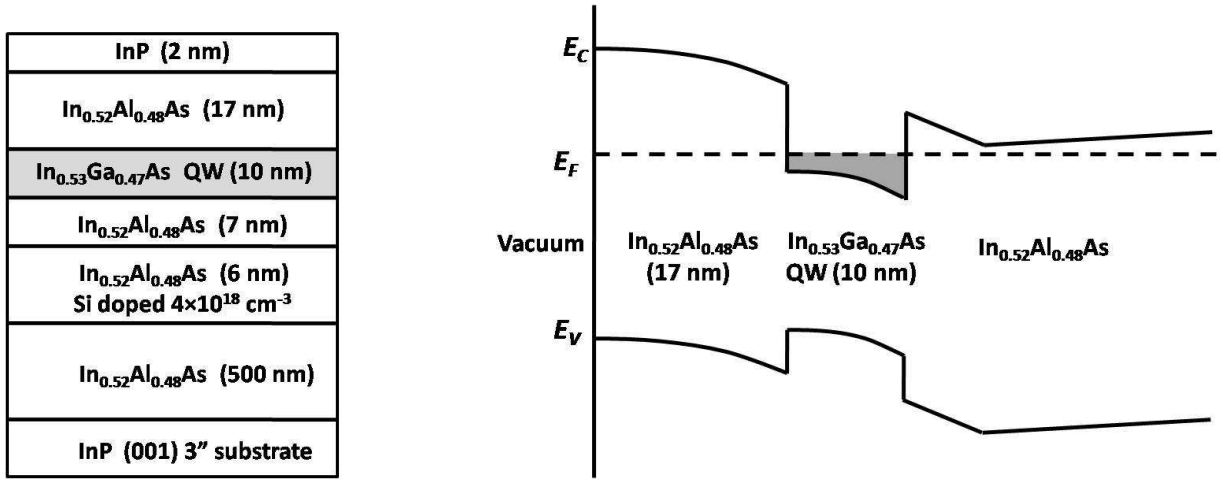


(a) (b)

Figure 1.3: (a) Schematic of the InGaAs/InAlAs heterostructure, with the quantum well (shaded) located 19 nm below the surface. (b) Schematic band structure of $In_{0.53}Ga_{0.47}As$ quantum well. The shaded area is the 2DES.

tems to yield tertiary and quaternary systems is feasible, as long lattice mismatches are less than 1% between adjacent layers. The InGaAs/InAlAs heterostructure used in this dissertation was purchased from IQE [34] and was grown by molecular beam epitaxy (MBE), and a schematic of the structure is shown in Fig. 1.3(a). The heterostructure consists of a 500 nm $In_{0.52}Al_{0.48}As$ buffer, a 6 nm $In_{0.52}Al_{0.48}As$ doping layer, a 7 nm $In_{0.52}Al_{0.48}As$ layer, the 10 nm wide $In_{0.53}Ga_{0.47}As$ quantum well, a 17 nm $In_{0.52}Al_{0.48}As$ layer, and a 2 nm undoped InP cap layer. The band structure and the confined quantum well sandwiched between two $In_{0.52}Al_{0.48}As$ layers are shown in Fig. 1.3(b). While InAs is best described with a two-band model, the quantum well in $In_{0.53}Ga_{0.47}As$ heterostructure is a single carrier system, and will be treated as such in our analyses. Using a quantum well at specific distances below the surface, i.e. different heterostructures, allows us to study interactions of electron systems with surface spins at controlled distances. This in turn allows us to extract detailed information regarding the various contributions to the quantum decoherence of electron systems due to their interactions with neighboring spin systems as a function of distance.

## 1.3 Two-Band Analysis

Two-band analysis is a valuable technique that allows one to quantify the carrier mobilities and densities where there are two parallel conducting channels [32, 33]. Experimentally, the Hall coefficient ($\rho_{XY}$) and the resistivity ($\rho_{XX}$) are measured as a function of the varying magnetic field. The $\rho_{XX}$ and $\rho_{XY}$ together form the resistivity tensor $\hat{\boldsymbol{\rho}}$, which is defined in the classical Drude model as $\boldsymbol{E} = \hat{\boldsymbol{\rho}} \cdot \boldsymbol{J}$ with $\boldsymbol{E}$ and $\boldsymbol{J}$ being electric field and current density. In a single-band system $\hat{\boldsymbol{\rho}}$ can be expressed as

$$\hat{\boldsymbol{\rho}} = \begin{pmatrix} \rho_{XX} & \rho_{XY} \\ -\rho_{XY} & \rho_{XX} \end{pmatrix} = \frac{1}{ne\mu} \begin{pmatrix} 1 & \mu B \\ -\mu B & 1 \end{pmatrix}, \tag{1.1}$$

where $n$, $\mu$, $e$ and $B$ are carrier density, carrier mobility, electron charge, and magnetic field respectively. In Eq. 1.1, we have $\frac{1}{ne\mu} = \rho_{XX}(B = 0)$. For a single-band system, the longitudinal magnetoresistance (diagonal terms in Eq. 1.1) is $B$ independent, and the transverse magnetoresistance (Hall signal) is proportional to $B$. Thus no classical correction to the magnetoresistance MR needs to be considered. However, InAs, when there are two bands, as in the case of where both the surface and the bulk electrons contribute to the conductivity during the transport, the expressions change. The conductivity tensor $\hat{\boldsymbol{\sigma}}$ is the inverse of $\hat{\boldsymbol{\rho}}$, and can be extracted by [35]

$$\begin{cases} \sigma_{XX} = \sigma_{YY} = \dfrac{\rho_{XX}}{\rho_{XX}^2 + \rho_{XY}^2} \\ \sigma_{XY} = -\sigma_{YX} = -\dfrac{\rho_{XY}}{\rho_{XX}^2 + \rho_{XY}^2} \end{cases}. \tag{1.2}$$

There are two different sets of electronic transport parameters in our two-band system, which are: surface mobility $\mu_s$, surface density $n_s$, bulk mobility $\mu_b$, and bulk density $n_b$.

The components of the conductivity tensor are related to the surface and the bulk electrons as in [33]

$$\begin{cases} \sigma_{XX} = \dfrac{n_s e\mu_s}{1+\mu_s^2 B^2} + \dfrac{n_b e\mu_b}{1+\mu_b^2 B^2} \\ \sigma_{XY} = -\dfrac{n_s e\mu_s^2 B}{1+\mu_s^2 B^2} - \dfrac{n_b e\mu_b^2 B}{1+\mu_b^2 B^2} \end{cases} . \tag{1.3}$$

The two-band model can be extended to more than two carriers with varied charges by introducing more conducting channels in the summation,

$$\begin{cases} \sigma_{XX} = \sum\limits_i \dfrac{n_i q_i \mu_i}{1+\mu_i^2 B^2} \\ \sigma_{XY} = -\sum\limits_i \dfrac{n_i q_i \mu_i^2 B}{1+\mu_i^2 B^2} \end{cases} (i = 1, 2, 3, ..., N), \tag{1.4}$$

where $n_i$, $q_i$, $\mu_i$ are the sheet density, charge, and mobility corresponding to the $i$th carrier [33]. Thus $\rho_{XX}$ and $\rho_{XY}$ can be determined by $\mu_s$, $n_s$, $\mu_b$, and $n_b$ as

$$\begin{cases} \rho_{XX} = \dfrac{n_s\mu_s + n_b\mu_b + \mu_s\mu_b(n_s\mu_b + n_b\mu_s)B^2}{e[(n_s\mu_s + n_b\mu_b)^2 + (n_s+n_b)^2(\mu_s\mu_b B)^2]} \\ \rho_{XY} = \dfrac{[n_s\mu_s^2 + n_b\mu_b^2 + \mu_s^2\mu_b^2(n_s+n_b)B^2]B}{e[(n_s\mu_s + n_b\mu_b)^2 + (n_s+n_b)^2(\mu_s\mu_b B)^2]} \end{cases} . \tag{1.5}$$

The expression of $\rho_{XX}$ in Eq. 1.5 indicates a parabolic background in $B$ at low fields, which will be subtracted from the MR to analyse the antilocalization signal. The two-band analysis is the only classical correction to the MR applied in this dissertation. By fitting experiment data to Eq. 1.5, one can obtain the carrier parameters $\mu_s$, $n_s$, $\mu_b$, and $n_b$. Often the transport contributions from the two carriers cannot be distinguished. Later in this chapter, a self-consistent calculation is introduced to discern the surface and the bulk electrons of InAs films.

## 1.4 Weak Localization and Antilocalization

### 1.4.1 Weak Localization

In a disordered metal-like system, the Drude theory yields the conductivity $\sigma = ne^2\tau_0/m_e$, where $\tau_0$ and $m_e$ are the elastic scattering time and the electron mass. Here $\tau_0$ can be interpreted as the lifetime of the electron in the eigenstate of momentum, which is determined by the stationary impurities and is temperature independent. However, at cryogenic temperatures, a decrease in conductivity due to quantum corrections in the electron diffusive movement is experimentally observed [36]. The Boltzmann theory assumes $\tau_0$ is long enough to destroy the correlations between different diffusive paths, thus the momentum of an electron decays exponentially after $\tau_0$, just as the Drude equation depicts. However, this is not quite correct when an electron still maintains its phase coherence after several elastic scatterings. From quantum mechanics, the phase of an electron wave is determined by the energy, thus we introduce the life time of the electron in an eigenstate of energy, defined as the inelastic scattering time $\tau_i$. At low temperatures, we can have $\tau_0$ several orders of magnitude smaller than $\tau_i$, indicating that a conduction electron can be scattered by impurities without loosing its phase coherence. During the diffusion process, there are many different possible diffusive trajectories for an electron to take due to random impurity scatterings. Regarding the correlations between these trajectories, quantum interference corrections to the Drude results have to be considered, which can explain the anomalous decrease in conductivity observed experimentally.

The quantum interferences result in enhancing the probability for back-scattering of the electron wave, known as weak-localization (WL). Considering the interference of the probability amplitudes $A_i$ for the Feynman paths from one point $r$ to another point $r'$ in a time $t$, the

probability $P(r, r', t)$ can be written as [2]

$$P(r, r', t) = \left| \sum_i A_i \right|^2 = \sum_i |A_i|^2 + \sum_{i \neq j} A_i A_j^*. \tag{1.6}$$

The first term on the right hand side of the Eq. 1.6 is the diffusion probability in Drude theory. The second term corresponds to the correlations between different paths. When the beginning ($r$) and the end ($r'$) points are different (Fig. 1.4a), the large number of the different trajectories average out the interference term due to lack of correlated phases. However, when $r$ and $r'$ overlaps with each other (Fig. 1.4b), the electron wave propagate either clockwise or counter-clockwise around the closed loop, and these two time-reversed paths interfere with each other. If time consumed before returning to the departing point of the loop $t < \tau_i$, the electron wave of the two paths are phase coherent, and the back-scattering probability is $P = |A^+ + A^-|^2$, where $A^+$ and $A^-$ are probability amplitudes for clockwise and counter-clockwise propagation. Since the two paths are identical except that the propagation direction is reversed, we have $A^+ = A^- = A$. Thus, the back-scattering probability is $4|A|^2$, which is twice the result of incoherent scattering when $t > \tau_i$. The enhanced probability of returning to the incident point of the loop may be interpreted as the electron being more likely to be localized, thus reducing the conductivity, which is the essence of WL. As phrased by Chakravarty and Schmid [37], "it is one of those unique cases where the superposition principle of quantum mechanics leads to observable consequences at the macroscopic level."

We now derive approximate but physically transparent quantitative expressions for WL. At the end of this paragraph a more rigorous expression is given. In two dimensions, the energy of an electron can be written as $E = \dfrac{\hbar^2}{2m}\left(k_x^2 + k_y^2\right)$, where $\hbar$ and $k_i$ $(i = x, y)$ are Planck constant and wavevector respectively. The criterion for a two-dimensional (2D) WL is that

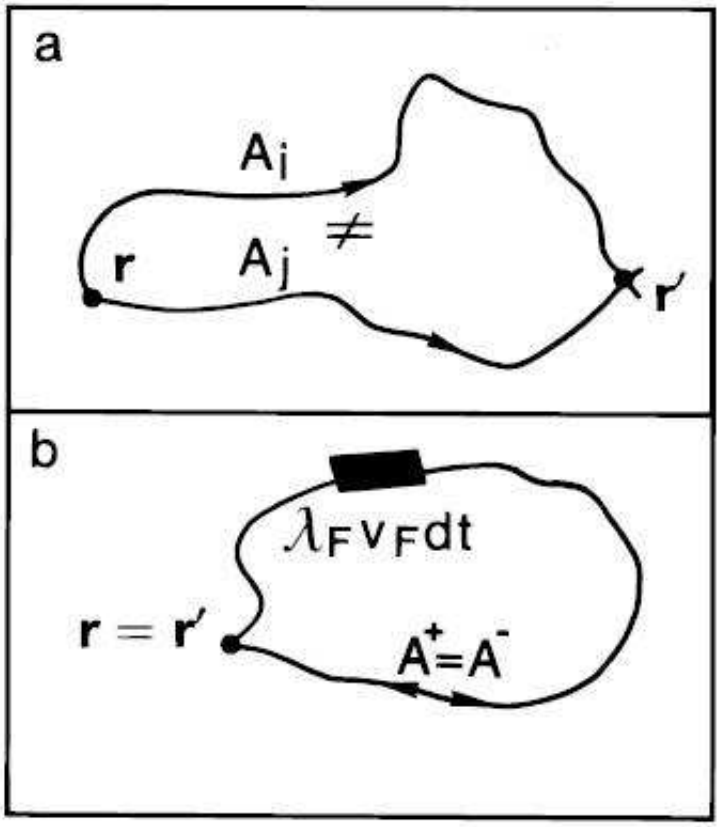


Figure 1.4: Schematic of coherent back-scattering. (a) The starting point $r$ and the end point $r'$ are separated, the probability amplitudes $A_i$ and $A_j$ of two trajectories between them are uncorrelated. (b) When $r$ and $r'$ coincide, the amplitudes $A^+$ and $A^-$ of two time-reversed paths are equal and add coherently, thus the probability for return to the origin is twice as great as in classical diffusion. (Ref. [2]).

the phase coherence length $l_\phi$ is much smaller than both the conducting channel length $L$ and width $W$. When an external magnetic field is not present, $l_\phi$ simply equals the inelastic coherence length $l_i = \sqrt{D\tau_i}$, where $D$ is the diffusion constant. The theoretical expression for the 2D WL conductance is derived as [38, 39]

$$\delta\sigma = -\frac{2e^2}{\pi\hbar}\frac{1}{LW}\sum_{k_x}\sum_{k_y}\frac{1}{k_x^2 + k_y^2 + 1/l_i^2}. \tag{1.7}$$

Equation 1.7 can be modified into the following integral

$$\delta\sigma = -\frac{2e^2}{\pi\hbar}\frac{1}{LW}\iint_{-\infty}^{+\infty}\frac{dk_x dk_y}{4\pi^2}\frac{LW}{k_x^2 + k_y^2 + 1/l_i^2} = -\frac{2e^2}{\pi\hbar}\frac{1}{4\pi^2}\int_0^{1/l}\frac{2\pi k dk}{k^2 + 1/l_i^2}, \tag{1.8}$$

where $l$ is the short-time cutoff length for diffusive motion. We evaluate the expression in Eq. 1.8 by choosing the upper limit of $l$ (in the integral) as the elastic decoherence length $l_0$, which is defined as $l_0 = \sqrt{D\tau_0}$. The expression for $\delta\sigma$ is then reduced to $\delta\sigma = -\frac{e^2}{2\pi^2\hbar} ln\left(\frac{\tau_i}{\tau_0} + 1\right)$ [40].

Often $\tau_0 \ll \tau_i$, thus we have [41]

$$\delta\sigma = -\frac{e^2}{2\pi^2\hbar} ln\left(\frac{\tau_i}{\tau_0}\right). \tag{1.9}$$

The relative phase of the two interfering waves is influenced by an external magnetic field as demonstrated in Fig. 1.5. The time-reversed symmetry of the closed path is broken, thus the resistance enhancement due to WL is suppressed. The canonical momentum of an electron in $B$ contains a potential vector $\boldsymbol{A}$ in the form of $\boldsymbol{p} = m\boldsymbol{v} + e\boldsymbol{A}$, where $m\boldsymbol{v}$ is the kinetic momentum and will cancel out over the path integral in Eq. 1.10. The phase difference

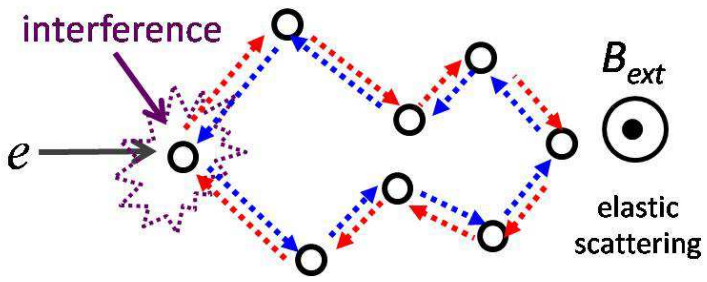


Figure 1.5: Diffusion paths of the conduction electron in a disordered system with an external magnetic field applied normal to the 2DES. The electron wave propagates clockwise or counter-clockwise through elastic scatterings, and in the case of quantum diffusion, returns to the origin before losing the phase coherence.

developed between clockwise (+) and counter-clockwise (–) paths is [42]

$$\delta\phi = \hbar^{-1}\oint_{+} \boldsymbol{p}\cdot d\boldsymbol{l} - \hbar^{-1}\oint_{-} \boldsymbol{p}\cdot d\boldsymbol{l} = \frac{2e}{\hbar}\int (\bigtriangledown \times \boldsymbol{A})\cdot d\boldsymbol{S} = \frac{2eBS}{\hbar} = \frac{2e}{\hbar}\Phi, \tag{1.10}$$

where $S$ and $\Phi$ are the area of the time-reversed path and the magnetic flux. On average, the constructive and the destructive interferences cancel each other when the phase shift exceeds 1 in radian, namely the loops with area $S > \dfrac{\hbar}{2eB}$ no longer contribute to the back-scattering. The effect of $B$ is essentially to introduce a long-time cutoff length to obtain smallest $k$ value in the expression of Eq. 1.8. The sum of the area $S$ enclosed by the two time-reversed paths on a time scale of magnetic relaxation time $\tau_B$ is then $S = 2D\tau_B$. The criteria $\delta\phi = 1$ requires $\tau_B = \dfrac{\hbar}{4eDB}$. Magnetic length $l_B = D\tau_B$ is chosen as the long-time cutoff length, thus the result of the Eq. 1.8 becomes $\delta\sigma = -\dfrac{e^2}{2\pi^2\hbar} ln\left(\dfrac{\tau_B}{\tau_0}\right)$ when $\tau_0 \ll \tau_i$ and $\tau_B \ll \tau_i$. Compared with Eq. 1.9, $B$ begins to have a significant effect on WL if $\tau_B > \tau_i$ because the coherence is lost and the MR disappears. Thus a more precise expression for $\delta\sigma$ when $B$ is present can be derived from Eq. 1.9 as

$$\delta\sigma(B) = -\frac{e^2}{2\pi^2\hbar}\left[ln\left(\frac{\tau_B}{\tau_0}\right) - ln\left(\frac{\tau_B}{\tau_i}\right)\right]. \tag{1.11}$$

Since $B$ introduces a time $\tau_B$ into the electron system, other characteristic times $\tau_\alpha$ ($\alpha = 0, i$) can be expressed in terms of characteristic magnetic fields $B_\alpha$, where $\tau_\alpha B_\alpha = \dfrac{\hbar}{4eD}$. The exact formula for magnetoconductance is derived in [43, 11]

$$\delta\sigma(B) = -\frac{e^2}{2\pi^2\hbar}\left[\Psi\left(\frac{1}{2}+\frac{B_0}{|B|}\right) - \Psi\left(\frac{1}{2}+\frac{B_i}{|B|}\right)\right], \tag{1.12}$$

where $\Psi(x)$ is the digamma function, and $\lim\limits_{x\to\infty}\Psi\left(\dfrac{1}{2}+x\right) = ln(x)$. When $B \to 0$, we have $\delta\sigma(B=0) = -\dfrac{e^2}{2\pi^2\hbar}\left[ln\left(\dfrac{B_0}{|B|}\right) - ln\left(\dfrac{B_0}{|B|}\right)\right] = -\dfrac{e^2}{2\pi^2\hbar}ln\left(\dfrac{B_0}{B_i}\right) = -\dfrac{e^2}{2\pi^2\hbar}ln\left(\dfrac{\tau_i}{\tau_0}\right)$, which is Eq. 1.9. The full expression for the quantum corrections to the 2D magnetoconductance $\sigma_2$ due to WL is defined as [44]

$$\Delta\sigma_2(B) = \delta\sigma(B) - \delta\sigma(B=0) = -\frac{e^2}{2\pi^2\hbar}\left[F\left(\frac{B_0}{|B|}\right) - F\left(\frac{B_i}{|B|}\right)\right], \tag{1.13}$$

where $F(x)$ is given by $F(x) = \Psi\left(\dfrac{1}{2}+|x|\right) - ln(|x|)$.

### 1.4.2 Antilocalization

So far, we have mainly considered the spatial part of the wave amplitude of the conduction electrons and neglected their spin component. In fact, the self-interference of an electron wave function travelling along time-reversed paths is sensitive to both spin-orbit scattering $\tau_{SO}^{-1}$ and spin-flip scattering $\tau_s^{-1}$. In materials with only spin-orbit coupling and without magnetic impurities, when we consider a closed transport path, spin-orbit interaction (SOI) involves an effective magnetic field which induces a momentum-dependent spin precession. Neutron experiments on spin 1/2 particles have a rotational periodicity of $4\pi$ [45]. The relative rotation of the spins is $2\pi$ for an electron wave demonstrated when moving along the

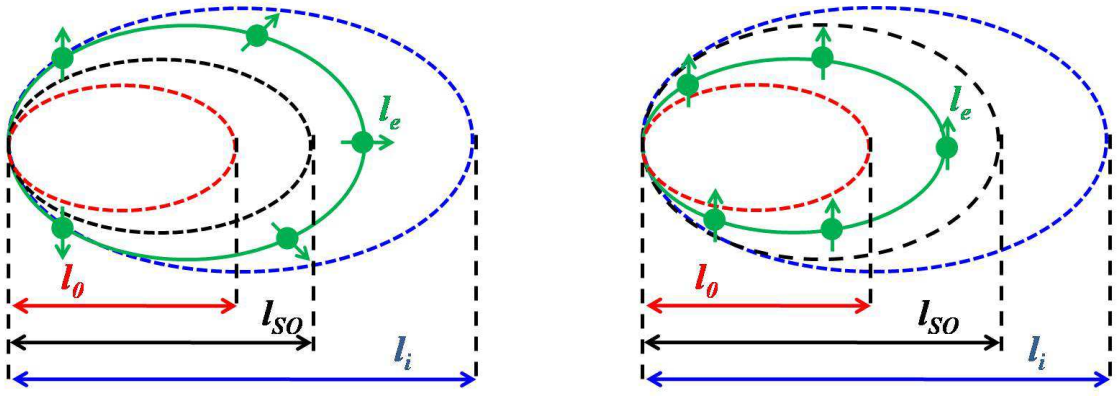


Figure 1.6: Schematic of characteristic length scales for the closed transport paths in (a) AL and (b) WL. $l_0 = \sqrt{D\tau_0}$, $l_i = \sqrt{D\tau_i}$, and $l_{SO} = \sqrt{D\tau_{SO}}$.

closed path. This oppositely shifted spin phase leads to a destructive interference between two probability amplitudes, which reduces the back-scattering probability to below $2|A|^2$. Hikami *et al* [11] pointed out that the SOI should reverse the sign of the correction to the resistivity and reduce its magnitude by a factor of 1/2, leading to antilocalization (AL). Figure 1.6 illustrates the origins of WL and AL by correlating characteristic time scales with length scales [42], where $l_0 = \sqrt{D\tau_0}$ describes the characteristic length relevant to the available minimum closed path for electron back-scattering, $l_i = \sqrt{D\tau_i}$ is the maximum closed path for the electron to avoid inelastic phase breaking, $l_{SO} = \sqrt{D\tau_{SO}}$ describes the spin phase shift on the order of $\pi$ caused by the effective magnetic field of the SOI, and $l_e$ is the length scale of the electron back-scattering. When $l_i > l_e > l_{SO}$ (Fig. 1.6(a)), destructive interference arises due to difference of $\pi$ in the spin phase, resulting in AL. However, in the case of $l_{SO} > l_e > l_0$ (Fig. 1.6(b)), where the SOI is weak, the back-scattering path is too short for the electron spin to acquire substantial phase. As a result, constructive interference at the incident point causes WL. Moreover, if we introduce magnetic spin-flip scatterings in Fig. 1.6(a), the spin phase length is increased because the spin-orbit scattering will be partially screened by the spin-flip rate. Accordingly, the AL signal will be suppressed. As

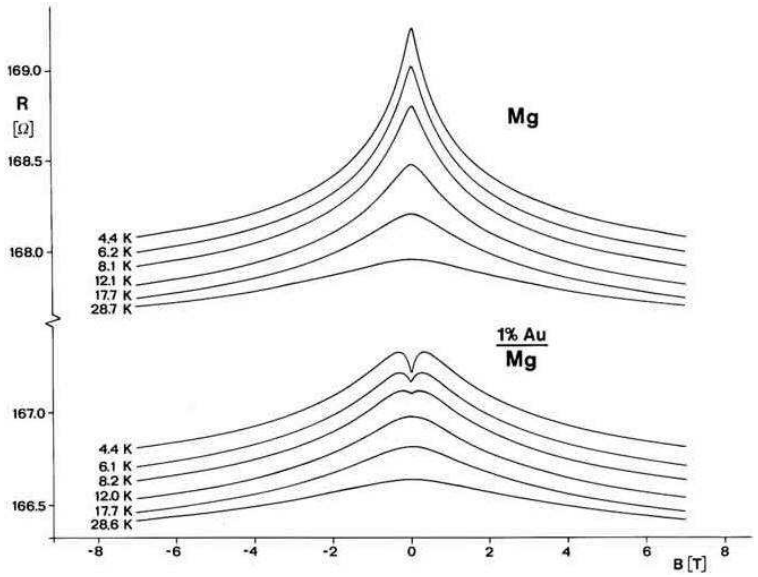


Figure 1.7: Experimental result of weak-localization in a thin Mg film (upper part). An increased resistance and a negative magnetoresistance are observed at low temperatures. With one atomic percent of surface layer being covered by Au on the same Mg film, a pronounced spin-orbit scattering is introduced and an antilocalization signal with a positive magnetoresistence at small fields is observed. (Ref. [3]).

$l_{SO}$ keep increasing untill $l_{SO} > l_e$ (Fig. 1.6(b)), then the AL signal changes to WL.

Early experiments by Bergmann [12] performed on metal films showed AL characterized by a dip, around zero applied magnetic filed, in the resistance traces when compared to WL traces. Fig. 1.7 [12] shows WL behavior of a Mg film. Mg is a light element and thus induces small spin-orbit interaction. With a few atomic percent of the surface layer being covered by Au, a heavy element with strong spin-orbit coupling, significant changes to the MR are caused as indicated in Fig. 1.7. The value of $\tau_{SO}^{-1}$ is a measure of the influence of the SOI, and in the presence of Au on Mg, the WL signal changes to AL under applied external magnetic field. When a weak external magnetic field is applied and $l_i > l_B > l_{SO}$, destructive interference due to the spin phase difference is destroyed by $B$, and MR becomes positive. In contrast, in a large external magnetic field where $l_B < l_{SO}$, the relative spin phase is almost unchanged and the constructive interference yields the usual negative magnetoresistance. For $l_B \approx l_{SO}$,

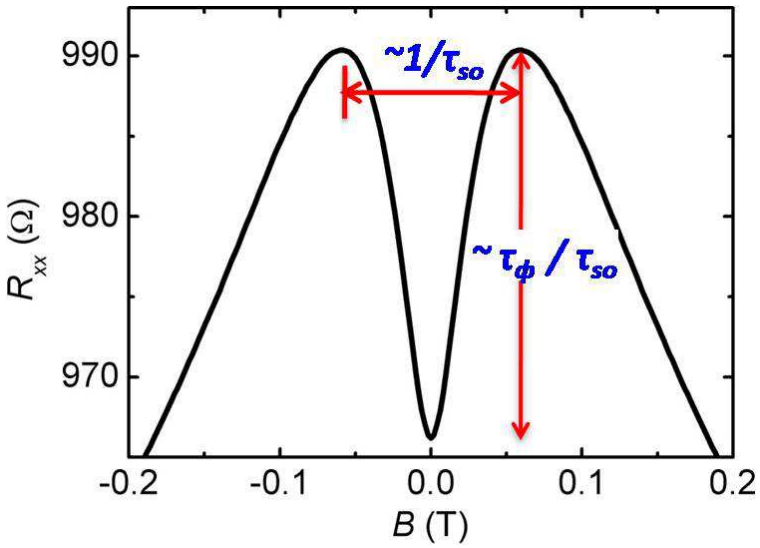


Figure 1.8: Schematic graph of a typical antilocalization signal. The longitudinal resistance $R_{XX}$ is dependent on $B$, and the shape of the curve is sensitive to $\tau_{SO}$ and phase coherence time $\tau_\phi$.

the MR changes sign and reaches local maxima, which explains the MR curve for 1% Au on top of Mg in Fig. 1.7.

A typical MR curve showing AL is depicted in Fig. 1.8. The separation in $B$ between two resistance maxima scales with $\tau_{SO}^{-1}$, while the depth of the resistance minimum scales with the ratio $\tau_\phi/\tau_{SO}$, where $\tau_\phi$ is the phase coherence time and $\tau_\phi = \tau_i$ when there are no magnetic impurities present.

In the presence of SOI, considering the spin states of the two interfering electron waves, their contribution to the coherent back-scattering can be expressed in cooperons. Applying the quantum notation $|s\ m\rangle$ with $s$ and $m$ being spin quantum number and secondary spin quantum number, a cooperon has a singlet state ($|0\ 0\rangle$) and three triplet states ($|1\ 1\rangle$, $|1\ 0\rangle$,

and $|1\ {-1}\rangle$). The characteristic singlet and triplet fields are [46]

$$\begin{aligned} B_{00} &= B_\phi \\ B_{11} &= B_{1\text{–}1} = B_\phi + B_{SO} \\ B_{10} &= B_\phi + 2B_{SO}, \end{aligned} \tag{1.14}$$

where $B_{SO} = \dfrac{\hbar}{4eD\tau_{SO}}$. The quantum corrections to the 2D magnetoconductance $\sigma_2$ due to AL is defined as [11]

$$\Delta\sigma_2(B) = -\frac{e^2}{2\pi^2\hbar}\left\{F\left(\frac{B_0}{|B|}\right) - \frac{1}{2}\left[F\left(\frac{B_{11}}{|B|}\right) + F\left(\frac{B_{10}}{|B|}\right) + F\left(\frac{B_{1\text{–}1}}{|B|}\right)\right] + \frac{1}{2}F\left(\frac{B_{00}}{|B|}\right)\right\}, \tag{1.15}$$

which is reduced to Eq. 1.13 when SOI is weak, so $B_{SO} = 0$.

Of particular interest in this dissertation is the application of AL in the determination of magnetic scattering by magnetic impurities. The magnetic impurities introduce an interaction with conduction electrons and scatter two complementary electron waves differently and destroy their coherence after a spin-flip scattering time $\tau_s$, and thus at fields, the quantum interference is greatly suppressed due to finite magnetic spin-flip scattering. In the presence of magnetic impurities, the phase coherence time is defined as $\tau_\phi^{-1} = \tau_i^{-1} + 2\tau_s^{-1}$ [47, 48], and $\tau_{SO}$ is replaced by $(\tau_{SO}^{-1} - \tau_s^{-1})^{-1}$ [48]. The expression applied in this work for $\Delta\sigma_2(B)$

is then obtained as [11, 46, 24, 6, 4, 5]

$$\Delta\sigma_2(B) = -\frac{e^2}{2\pi^2\hbar}\left\{\left[\Psi\left(\frac{1}{2}+\frac{B_0}{|B|}\right)-\Psi\left(\frac{1}{2}+\frac{B_i+B_{SO}+B_s}{|B|}\right)+\frac{1}{2}\Psi\left(\frac{1}{2}+\frac{B_i+2B_s}{|B|}\right)\right.\right.$$

$$\left.-\frac{1}{2}\Psi\left(\frac{1}{2}+\frac{B_i+2B_{SO}}{|B|}\right)\right]-\left[ln\left(\frac{B_0}{|B|}\right)-ln\left(\frac{B_i+B_{SO}+B_s}{|B|}\right)\right.$$

$$\left.\left.+\frac{1}{2}ln\left(\frac{B_i+2B_s}{|B|}\right)-\frac{1}{2}ln\left(\frac{B_i+2B_{SO}}{|B|}\right)\right]\right\} \tag{1.16}$$

with $B_s = \dfrac{\hbar}{4eD\tau_s}$. $B_i$, $B_{SO}$, and $B_s$ are fitting parameters allowing the determination of $\tau_i$, $\tau_{SO}$, and $\tau_s$, while $B_0$ is independently and separately known from $\tau_0$. We notice that in Eq. 1.14, $B_{11} = \dfrac{1}{2}(B_{00}+B_{10})$. Only two of the three fitting parameters are independent, therefore a MR measurement can only determine the two fields $B_i$ and $B_{SO}$. To determine the scattering rate of magnetic impurities $B_s$, an independent measurement for $B_i$ is needed. Thus in our experiments, we always require two adjacent identical patterns on the same sample, where one is left bare to obtain $B_i$ and the other is covered by the magnetic species of interest.

Several theories have been developed, Hikami Larkin and Nagaoka (HLN) [11], or Iordanskii, Lyanda-Geller, and Pikus (ILP) [46], that relate $\tau_{SO}^{-1}$ to the measured AL signal. HLN theory assumes a spin-orbit interaction cubic in the wavevector $k$, while ILP theory allows for the inclusion of terms linear as well as cubic in $k$. In our low mobility materials and at low temperatures, the spin-orbit scattering is dominated by the Elliott-Yafet mechanism. In this mechanism, the origin of the spin-orbit scattering is less important; it may be due to structural SOI combined with orbital scattering at impurities (as in our case), or due to spin-orbit scattering only locally at impurities. To properly express the interactions in our

studies, we adopt the HLN expression simplified from the ILP model with the linear $k$ term omitted [46], which is given by Eq. 1.16.

## 1.5 Quasi-relativistic Dispersion

From past studies, it has been realized that electrons in narrow-gap semiconductors behave analogous to relativistic electrons in vacuum with linear energy-momentum relationship [49, 50]. The analogy was first theoretically predicted in the presence of crossed magnetic and electric fields, and later confirmed by cyclotron-resonance experiments performed on InSb [50]. In the absence of external fields, considering a large spin-orbit energy $\Delta$ in $\boldsymbol{k} \cdot \boldsymbol{p}$ perturbation theory, the dispersion relation for the conduction band can be given by the simplified Kane formula [51, 52]

$$E_C(k) = \sqrt{\left(\frac{E_g}{2}\right)^2 + E_g \frac{\hbar^2 k^2}{2m_e^*}} - \frac{E_g}{2}, \tag{1.17}$$

where $E_g$ and $m_e^*$ are band gap and the effective mass at the $\Gamma$-point respectively. Compared with the relativistic relation between energy $E$ and the electron momentum $p$ for electrons in vacuum

$$E = \sqrt{p^2c^2 + m_e^2c^4} \tag{1.18}$$

with $c$ being the light velocity ($c = 3 \times 10^{10}$ cm/s), Eq. 1.17 has the identical form, where $m_e$ and $m_e c^2$ corresponds to $m_e^*$ and $\dfrac{Eg}{2}$. A maximum velocity $u$ which electrons can reach in semiconductors can be deduced by using the analogy $c = \sqrt{2m_e c^2/2m_e} \longrightarrow u = \sqrt{E_g/2m_e^*}$. Taking the experimental values of $E_g$ and $m_e^*$ for most of the common III-V compounds like InSb, InAs, InGaAs, a value of $u \sim 1.3 \times 10^8$ cm/s is obtained [50, 51]. The Fermi velocity of

electrons in these narrow-gap semiconductors is $\sim 10^7$–$10^8$ cm/s, therefore, quasi-relativistic phenomena should be considered and the dispersion relation in Eq. 1.17 is employed. When $E_g$ in Eq. 1.17 is infinitely large, the $E(k)$ dispersion will become the classically parabolic relation. Based on Eq. 1.17, the effective mass at any given $E$ can be derived through $m(E)^* = \dfrac{\hbar^2}{\partial^2 E/\partial k^2}$ as

$$m(E)^* = m_e^* \left(1 + \frac{2E}{E_g}\right)^3. \tag{1.19}$$

Consequently, the calculations of the transport parameters for our 2DESs have to be revised as well. The 2DES is confined within a quantum well with thickness of $w_{QW}$, which provides a wavevector $k_z$ perpendicular to the transport plane and quantized in $\dfrac{\pi}{w_{QW}}$. Accordingly, the Fermi wavevector can be written as $k_F = \sqrt{k_\parallel^2 + k_z^2}$, where $k_\parallel = \sqrt{2\pi n}$ is the in-plane wavevector. By replacing $k$ in Eq. 1.17 with $k_F$, the Fermi energy is then derived as $E_F = E(k_F) - E(k_z)$, where the second term on the right of the equation is the QW confinement energy and becomes 0 as $w_{QW} \longrightarrow 0$ . The inplane Fermi velocity is $v_F = \dfrac{\hbar}{\partial E/\partial k} = \dfrac{\hbar k_\parallel}{m_e^*} \dfrac{1}{1 + 2E_F/E_g}$, and the Fermi energy effective mass $m_{eF}^* = m_e^* \left(1 + \dfrac{2E_F}{E_g}\right)^3$. From $v_F$ and $m_{eF}^*$, both the elastic scattering time and the diffusion constant can be determined as $\tau_0 = m_{eF}^* \mu / e$ and $D = \dfrac{1}{2} v_F^2 \tau_0$.

In addition to the modifications applied to the transport parameters, the conventional (non-relativistic) two-dimensional (2D) and three-dimensional (3D) density of states are also modified due to this quasi-relativistic dispersion, resulting in

$$\begin{aligned} g_{2\mathrm{D}}(E) &= \frac{m_e^*}{\pi\hbar^2}\left(1 + \frac{2E}{E_g}\right), \\ g_{3\mathrm{D}}(E) &= \frac{m_e^*\sqrt{2m_e^* E}}{\pi^2\hbar^3}\left(1 + \frac{2E}{E_g}\right)\sqrt{1 + \frac{E}{E_g}}. \end{aligned} \tag{1.20}$$

## 1.6 InAs Surface Band Structure

The results of $n_s$ and $n_b$ obtained from the two-band fitting allow determination of $E_F$ as well as band-bending at the surface. Electrons follow the Fermi-Dirac distribution, and together with Eq. 1.20, the 3D bulk electron density can be derived as

$$n_{b3\mathrm{D}} = \int_{E_C^b}^{\infty} \frac{m_e^* \sqrt{2m_e^*(E - E_C^b)}}{\pi^2 \hbar^3} \frac{1}{e^{\frac{E-E_F}{kT}} + 1} \left[1 - \frac{2(E - E_C^b)}{E_g}\right] \sqrt{1 - \frac{E - E_C^b}{E_g}} dE. \quad (1.21)$$

where $E_C^b$ and $k_B$ are bulk conduction band minimum and the Boltzmann constant respectively. From $n_b$ (the experimental value obtained from the two-band analysis) and the InAs layer thickness, the numerical value of $n_{b3\mathrm{D}}$ can be calculated and plugged into Eq. 1.21. As a result, the distance between $E_F$ and $E_C^b$ can be attained. The band-bending at the surface approximately forms a triangular potential well (Fig. 1.1(a)), where the energies of accumulation electrons are quantized into a few of subbands. In the triangular well approximation, a constant electric field $F$ at the surface and an infinitely high potential barrier at the interface are presumed [53]. Correspondingly, the subbands energies $E_i$ with respect to the surface conduction band minimum $E_C^s$ are [53]

$$E_i - E_C^s = \left(\frac{9\pi^2}{8m_e^*}\right)^{\frac{1}{3}} \left[e\hbar F \left(i - \frac{1}{4}\right)\right]^{\frac{2}{3}}, \; i = (1,\ 2,\ 3, ...), \quad (1.22)$$

with $e = 1.6 \times 10^{-19}$ C being the electron charge. We assume only the first subband is occupied in the potential well, thereby $n_s$ can be expressed in an integral similar to Eq. 1.21 as

$$n_s = \int_{E_1}^{\infty} \frac{m_e^*}{\pi\hbar^2} \frac{1}{e^{\frac{E-E_F}{kT}} + 1} \left[1 - \frac{2(E - E_C^s)}{E_g}\right] dE. \quad (1.23)$$

With the $n_s$ value obtained from the two-band fitting, a test calculation by using Eqs. 1.22

and 1.23 proves that $E_2$ is above $E_F$, which implies occupation of a single subband by the surface electrons. According to Eq. 1.23 the distance between $E_1$ and $E_F$ can be derived. From Eqs. 1.22, 1.23, and 1.24

$$eFw_T = E_F - E_C^s = (E_F - E_1) + (E_1 - E_C^s) = 0.080 \text{ eV} + \left(\frac{9\pi^2}{8m_e^*}\right)^{\frac{1}{3}} \left(\frac{3}{4}e\hbar F\right)^{\frac{2}{3}}, \quad (1.24)$$

where $w_T$ is the width of the triangular well, the electric field caused by the band-bending at the surface can be obtained as well, and checked to be reasonably below the breakdown field of InAs ($\sim 5.0\times10^4$ V/cm [54]). The structural asymmetry induced by $F$ assures a prominent Rashba SOI. The extracted $w_T$ approximately equals to the electron wavelength along the direction perpendicular to the transport plane, as demonstrated in Fig. 1.9. Hence $k_z$ can be calculated as $\sim \frac{2\pi}{w_T}$. Figure 1.9 depicts the band structure and the probability density ($|\Psi|^2$) associated with the surface electron wavefunctions at the experiment temperatures. In Chap. 4, detailed calculations and explanations are provided, and show that the band structure analysis is self-consistent.

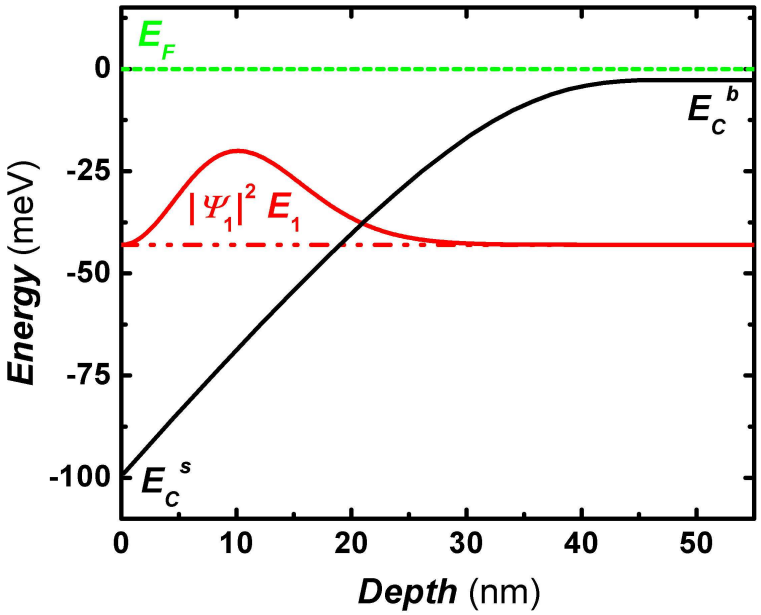


Figure 1.9: Schematic band structure at the surface of InAs, where the 2DES has a single occupied subband (the energy levels are explained in Chap. 4), and $|\Psi_1|^2$ represents the probability density in this subband (in arbitrary units, with $|\Psi_1|^2 = 0$ taken at the $E_1$ line).

# Chapter 2

# Experimental

We performed a series of comparative AL measurements to study the interactions between the 2DES and various magnetic surface species. Two different host systems are employed as 2DESs in our study, which are an InAs surface accumulation layer and an InGaAs quantum well (at a distance from the surface of a heterostructure). For each sample, two immediately neighboring twin-serpentine structures are patterned on the surface to enhance the observed signal by increasing the channel length to width ratio. The twin serpentines allow for comparative measurements with one being left bare and the other being covered by the following species: rare earth ions, transition metal ions, transition metal phthalocyanines, or CoFe nanopillars. The local spin moments of the species can modify the spin decoherence of a 2DES, which in turn will change the shape of AL. Taking the fact that the twin serpentines are fabricated simultaneously on the same sample and experience the same fabrication processes and cooldown, the measured AL signal differences will be due only to the presence of surface magnetic species and their interactions with the 2DES. Therefore, the interactions and spin exchange mechanisms between electrons and surface magnetic moments can be

investigated in this adjustable artificial structure.

In the following sections, the fabrication techniques of devices in this dissertation will be documented. The process of patterning the twin-serpentine structure onto surfaces of both InAs and InGaAs will be first described, as well as the deposition of surface species, processes include photolithography, electron-beam lithography, wet etching, and lift-off. Further, the techniques used to perform magnetotransport measurements at cryogenic temperatures (0.4-6 K) and magnetic fields up to 9 T will be discussed.

## 2.1 Sample Fabrication

Depending on the location of the 2DESs, different deposition scenarios for the surface species can be applied. The distant InGaAs QW from the surface allows an array of ferromagnetic nanopillars being delineated by thermal evaporation and lift-off after electron-beam lithography. In the case of the InAs film, however, thermal evaporation can change the Fermi level pinning at the surface to cause a variation in electron mobility and density of the accumulation layer. Therefore, magnetic species have been dissolved in water, chloroform, or any other solvents and deposited on the surface. Obviously, this method can be also applied to the InGaAs/InAlAs heterostructure. In the ensuing respective subsections, details of each device design will be presented.

### 2.1.1 InGaAs Sample

The InGaAs 2DES schematically depicted in Fig. 1.3 (a) was grown by molecular-beam epitaxy (MBE) on semi-insulating InP (001) substrate. The first step of sample fabrication

is to prepare 4 × 2 $mm^2$ InGaAs/InAlAs chips by cleaving from wafers. To make samples neat and clean, the chips are obtained by scribing the InP (001) surface (the back side) of the wafer with a carbide tip first, then cleaved, then cleaned and followed by soaking in trichloroethylene (TCE), acetone (ACE), and isopropyl alcohol (IPA) in consecutive order for 3 minutes each to remove organic, ionic, and metallic impurities. At the end, the surface is rigorously squirted with IPA and blown dry with $N_2$ gas to physically remove any large dust particles.

Device fabrication is based on patterning the clean chips. Two methods are most commonly used in microfabrication to create patterns. Photolithography, which transfers a geometric pattern from a photomask to a photon-sensitive chemical photoresist by exposing it under ultraviolet (UV) light, is capable of resolving to relatively large linewidths $\sim 1$ $\mu$m, limited by UV light diffraction. Electron-beam lithography is similar to photolithography but with the photoresist and the UV light being replaced with an electron resist and an electron beam from a scanning electron microscope (SEM), which can define smaller structures with linewidths $\sim$ 30 nm. Both methods are involved in InGaAs sample processing. Using electron-beam lithography, two adjacent twin serpentine structures were transferred onto a Hall bar mesa (itself patterned on the heterostructure material by photolithography), as depicted in Fig. 2.1. The detailed procedure is as follows.

The photoresist used in our cleanroom fabrication is AZ5206, which can be easily washed away by ACE. The clean chip is spin coated with a thin film of AZ5206 by a spin-coater (Specialty Coating Systems model P-6000). The mounting head of the spinner requires a minimum sample size with 15 mm in diameter, therefore, the chip has to be glued to a thin glass slide (18 × 18 $mm^2$ square) before mounting onto the machine. AZ5206 is also used as glue and the preferred gluing position is at the corner of the glass slide, where

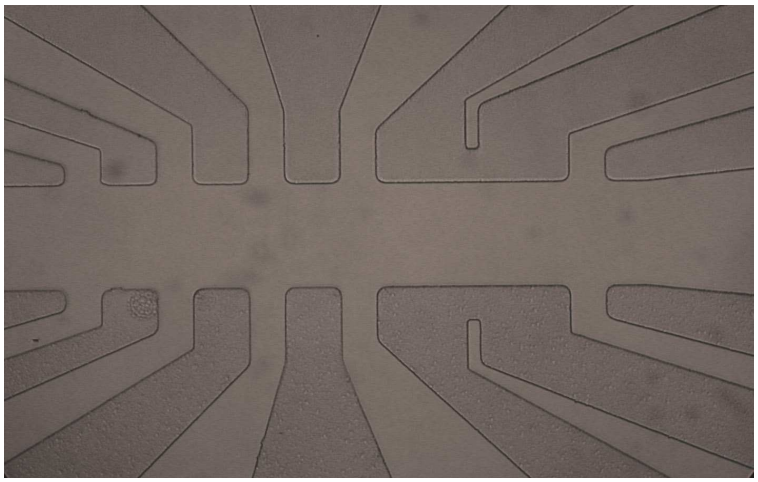

Figure 2.1: Optical micrograph of a Hall bar pattern.

more centripetal force can be applied to the spin-coating process. The glue is air dried for 5 minutes and baked in a 90 °C convection oven for 15 minutes. Next, in the darkroom, enough AZ5206 is dripped with a pipette to cover the chip surface, and immediately spun at 4000 rpm (revolution per minute) for 40 s to attain a uniform 0.6 $\mu$m thick AZ5206 layer. The photoresist-coated chip is then cured and prebaked in the 90 °C oven to drive off the excess photoresist solvent. After prebaking, the photoresist is exposed to a pattern of 365 nm UV light with an intensity of 11 mW/cm$^2$. The UV light is emitted from a mercury lamp in a Karl Suss (model MJB3) photolithography machine. The pattern is on a photomask, which is a glass plate with one side coated with an $Fe_2O_3$ film. The $Fe_2O_3$ film copies the pattern from original photomask made by Advanced Reproductions and selectively blocks portions of the device from being exposed to the UV light. Before exposure, the mask is aligned over the chip in such a way that the pattern avoids all of the defects on the sample surface. During the exposure, the side with the patterned $Fe_2O_3$ film physically contacts the surface of the photoresist. The exposure lasts for 22 s and causes a chemical change that allows the unshadowed photoresist to be removed by a developer. Developing the exposed device in a diluted AZ 351 developer (AZ 351 : $H_2O$ = 1 : 5) for 25 s successfully dissolves

away the exposed portions of the photoresist, followed by rinsing in de-ionized $H_2O$ for $\sim$ 30 s to wash off the developer. Then the sample is blown dry with $N_2$ gas. A 30 minutes post bake is performed after developing, typically to help solidify the remaining photoresist to make a more durable protecting layer in future wet chemical etching. After this step, the desired pattern is transferred to the photoresist film on top of the sample, but not yet to the sample itself.

A pattern can be transferred to an InGaAs/InAlAs sample after lithography by etching the exposed InGaAs to remove the QW layer. The etchant for InP cap of the heterostructure is a solution of $HCl : H_2O$ with a ratio of $1 : 2$. The 2 nm InP can be etched away after submerging the sample in the etchant for 10 s, followed by rinsing in de-ionized $H_2O$ for $\sim 30$ s to wash off the etchant. After blow-drying with $N_2$ gas, the sample is soaked in a solution of $H_3PO_4 : H_2O_2 : H_2O$ $(1 : 1 : 38)$ for 120 s to etch off 17 nm InAlAs and the 10 nm InGaAs layers. The etching time may be varied depending on the size and the shape of the pattern. Therefore, the etching is done in steps to monitor the progress under a microscope to avoid over etching. At this stage, the pattern is transferred to the sample. To provide a more visual explanation, the photolithography and the wet etching process are also presented pictorially in Fig. 2.2. Next step is to remove photoresist by soaking the sample in ACE for 1 hour, followed by boiling the sample in fresh ACE (75 °C) for 1 hour and submerging in fresh ACE at room temperature for another hour successively. At the end, the surface is squirted with IPA and blown dry with $N_2$ gas.

Before any further pattern processes, a contacting material is placed on each of the 12 contacting pads of the Hall bar mesa. The contact used for the sample depends on the compound. For InGaAs/InAlAs heterostructure, indium is used since it exists from the cap layer to the QW layer and can diffuse easily from the surface to the conducting QW layer by

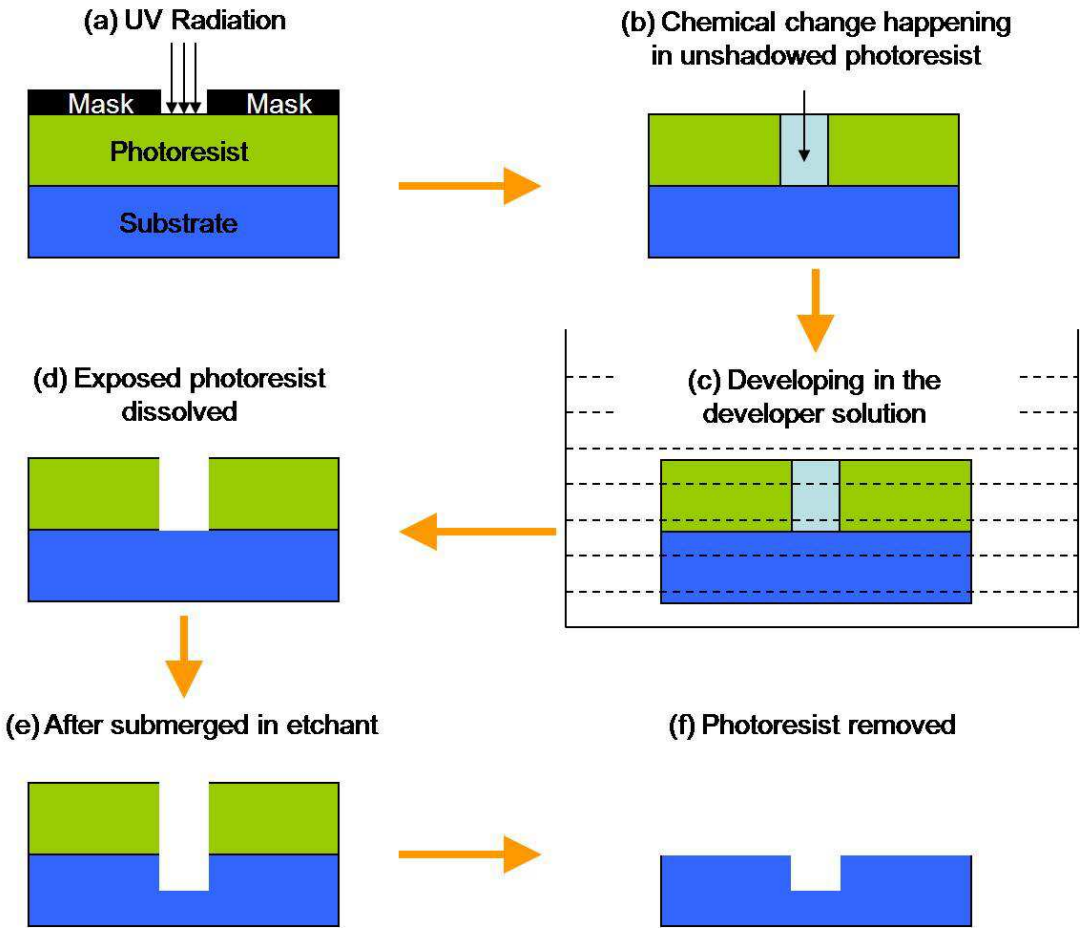


Figure 2.2: Cartoon of a photolithography ((a) – (d)) and an etching ((d) – (f)) process.

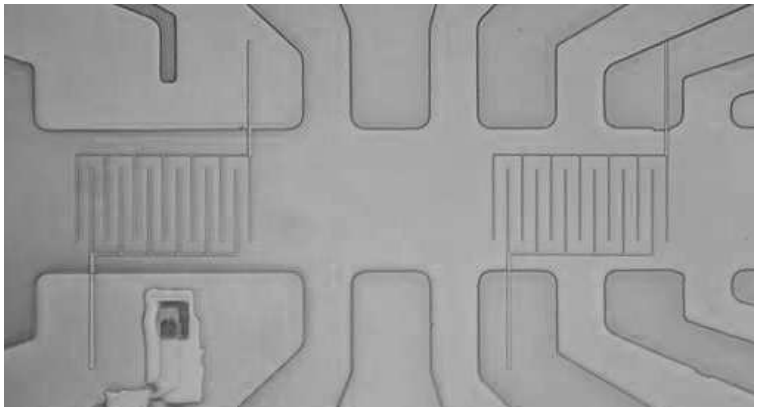

Figure 2.3: Optical micrograph of a sample with twin-serpentine pattern on a Hall bar pattern mesa.

a simple thermal annealing. Also, indium is chosen because it is very stable and conductive at low temperature (0.4 K). The melting point of indium is 156.60 °C, and the soldering iron is set to 220–240 °C. The soldering station used is a Weller model WD1M with a Weller RT1 Needle Tip. Once an In mound is soldered to every contacting pad, the sample is annealed in a homemade annealing station at 210 °C for 5 minutes. Typically the solders are placed on contacting pads during the device packaging, while here this step is right after photolithography. There are two reasons for this. One is that the later patterning processes may contaminate the contacting pads and prevent ohmic contacting. The other is that an annealing at the very end could cause unwanted thermal damages to the devices.

The next step is to pattern the twin serpentines onto the Hall bar mesa (Fig. 2.3) by using electron-beam lithography. Similar to photolithography, electron-beam lithography creates fine structures in an electron-sensitive film (electron resist) which can be subsequently transferred to the substrate material by etching. In an SEM, a focused beam of electrons is scanned to draw geometric patterns on a surface covered with 950 K polymethylmethacralate (PMMA) electron resist. The PMMA used in this thesis is dissolved in chlorobenzene with 3% concentration. Before spin-coating with the PMMA film, the sample has to be glued on a

glass slide covered by a layer of conducting metal such as gold to drain electrons, otherwise, a local accumulation of electrons can distort the pattern or even burn the PMMA. The sample is glued along one side and close to one corner of the glass slide with colloidal graphite, which is also a conducting material, then air dried at room temperature for 15 minutes, followed by a soft bake in a 170 °C oven for 45 minutes to set the colloidal graphite.

The PMMA is spun onto the sample at 7800 rpm for 40 s, resulting in layer thickness of 0.1 $\mu$m and then cured by baking in the 170 °C oven for 4 hours. The sample is loaded into the SEM chamber with pressure pumped down below $5 \times 10^{-5}$ Torr. The electron beam movement is controlled by Nano-Pattern Generating Software (NPGS), which accepts a pattern designed by a computer drawing program (DesignCAD .dc2 files). NPGS controls the magnification, beam current, center to center distance, line spacing, dose and pattern. The amount of exposure to the PMMA varies pattern by pattern due to the proximity effect. The pattern edges are smeared due to electron scatterings in the PMMA, therefore the exposure regions are normally broadened, and this effect is more pronounced when regions near one another are exposed. For example, a single dot with diameter of 40 nm can be exposed with 220 $\mu$C/cm$^2$ dose. However, if a fine line with width of 40 nm is exposed, which actually is written as an overlapping dot mesh, a dose of only 140 $\mu$C/cm$^2$ is necessary. The dc2 file contains the serpentine structure is named as *Serpentine Shrink*, which requires a 220 $\mu$C/cm$^2$ dose, a 12 pA current, and a 900 magnification during the electron beam writing. The exposed portions of PMMA can be developed by submerging in methyl iso butyl ketone (MIBK) diluted 3 times with IPA, for 70 s. Then the sample is immediately rinsed in IPA for $\sim$ 30 s, and is subsequently blown dry with $N_2$ gas. To transfer the serpentine patterns to the device, the wet etching procedures described above are repeated. After the 3-hour ACE cleaning process, the PMMA is removed from the sample and it is ready for the deposition of nanopillars.

To grow ferromagnetic nanopillars ($Co_{0.6}Fe_{0.4}$) on one of the serpentines, thermal evaporation in ultra high vacuum is implemented. The materials are deposited in a commercial Edwards (model 306 A) evaporator. Before loading the sample into the evaporator chamber, electron-beam lithography is applied once more to pattern an array of circles onto a new layer of PMMA. The pattern is actually a rectangle of polyfill (NPGS plotting function) with dot to dot distance set as 0.2 $\mu$m, and named as *New Dot Array*. The writing parameters such as dose, current, and magnification are set as 13 $\mu C/cm^2$, 35 pA, and 1400 respectively. For the evaporation, when the pressure in the chamber reaches $\sim 7 \times 10^{-7}$ Torr with the help of the liquid $N_2$ trap, the source material in a tungsten boat can be heated up by applying a large current. The heat is gauged by a current meter. The vaporized source material is condensed on the sample surface with the deposition thickness monitored by a quartz balance, which measures the shift in resonance frequency of a quartz crystal. Since CoFe does not stick well the sample surface, 7 nm Al is deposited (usually at a rate of 0.5–1.0 Å/s) to act as an adhesion layer for the CoFe. Subsequently, 29 nm CoFe is deposited at a rate of 1–2 Å/s. The deposition layer thickness is limited by the thickness of PMMA, which is 100 nm.

To create the array of CoFe nanopillars on InGaAs/InAlAs heterostructure, a final step of lift-off is necessary (demonstrated in Fig. 2.4). The sample is submerged in heated ACE for at least 1 minute. The surface of the device is then gently squirted with ACE until the whole film of PMMA is removed. Once lift-off is finished, the sample is immediately immersed in ACE with the 3-hour cleaning process. Figure 2.5(a) depicts the sample after lift-off, and Fig. 2.5(b) is the SEM picture for the fabricated CoFe nanopillars, whose dimensions are indicated in Fig. 2.5(c). The current sample carrying one bare serpentine and one serpentine covered with Al/CoFe nanopillars will be called the Al/CoFe sample. To assess the influence of the Al adhesion layer on the measurements, a control sample with one bare serpentine, and one covered by an array of 9 nm Al nanopillars is fabricated also (called the Al sample;

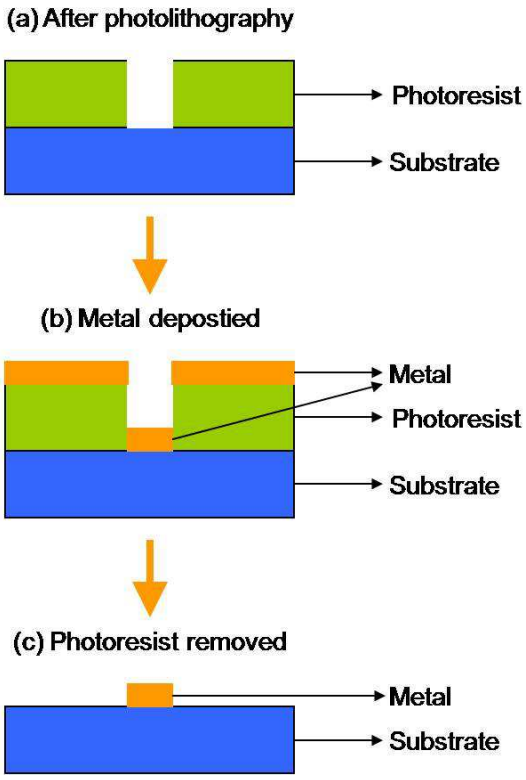


Figure 2.4: Cartoon of a lift-off process.

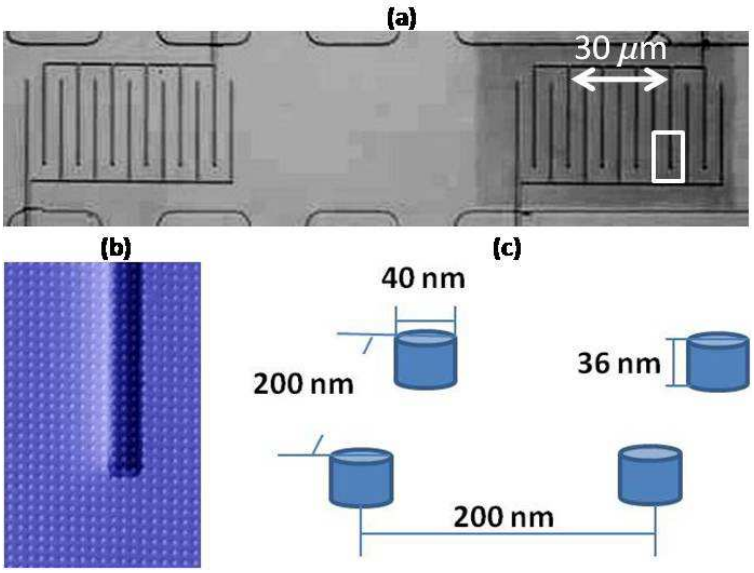


Figure 2.5: (a) Optical micrograph of a sample, with twin serpentine structures (bare and nanopillar-covered) on a mesa. The dark area (on the right) is covered by nanopillars. (b) Scanning electron micrograph of the area within the white outline in (a). (c) Dimensions of the Al/CoFe nanopillars and their array in (b). (Ref. [4])

the Al array has dimensions identical to the Al/CoFe array).

Finished samples have to be packaged into a standard 14 dual-inline package (DIP) header so that it can be mounted into the measurement apparatus. The sample is first electrically connected to the pins of an empty 14 pin DIP header by soldering Au wire from the contacting pads to the DIP header pins. First Au wires are soldered to the mounds placed on the contacting pads. Then the sample with Au wires is attached onto a DIP header by using Apiezon N low temperature grease to ensure that the sample does not fall off even at low temperatures. At the end, the free ends of the Au wires are soldered to the DIP header pins.

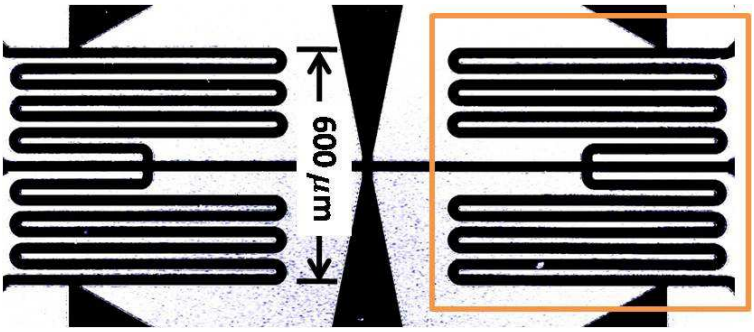


Figure 2.6: Structure of an InAs sample with two identical serpentines adjacent to each other. Right serpentine is covered by surface species with magnetic moments (within the square outline); Left is bare of magnetic moments for comparative measurements. (Ref. [5])

### 2.1.2 InAs Sample

The fabrication of InAs samples is relatively easier. During the pattern process, only photolithography is required, electron-beam lithography and lift-off are no longer needed. With a twin-serpentine structure photomask, two adjacent serpentines can be patterned onto the InAs surface as illustrated in Fig. 2.6. At the wet etching step, the etchant used for InAs is $H_2SO_4 : H_2O_2 : H_2O$ (1 : 8 : 15), and the etching time is 100–120 s depending on temperature and moisture. After the photoresist is removed InSn is soldered onto contacting pads at 175 °C. Once the sample is packaged in a DIP header, the surface magnetic species can be deposited on one of the two serpentines. The magnetic species were dissolved in de-ionized $H_2O$ to become aqueous nitrate solutions. The solutions of rare earth ions ($Gd^{3+}$, $Sm^{3+}$, and $Ho^{3+}$) and transition metal ions ($Fe^{3+}$, $Co^{2+}$, and $Ni^{2+}$) are all at a concentration of 6 $\times$ $10^{-4}$ M. In the case of transition metal phthalocyanines, the compounds were dissolved in chloroform with a concentration of $\sim$ $10^{-4}$ M. A 0.01 $\mu$L of any solution is deposited on one of the pair of serpentines by using a pipet from Fisherbrand (Model FINNPIPETTE) with pipet tips from Molecular Bioproducts (model ART 10 REACH), and then air dried. We estimate the surface species density on the order of $10^6$ $\mu m^{-2}$.

The rare earth ions (RE) and transition metal (TM) ions, are from nitrate salts dissolved in aqueous solutions. The preparation procedures are described below: 2.8 mg $Sm(NO_3)_3{\cdot}6H_2O$ is dissolved in 10 mL deionized water; 2.7 mg $Gd(NO_3)_3{\cdot}5H_2O$ is dissolved in 10 mL deionized water; 2.8 mg $Ho(NO_3)_3{\cdot}5H_2O$ is dissolved in 10 mL deionized water; 3.1 mg $Ni(NO_3)_2{\cdot}6H_2O$ is dissolved in 18 mL deionized water; 1.7 mg $Co(NO_3)_2{\cdot}6H_2O$ is dissolved in 10 mL deionized water; 3.6 mg $Fe(NO_3)_3{\cdot}9H_2O$ is dissolved in 15 mL deionized water. The nitrate salts are weighed by using an analytical balance from Sartorius (model BP1215). For the TM-phthalocyanine samples, one serpentine is covered by the phthalocyanine solution, and the other by the TM-phthalocyanine solution to exclude the effect of phthalocyanine molecules. Both TM-phthalocyanine and phthalocyanine compounds are not water soluble, but dissolve in chloroform. The solutions are prepared as below for Pc and TM-Pc: in the case of $Ni^{2+}$-phthalocyanine, 1.2 mg phthalocyanine and 1.5 mg $Ni^{2+}$-phthalocyanine in 40 mL chloroform each; in the case of $Co^{2+}$-phthalocyanine, 1.2 mg phthalocyanine and 1.6 mg $Co^{2+}$-phthalocyanine in 40 mL chloroform each; in the case of $Fe^{3+}$-phthalocyanine, 1.4 mg phthalocyanine and 1.7 mg $Fe^{3+}$-phthalocyanine in 40 mL chloroform each. These concentrations are on the order of $\sim 6 \times 10^{-4}$ M. However, dissolution is not complete at room temperature, and thus we consider the effective concentration to be $\sim 10^{-4}$ M for TM-phthalocyanine and phthalocyanine solutions.

## 2.2 Measurement Setup

To perform magneto-transport measurements on the devices, they are mounted into a low temperature system, a $^3$He cryostat capable of 0.38 K in steady state (Fig. 2.7). The $^3$He system is a homebuilt insert for a commercial $^4$He cryostat (Janis), depicted in Fig. 2.8 (b), which has several chambers filled with liquid He that can be pumped on to lower the vapor

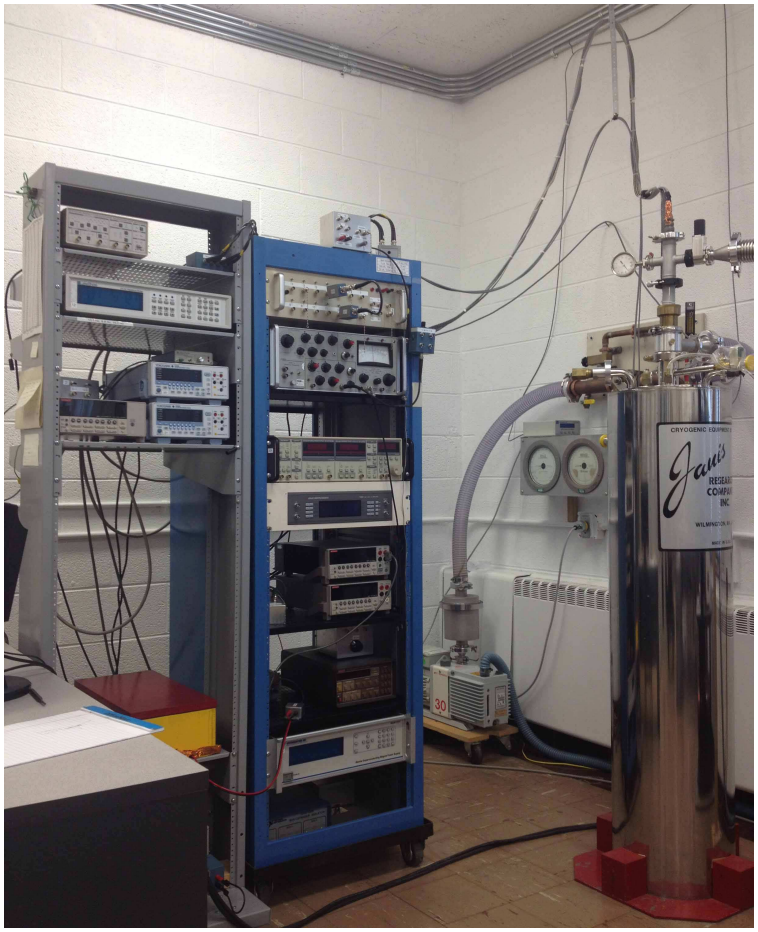

Figure 2.7: Equipment on the left shelf are LakeShore 370 AC resistance bridge, Princeton Applied Research P124A analog lock-in amplifier, SR 830 digital lock-in amplifier, EG&G 7265 digital lock-in amplifier, Keithley 2400 source meter, Keithley 2000 multimeter, Cryomagnetics CS-4 superconducting magnet power supply. On the right is the cryostat system.

pressure, thus lowering the temperature. It incorporates a superconducting (SC) magnet to achieve magnetic fields of up to 9 T. In addition, it is not necessary to use $^3$He in the inner-most chamber. Often, a $^4$He exchange gas is used, for the base temperature to 1.2 K.

All of the measurements require low noise, and are performed by using lock-in amplifiers for both sourcing current and measuring voltages. The lock-in amplifiers utilized are from Stanford Research Systems (model SR830), EG&G (model 7265), and Princeton Applied Research (model P124A). The first two are digital instruments while the third one is an

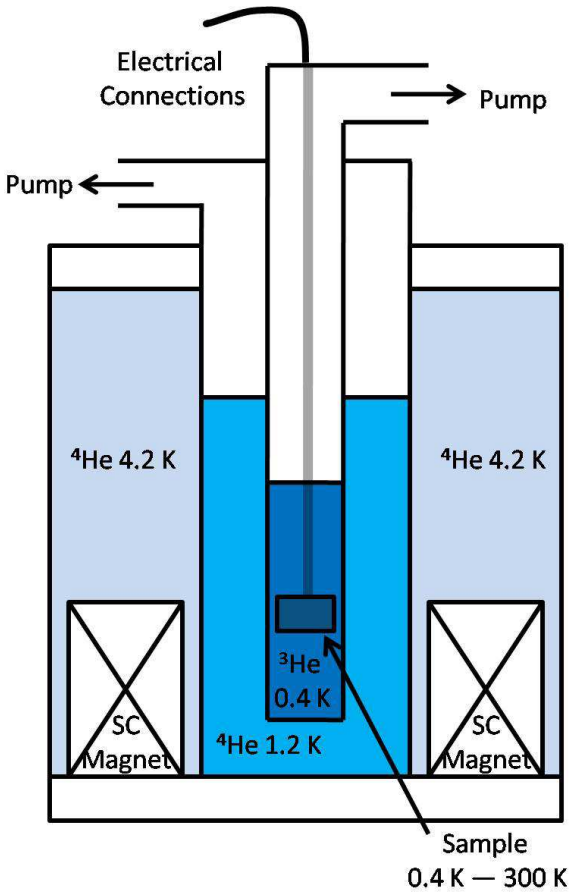


Figure 2.8: Schematics of $^3$He cryostat.

analog instrument. The analog lock-in's signal is monitored by a Keithley (model 2400) voltmeter. The temperature is measured by the resistance bridge in a Lakeshore (LS370AC) temperature controller, which also controls the probe heaters to regulate the measurement temperature. The magnets are driven by external power supplies isolated from the measurement electronics. The superconducting magnet of the $^3$He system is powered either by a Cryomagnetics (model CS-4) or a Kepco (model BOP 20-10D), where the Kepco is driven externally by a Keithley (model 2400) source-measure unit in source-voltage mode. During the measurement, magnetic fields are perpendicular to the surfaces of InAs. All of the information regarding to the electrical, temperature, and magnetic field measurements and control are combined via general purpose interface bus (GPIB) lines. The data acquisition and remote control of the instruments are performed by LabVIEW programs.

# Chapter 3

# Interactions between InGaAs Electrons and Ferromagnetic Nanopillars

The buried $In_{0.53}Ga_{0.47}As$ QW inside the InGaAs/InAlAs heterostructure provides us the possibility to define an array of ferromagnetic nanopillars on the surface without affecting the transport properties of the 2DES. The nanopillar matrix pattern (Fig. 2.5(c)) fabricated by electron-beam lithography is also similar to the structure of a spin-transfer torque magnetoresistive random-access memory (STT-MRAM) [55], which is a new type of solid-state memory that uses electrical currents to read and write data stored in the magnetic moments. As a pioneering product in the market, STT-MRAM combines all the advantages from the old memory devices, which makes it compact, speedy, low-power, and nonvolatile. However, the high building cost limited by the writing current hinders its development. Therefore, how to reduce the current to flip the magnetic moment of a cell in STT-MRAM still requires

numerous fundamental studies. The magnetic moment flipping rate is related to the spin coherence time (determined by spin-orbit and spin-flip scatterings), which can be investigated via the interactions between CoFe nanopillars and the InGaAs QW. The surface magnetic species changes both $\tau_{SO}^{-1}$ and $\tau_s^{-1}$ of 2DESs. Normally the interaction increases $\tau_{SO}^{-1}$ and $\tau_s^{-1}$, with $\tau_{SO}^{-1}$ less sensitive to the interacting distance and $\tau_s^{-1}$ more sensitive. The InGaAs QW is located 19 nm below the heterostructure surface, which is approximately one Fermi wavelength $\lambda_F$ of the QW electron. Therefore it is plausible to probe the modification of the SOI, while it is too far for the ferromagnetic surface species to generate spin-flip scatterings in the QW. Furthermore, the magnetic moments of CoFe nanopillars are fairly strong due to their high saturation magnetization. These strong moments can be aligned by the external magnetic fields to generate other average effects in the 2DES. All of these quantum properties in the presence of the surface species can be experimentally studied by low-temperature AL measurements.

The InGaAs/InAlAs heterostructure studied here has a prominent Rashba SOI due to structural inversion asymmetry caused by the single doped layer under the QW. Hence a strong AL signal is anticipated in MR measurements. The characteristic MR of AL, being due to spin-dependent quantum interference, carries quantitative information about phase and spin decoherence, and thus is a valuable tool to experimentally study $\tau_\phi$, $\tau_{SO}$, and $\tau_s$. Yet when spin-flip interactions between surface magnetic moments and the QW electrons can be neglected, then $\tau_\phi^{-1} = \tau_i^{-1}$, which is the case for the system under study. In a series of comparative measurements we find that the presence of the ferromagnetic nanopillars modifies the SOI and phase coherence properties of the 2DES in the QW, as determined by the quantum corrections to the 2DES conductivity arising from AL.

## 3.1 Quantum Well Transport Properties

Quantum interference of AL happens at sufficiently low temperatures, and the experiments are performed at two different temperatures, 0.4 K and 1.3 K. Prior to analyzing the AL measurements, it is necessary to characterize the transport properties of the QW. Electrical transport characterizations of the InGaAs QW are obtained from Hall and MR measurements at corresponding $T$. The transverse ($R_{XY}$) and longitudinal ($R_{XX}$) transport coefficients shown in Fig. 3.1, from which $n$ and $\mu$ can be extracted, were measured on the bare serpentine of the Al sample at 0.4 K. Both quantum Hall ($R_{XY}$) and Shubnikov-De Haas oscillations ($R_{XX}$) are observed. The flat MR background and the linear Hall slope around $B = 0$ both indicate no evidence of two-band transport and hence single-subband occupancy in the QW is assumed. With the zero-field Hall slope $R_H = 395.4\ \Omega/\mathrm{T}$, the 2DES areal density of the QW can be attained with a simple calculation as $N_s = 1/eR_H = 1.6 \times 10^{12}\ \mathrm{cm}^{-2}$. Meanwhile $N_s$ can be also calculated from Shubnikov-De Haas oscillations as $N_s = \dfrac{e}{\pi\hbar B_{SdH}}$ $= 1.6 \times 10^{12}\ \mathrm{cm}^{-2}$ with spin degeneracy being considered, where $B_{SdH} = 34.0$ T (Fig. 3.1) is the frequency of the Shubnikov-De Haas oscillations periodic in $1/B$. Calculations from $R_{XY}$ and $R_{XX}$ are in accordance concerning $N_s$. Accounting for quasi-relativistic dispersion in the InGaAs conduction band, with $m_e^*/m_e = 0.0353$, $w_{QW} = 10$ nm, and $E_g = 813$ meV, the measured $N_s$ and $\mu$ are used to derive other transport parameters, such as $\tau_0$, $D$, $E_F$, $\lambda_F$. Table 3.1 summarizes the measured and derived transport properties at $T =$ 0.4 K. The measured $N_s$ and $\mu$ of the same sample do not vary between $T = 0.4$ K or 1.3 K, consequently neither do other parameters in Table 3.1. As Table 3.1 indicates, we experimentally find that the nanopillars on the surface tends to increase $N_s$ and $\mu$ for both the Al/CoFe sample and the Al sample. The $\sim 3\%$ metal coverage of the surface could slightly change the pinning position of $E_F$ and hence the band-bending, which results in a variation in $N_s$. Also, the presence of the effectively metallic coverage and the increased electron density

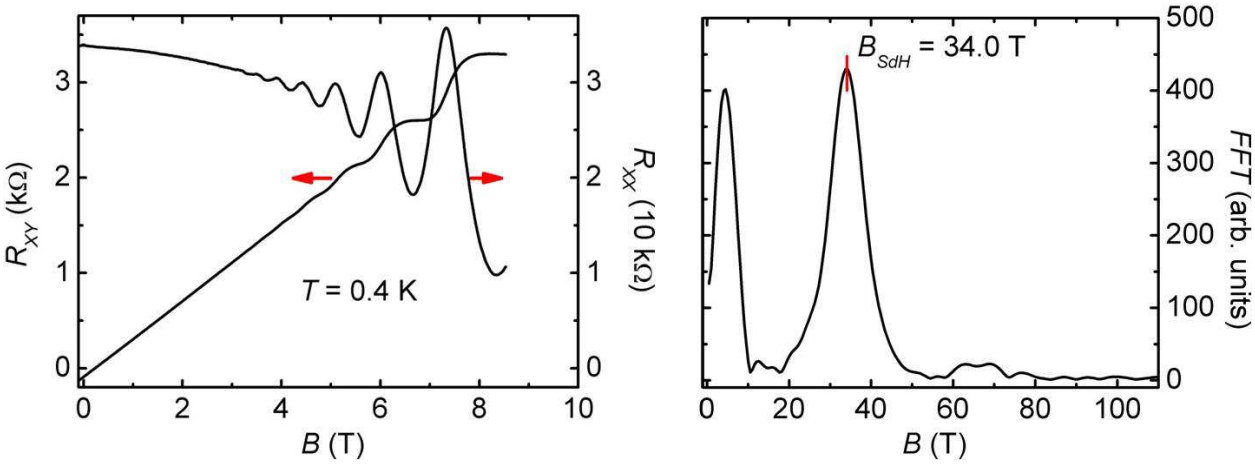


Figure 3.1: Left panel: $R_{XY}$ and $R_{XX}$ transport coefficients vs $B$, obtained on the bare serpentine of the Al sample at 0.4 K. Right panel: Fast Fourier transforms (FFT) of $R_{XX}$ data in the left panel with the first peak from the background noise, and the second peak from the Shubnikov-de Haas oscillation.

could enhance the Coulombic screening of the ionized impurity scattering, therefore $\mu$ will be improved. Compared with other $In_{0.53}Ga_{0.47}As/In_{0.52}Al_{0.48}As$ heterostructures [56, 57], the present 2DES has a relatively low $\mu$, which is due to the single doping layer situated underneath the QW. This doping scenario ensures a strong asymmetry of the confinement potential and hence substantial SOI, exploited here for the pronounced AL to which it leads. Moreover AL is a quantum interference between two time-reversed paths of an electron, thus requiring a lower value of $\mu$ to increase the possibility of an electron returning to the incident point during the transport.

## 3.2 Analysis and Results

After the sample is cooled to $T$ (0.4 K and 1.3 K), magnetotransport measurements occur by using standard four-contact low-frequency lock-in techniques with $B$ always applied normal to the surface. The twin serpentines on one sample (Fig. 2.5(a)) experience the same cooling

Table 3.1: InGaAs QW 2DES serpentine transport properties: $N_s$, $\mu$, $D$, $E_F$, and $\lambda_F$, at $T$=0.4 K.

| | Al/CoFe sample Covered | Al/CoFe sample Bare | Al sample Covered | Al sample Bare |
|---|---|---|---|---|
| $N_s$ ($10^{12}$ cm$^{-2}$) | 1.6 | 1.5 | 1.7 | 1.6 |
| $\mu$ ($10^4$ cm$^2$/Vs) | 0.68 | 0.63 | 1.2 | 1.0 |
| $D$ ($10^3$ cm$^2$/s) | 1.1 | 0.91 | 2.0 | 1.6 |
| $E_F$ (meV) | 81 | 77 | 86 | 81 |
| $\lambda_F$ (nm) | 20 | 20 | 19 | 20 |

history and fabrication processes apart from the presence of the nanopillars, allowing comparative measurements to assess the influence of the nanopillars [6, 4, 5]. Prior to discussing the details of the data analysis, we use Fig. 3.2 to demonstrate the effect of the nanopillars. Figure 3.2 represents the comparative low-$B$ AL data for the Al/CoFe sample and the Al sample, at two experiment temperatures. An expression of $\Delta R(B)/R_0$ is applied to present the MR, where $\Delta R(B) = R(B) - R_0$ defined as the AL correction to the longitudinal resistance $R$, and $R_0 = R(B = 0)$. The data displayed in Fig. 3.2 is symmetrized to eliminate the contributions from the external electronic shifts like Hall effect. Figure 3.2 exhibits the characteristic curves of AL, with an initial increase in $R$ from $B = 0$, reaching a maximum at $B \sim 90$ G, beyond which negative MR is observed. As introduced in Chap. 1, the separation in $B$ between two resistance maxima and the depth of the resistance minimum are sensitive to $\tau_{SO}$ and $\tau_\phi$, which can be extracted from fittings (detailed fits are presented later). The MR of the *bare* serpentines of both the Al/CoFe sample and the Al sample are plotted in Figs. 3.2(a) and (c) (to account for processing variations between the samples, a scaling factor of 1.5 is multiplied to the resistance values of the Al sample, which does not affect the $\tau_\phi$ and $\tau_{SO}$ values deduced from the data but makes the MR of the two *bare* serpentines almost identical). The MR of the serpentines *covered* with nanopillars, of both the Al/CoFe sample and the Al sample are plotted in Figs. 3.2(b) and (d). From Figs. 3.2(a)–(d), evaluating the

data for the Al sample (black traces), it is apparent that Al nanopillars lower and narrow the AL signal. In contrast, the Al/CoFe nanopillars not only lower but also notably broaden the AL signal, demonstrating the sensitivity of AL to surface coverage [6, 4, 5]. Information about the interaction between the surface moments and the 2DES is extracted from the comparative (rather than absolute) AL data, as described below.

Determined by $\tau_s^{-1}$, spin-flip scattering is a spin exchange mechanism between electrons and the local magnetic moments, which happens when electrons are within a short range of a local moment. Therefore, the introduced $\tau_s^{-1}$ from the distant ferromagnetic nanopillars is rather weak compared with $\tau_i^{-1}$. In fact a test fitting by using Eq. 1.16 suggests that $B_s$ ($\sim \tau_s^{-1}$) is at least two orders of magnitude smaller than $B_i$ ($\sim \tau_i^{-1}$) and $B_{SO}$ ($\sim \tau_{SO}^{-1}$), and thus negligible. The phase decoherence is then mainly depending on $\tau_i^{-1}$. Since then $B_\phi \simeq B_i$, we substitute $B_i$ with $B_\phi$, and drop $B_s$ in Eq. 1.16 to obtain

$$\begin{aligned}\Delta\sigma_2(B) = &-\frac{e^2}{2\pi^2\hbar}\left\{\left[\Psi\left(\frac{1}{2}+\frac{B_0}{|B|}\right)-\Psi\left(\frac{1}{2}+\frac{B_\phi+B_{SO}}{|B|}\right)+\frac{1}{2}\Psi\left(\frac{1}{2}+\frac{B_\phi}{|B|}\right)\right.\right.\\ &\left.\left.-\frac{1}{2}\Psi\left(\frac{1}{2}+\frac{B_\phi+2B_{SO}}{|B|}\right)\right]-\left[ln\left(\frac{B_0}{|B|}\right)-ln\left(\frac{B_\phi+B_{SO}}{|B|}\right)\right.\right.\\ &\left.\left.+\frac{1}{2}ln\left(\frac{B_\phi}{|B|}\right)-\frac{1}{2}ln\left(\frac{B_\phi+2B_{SO}}{|B|}\right)\right]\right\}.\end{aligned} \tag{3.1}$$

Since $\Delta R(B) \ll R_0$, with $\Delta\sigma_2(B)/\sigma_2(B=0) \approx -\Delta R(B)/R_0$, experimental $\Delta R(B)/R_0$ values can be directly compared to Eq. 3.1. Good correspondence exists between Eq. 3.1 and our experimental results. Equation. 3.1 is parameterized in $B_0$, $B_\phi$, $B_{SO}$. Since $B_0$ is independently and separately derived from the transport parameters $\tau_0$ and $D$, two data sets, on twin bare and nanopillar-covered serpentines, are sufficient to determine $B_\phi$, $B_{SO}$.

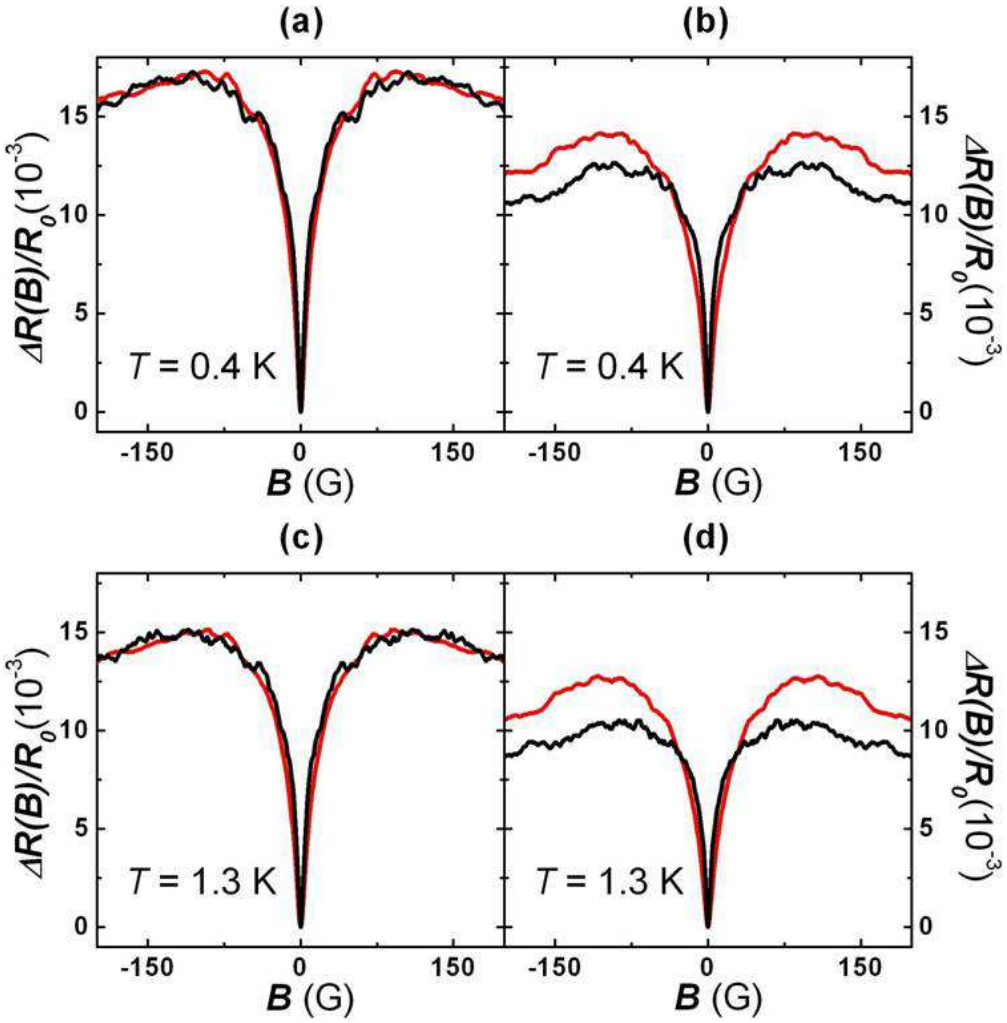


Figure 3.2: (a) Magnetoresistance due to AL at 0.4 K on the bare serpentines of the Al/CoFe sample (red) and the Al sample (black). (b) Magnetoresistance due to AL at 0.4 K of nanopillar-covered serpentines of the Al/CoFe sample (red) and the Al sample (black). (c) Same as (a) but at 1.3 K. (d) Same as (b) but at 1.3 K. (Ref. [4])

For the bare serpentines of the Al/CoFe sample and of the Al sample, and on the Al nanopillar-covered serpentine of the Al sample, their $B_\phi$ and $B_{SO}$ can be directly determined from the data. Comparing the AL data of the two bare serpentines (Figs. 3.2 (a) and (c)), we expect that they yield similar $\tau_\phi$ and $\tau_{SO}$ values. Indeed when we perform a least-squares fitting and extract $\tau_\phi$ and $\tau_{SO}$ for the Al/CoFe sample and the Al sample, we find that $\tau_\phi$ and $\tau_{SO}$ values for both bare serpentines are close: both $\tau_\phi$ and $\tau_{SO}$ of the Al/CoFe sample are just 1.2 times higher than of the Al sample. A fitting for the Al nanopillar-covered serpentine of the Al sample also yields values for its own $\tau_\phi$ and $\tau_{SO}$. Values are tabulated as scattering rates in Table 3.2. We now turn to the Al/CoFe nanopillar-covered serpentine of the Al/CoFe sample. From previous studies of magnetic impurities in metal systems [14], we learn that ferromagnetic nanopillars can induce an additional spin-orbit scattering rate $\tau_{SO}^{-1}$, without affecting the phase docoherence rate $\tau_\phi^{-1}$. Yet, we experimentally find that the fringing magnetic fields from to the ferromagnetic pillars affect the AL data by generating an average offset in the value of $B$ normal to the surface, with a constant offset absolute value $|\bar{B}_z|$ and a sign following the sign of the applied $B$. The averaged contribution from the fringing fields at the level of the 2DES is then approximated as a step function described as $|\bar{B}_z|$ at $B \geq 0$, and $-|\bar{B}_z|$ at $B < 0$. This model will be discussed in details in the section of *Al/CoFe Device*. The AL correction to conductivity in normal $B$ is then modified as:

$$\Delta\sigma_2'(B) = \begin{cases} \Delta\sigma_2(B + |\bar{B}_z|) - \Delta\sigma_2(|\bar{B}_z|) & B \geq 0 \\ \Delta\sigma_2(B - |\bar{B}_z|) - \Delta\sigma_2(|\bar{B}_z|) & B < 0 \end{cases}, \tag{3.2}$$

where $|\bar{B}_z|$ is introduced as an additional fitting parameter. A good result is obtained by fitting Eq. (3.2) to the AL data of the Al/CoFe nanopillar-covered serpentine, and $|\bar{B}_z|$ is found to be $\sim 35$ G (Table 3.2). It will be shown below that $|\bar{B}_z| \sim 35$ G is in good agreement with a micromagnetics calculation using a magnetization normal to the 2DES plane. The

same fitting provides $B_{SO}$ and hence $\tau_{SO}$ for the Al/CoFe nanopillar-covered serpentine. Concerning $B_\phi$ and $\tau_\phi$, since on this serpentine $B_s \sim 0$, we have assumed the same ratio 1.2 as between the bare serpentines, between $\tau_\phi$ of the Al/CoFe nanopillar-covered serpentine and $\tau_\phi$ of the Al nanopillar-covered serpentine. By this method $\tau_\phi$ and $\tau_{SO}$ are obtained for all serpentines, bare and covered, presented as scattering rates in Table 3.2.

Figure 3.3 shows the good correspondence between data and theoretical fits by using Eq. 3.2 for both bare and covered serpentines of the two samples at different $T$. Different AL models and uncertainty in the transport parameters can lead to a variation of $\sim 30\%$ in the absolute values of $\tau_\phi$ and $\tau_{SO}$. However, our experiments are comparative: we maintain the same nanopillar coverage, compare covered serpentines to bare serpentines measured on the same samples and at the same $T$, and apply the same model, ensuring that comparisons between covered and bare serpentines regarding $\tau_\phi$ and $\tau_{SO}$ bear reliable conclusions. The use of Eq. (3.2) results in a good fit, and is appropriate for samples where spin scattering is dominated by the Elliott-Yafet mechanism [58, 59], which, as described below, will prove to be the case in our InGaAs QW.

The values in Table 3.2 indicate a phase decoherence rate $\tau_\phi^{-1}$ scaling with $T$ for each serpentine, consistent with dominant Nyquist decoherence [60] arising from fluctuations in the electromagnetic background. Experimentally, the presence of Al/CoFe or Al nanopillars increases $\tau_\phi^{-1}$.

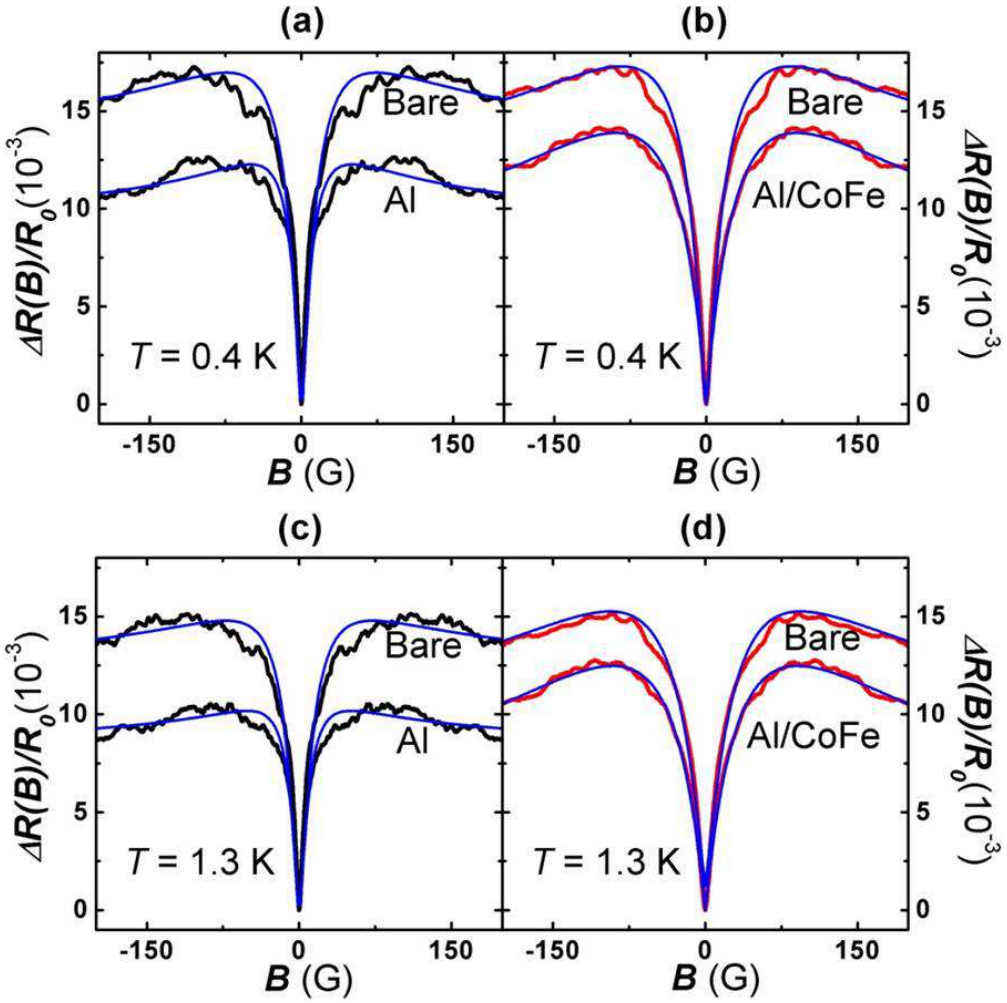


Figure 3.3: (a) Magnetoresistance due to AL on bare and covered serpentines of the Al sample (black solid lines) at $T = 0.4$ K and (c) at $T = 1.3$ K. (b) Magnetoresistance due to AL on bare and covered serpentines of the Al/CoFe sample (red solid lines) at $T = 0.4$ K and (d) at $T = 1.3$ K. Blue solid lines in all panels are theoretical fits. Ref.([4])

Table 3.2: 2DES scattering rates and fitting parameters: $\tau_0^{-1}$, $\tau_i^{-1}$, $\tau_{SO}^{-1}$ and $|\bar{B}_z|$, at $T = 0.4$ K and 1.3 K.

| | | Al/CoFe sample Covered | Al/CoFe sample Bare | Al sample Covered | Al sample Bare |
|---|---|---|---|---|---|
| $\tau_0^{-1}$ (ps$^{-1}$) | (0.4 K) | 2.5 | 2.7 | 1.4 | 1.8 |
| | (1.3 K) | 2.5 | 2.7 | 1.4 | 1.8 |
| $\tau_\phi^{-1}$ (ps$^{-1}$) | (0.4 K) | 0.10 | 0.077 | 0.081 | 0.063 |
| | (1.3 K) | 0.27 | 0.21 | 0.22 | 0.17 |
| $\tau_{SO}^{-1}$ (ps$^{-1}$) | (0.4 K) | 0.91 | 0.77 | 0.48 | 0.63 |
| | (1.3 K) | 0.91 | 0.77 | 0.48 | 0.63 |
| $\|\bar{B}_z\|$ (G) | (0.4 K) | 34 | / | / | / |
| | (1.3 K) | 36 | / | / | / |

## 3.3 Al Sample

### 3.3.1 Spin Decoherence Mechanism

In $n$-type semiconductors, two spin relaxation mechanism are responsible for the spin decoherence of conduction electrons: the Elliott-Yafet (EY) mechanism and the Dyakonov-Perel (DP) mechanism. Spin relaxes in the EY mechanism due to an admixture of spin-up and spin-down states in the electron Bloch eigenstates. In the presence of both spin orientations, momentum scattering (spin-independent) can cause spin-flips and hence spin relaxation. Separately, an electron spin precesses in the effective magnetic field generated by SOI interactions, which changes in random directions at every momentum scattering event. Therefore, spin precesses randomly between adjacent scattering events, and this randomwalk-like evolution of spin phase leads to spin decoherence via the DP mechanism.

A physical picture for these two spin decoherence mechanisms is described below. In the EY mechanism, the electron spin is locked to the electron momentum, and the coherence is maintained before any momentum scattering happens. Momentum scattering will cause a random change in momentum, and therefore lead to the spin decoherence. The spin decoherence rate due to EY ($\tau_{SO}^{-1\ \mathrm{EY}}$) will hence be proportional to the momentum scattering rate, $\tau_0^{-1}$. In the DP mechanism oh the other hand, we consider the electron spin precessing around a spin-orbit field with a Larmor frequency of $\Omega_k$ and a initial phase $\Phi_0$. Upon every scattering, the momentum of the electron will change, so does the spin-orbit field, and the electron spin will now start from $\Phi_0$ and precess around this new effective field which will be in a different direction and a different magnitude. If scattering occurs frequently enough so a full precession cannot take place ($\Omega_k\tau_0 < 1$), then over a time period $t$, the phase of the spin is said to be randomly walking. Since in the DP mechanism frequent momentum scattering prevents a substantial relative phase accumulation between electron spins, the spin decoherence rate due to DP ($\tau_{SO}^{-1\ \mathrm{DP}}$) will be inversely proportional to the momentum scattering rate, $\tau_0^{-1}$. The DP mechanism differs from the EY mechanism in that loss of spin orientation occurs between scattering events and not at spin-independent scattering events.

From past studies, the spin decoherence rate of the EY and the DP mechanism are derived as [61]

$$\frac{1}{\tau_{SO}^{\mathrm{EY}}} = \frac{\alpha_{\mathrm{EY}}}{\tau_0}\left(\frac{E_F}{E_G}\right)^2, \qquad \frac{1}{\tau_{SO}^{\mathrm{DP}}} = \alpha_{\mathrm{DP}}\tau_0\left(\frac{E_F^3}{\hbar^2 E_G}\right). \tag{3.3}$$

The most striking difference between the EY and the DP mechanisms is their dependence on momentum relaxation time (elastic scattering time $\tau_0$): $\tau_{SO}^{\mathrm{EY}} \propto \tau_0$ and $\tau_{SO}^{\mathrm{DP}} \propto 1/\tau_0$. Another important distinction is the energy dependence of the DP (cubic) mechanism compared to the EY (quadratic) mechanism. This will cause the DP mechanism to be stronger at higher temperatures. Generally, the DP mechanism is a stronger relaxation mechanism except in

cases where the semiconductor has a small band gap.

### 3.3.2 Elliott-Yafet System

From the above discussion, at low $T$ the spin scattering of III-V narrow gap semiconductors with low $\mu$ is dominated by the EY mechanism [61, 62, 63], which causes the spin-orbit scattering rate $\tau_{SO}^{-1}$ to decrease as $\mu$ increases ($\tau_{SO}^{-1} \sim \tau_0^{-1}$) [64]. We have mentioned that the Al coverage on the Al sample surface increases $\mu$, possibly by a change in band bending or by additional screening of the ionized impurities within the heterostructure, or both. Accordingly, for the Al sample Table 3.2 shows a decrease in $\tau_{SO}^{-1}$ for the Al nanopillar-covered serpentine compared with the bare serpentine. The ratios between bare and covered serpentines of respective values of $\tau_{SO}^{-1}$ as well as $\tau_0^{-1}$ are both $\sim 1.3$, showing that the EY expectation of $\tau_{SO}^{-1} \sim \tau_0^{-1}$ holds for the Al sample.

## 3.4 Al/CoFe Sample

### 3.4.1 Average Offset Fringing Field

Each Al/CoFe nanopillar is magnetized by the external $B$ and accordingly generates a fringing field, which can be estimated. The saturation magnetization of $Co_{0.6}Fe_{0.4}$ can be calculated from superconductor-insulator-ferromagnet spin polarization data [65], as $M_s = 1770$ emu/cm$^3$, close to the calculated saturation magnetization of $Co_{0.5}Fe_{0.5}$, $M_s = 1800$ emu/cm$^3$ [66]. The typically high $M_s$ of $Co_{0.6}Fe_{0.4}$ yields fringing fields still appreciable at the QW. The fringing fields flip direction according to the direction of the applied $B$, and at a low

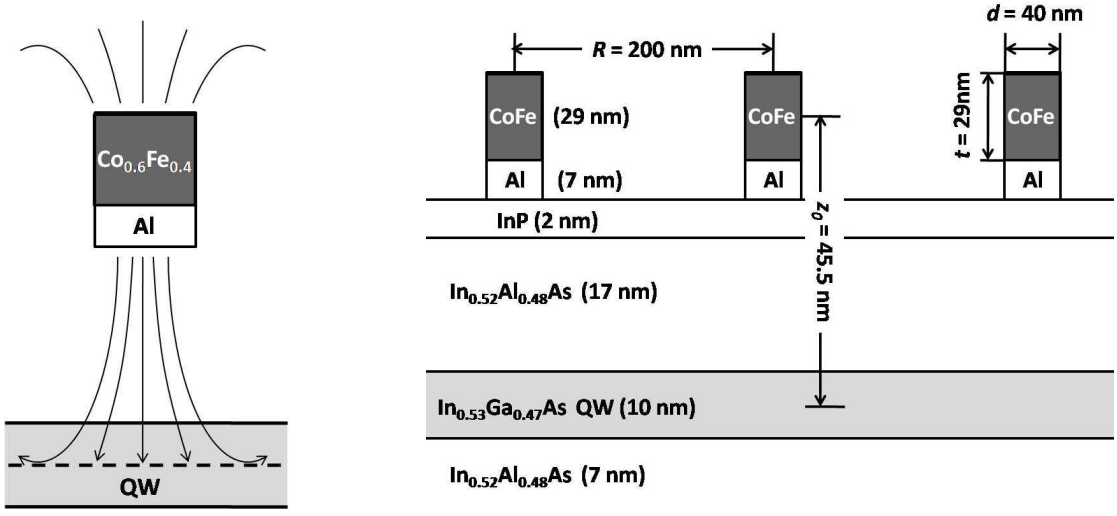


(a) (b)

Figure 3.4: (a) Schematic of the fringing fields at the QW generated by one CoFe nanopillar. (b) Schematic side view of the Al/CoFe nanopillars on the surface of the heterostructure. The effective separation between the magnetic dipoles and the QW is taken as $z_0 = 45.5$ nm, the distance between two neighboring nanopillars is $R = 200$ nm, the diameter of each nanopillar is $d = 40$ nm, and the thickness of the CoFe layer is $t = 29$ nm (Ref. [4]).

coercive field. The coercive field can be estimated to be below $\sim 1$ G, as a consequence of the low crystalline coercive field of the soft-magnetic $Co_{0.6}Fe_{0.4}$ ($\sim 0.2$ G) [67] and the low shape anisotropy of the nanopillars (the ratio of height to diameter is 0.9). The nanopillar diameter is also small (40 nm) compared to the interpillar distance (200 nm) and hence the interaction between nanopillars is negligible. Compared with the range of $B$ for the AL signal, the applied $B$ where the fringing fields flip sign is thus small.

With a low crystalline coercive field and low shape anisotropy, anisotropy is not expected to be decisive in determining the magnetization direction, but rather the direction will depend on the orientation of the variable externally applied $B$, down to the very low coercive fields. For the micromagnetics calculation supporting the AL analysis we hence assume a magnetization normal to the 2DES plane. The experiments suggest that the Al/CoFe nanopillars create a non-negligible $B$ at the level of the 2DES, and calculations bear this out, as out-

lined below. We approximate each nanopillar as an ellipsoidal ferromagnetic single-domain particle at the saturation magnetization, with a demagnetization factor $\alpha = 5.30$, and with magnetization normal to the 2DES plane. Exactly below the pillar, the fringing field of one pillar is calculated to be $(4\pi$ - $\alpha)M_s = 11000$ G, a substantial value. Yet, considering the distance between the 2DES and the pillars, the fringing field will fan out greatly towards the 2DES, and the return fields will reduce the average value as illustrated in Fig. 3.4(a). To quantitatively estimate $|\bar{B}_z|$ at the middle of the QW layer, each pillar is represented by a magnetic dipole positioned at a height as depicted in Fig. 3.4(b). Each magnetic dipole has a magnetic moment $m = M_s\pi(\frac{d}{2})^2 t = 6.45 \times 10^{-14}$ emu (parameters defined in Fig. 3.4(b)), where $d$ and $t$ are diameter and thickness of the CoFe nanopillar. Then the component normal to the 2DES of the fringing field from one nanopillar can be expressed as:

$$B_z(x,y) = \frac{\mu_0}{4\pi}\frac{m(2z_0^2 - x^2 - y^2)}{(x^2 + y^2 + z_0^2)^{5/2}}. \tag{3.4}$$

Neighboring nanopillars are separated by a distance $R = 200$ nm. The average $|\bar{B}_z|$ over a square of dimensions $R \times R$ centered under each pillar can be calculated as $|\bar{B}_z| = \iint B_z(x,y)dxdy/R^2 = 54$ G. When an increasing number of nanopillars with their respective return fields are taken into account, $|\bar{B}_z|$ decreases and asymptotically approaches 29 G. The value of $|\bar{B}_z|$ extracted from the AL data fits, 35 G, falls within the range found in the theoretical calculations, strongly suggesting that the magnetic fringing fields of the Al/CoFe nanopillars indeed affect our data as described. Figure 3.5 demonstrate the magnetic field distribution over a square of $R \times R$ in the presence of different numbers of CoFe nanopillars. When there are 5 or 9 nanopillars within the square, $|\bar{B}_z| = 42$ G, or 31 G.

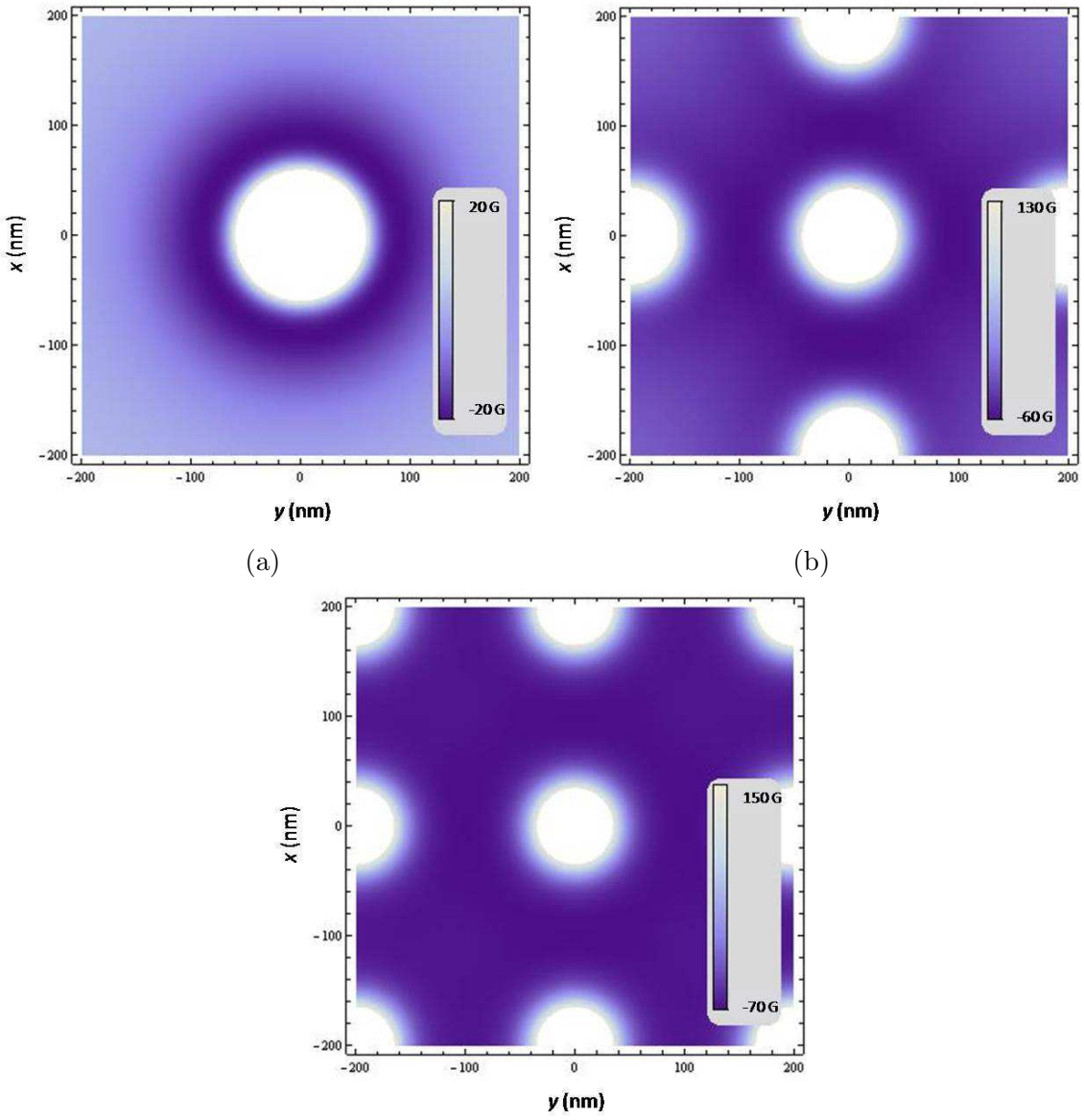


Figure 3.5: The magnetic field distribution at the QW in the presence of (a) one CoFe nanopillar, (b) 5 CoFe nanopillars, and (c) 9 CoFe nanopillars over a square of dimensions $R \times R$.

### 3.4.2 Pseudorandom Field

Concerning the spin-orbit decoherence, for the Al/CoFe sample the spin-orbit scattering rate $\tau_{SO}^{-1}$ is seen to increase with Al/CoFe nanopillar coverage compared to the bare serpentine. This can be explained by the fact that in addition to the average offset field $|\bar{B}_z|$, the ferromagnetic nanopillars also create a spatially varying component to the fringing field. We surmise that the varying component is sensed by the 2DES electron spins as a random spin-orbit field. SOI is experienced by electrons as an effective momentum-dependent vector potential, creating an effective magnetic field $B_{eff}$, in the plane of the 2DES in the case of Rashba SOI [68]. Momentum scattering (quantified by $\tau_0^{-1}$) causes a random component to $B_{eff}$, and the variation in spin precession along the random component causes decoherence between spins, which in the EY mechanism is not mitigated by motional narrowing as in the DP mechanism [69], and hence increases $\tau_{SO}^{-1}$ [10]. Under Al/CoFe nanopillar coverage, electron spins experience an effectively random component of the fringing field, similarly leading to precessional spin decoherence and mimicking SOI-induced spin scattering. Ultimately, the screening effect is counteracted by the effectively random component of $B$, and we observe $\tau_{SO}^{-1}$ increasing under the Al/CoFe nanopillars. Table 3.2 also indicates that for both bare and covered serpentines $\tau_{SO}^{-1}$ stays constant with $T$, consistent with previous discussions [61]. The CoFe nanopillars hence influence the QW electrons in two ways: producing a average offset fringing field $\sim$ 35 G (Fig. 3.6(a)), and inducing a spatially varying pseudorandom field (Fig. 3.6(b)).

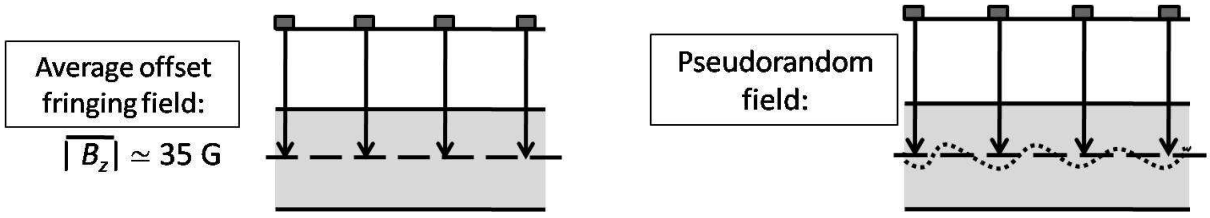


Figure 3.6: Schematics of (a) average offset fringing field and (b) pseudorandom field.

## 3.5 Conclusion

Using antilocalization measurements we observe interactions between two-dimensional electrons in the quantum well of an InGaAs/InAlAs heterostructure and ferromagnetic CoFe nanopillars deposited on the surface. The measurements show that the spin-orbit scattering rate is increased by the ferromagnetic nanopillars, an observation here explained by the presence of a pseudorandom magnetic field component due to the fringing magnetic field of the nanopillars. On the other hand, non-magnetic Al nanopillars are observed to decrease the spin-orbit scattering rate, consistent with increased Coulombic screening under the Elliott-Yafet spin decoherence mechanism. Due to large saturation magnetization and small coercive field of the CoFe nanopillars, an average fringing field normal to the heterostructure surface has to be taken into account as well. The analysis shows that the antilocalization data are in good agreement with expectations deduced from the physics of spin-orbit interactions and simple micromagnetic models.

# Chapter 4

# Interactions between InAs Electrons and Surface Species

Antilocalization (AL) has been widely applied in characterizing the surface states of a variety of solid state materials, among which a recently realized class of material, topological insulators (TI) [15, 21]. TIs possess an insulating interior and exotic metallic surface states that are protected by time reversal symmetry. The electrons travelling on surfaces of topological insulators are insensitive to scattering by impurities, which may provide new routes to generating novel particles, for example induced superconductivity on the surface or Majorana fermions, and thereby become technologically applicable in spintronics and quantum computing.

In a solid state material, the sharp transition from bulk to vacuum leads to an abrupt change of the electronic band structure within a few atomic layers near the surface. New electronic states can now be formed in the weakened potential at the surface, classified as surface states.

The strong spin-orbit coupling in the bulk of topological insulators inverts the conduction band and the valence band, forming a non-trivial topology [22]. When a non-trivial topological insulator is put in contact with vacuum, the band structure of the topological insulator must flip to fit the one in vacuum. The band gap has to close near the edge, thus forming the topologically protected metallic surface states. In the absence of any magnetic scattering, the two-dimensional AL effect can be observed as a consequence of the inherent strong spin-orbit coupling. If magnetic impurities are introduced in topological insulators, the time reversal symmetry will be broken and a gap will open in the Dirac spectrum of the surface states. This transition leads to a variation of the spin orientations, where rich spin configurations and spin-dependent interactions can be explored by AL measurements. Therefore magnetic moments in proximity with a non-magnetic host becomes a promising model to study fundamental and applied phenomena in spin physics and spin-based technologies. In our InAs system, similar metallic surface states also exist here caused by the Fermi level pinning above the conduction band minimum due to donor-like surface states (Fig.1.1(a)). The strong band bending generates a prominent Rashba SOI, manifested in the AL signal in the MR measurements. The presence of these surface states allows us to investigate a variety of spin-spin interactions and exchange mechanisms either between magnetic impurities and the itinerant electrons or between the magnetic moments themselves.

The InAs sample consists of a 3.75 $\mu$m thick $n$-type InAs film (Fig.1.1(b)). To enhance the observed signal, two immediately neighboring twin serpentines are fabricated with channel length of 8820 $\mu$m and width of 40 $\mu$m, as shown in Fig. 2.6. For each experiment and sample, onto only one of the twin mesas the following surface magnetic moments are deposited: rare earth (RE) ions, transition metal (TM) ions, or TM-phthalocyanine (Pc) molecules. The InAs surface accumulation layer is then in direct contact with the magnetic moments, allowing for observations of induced spin-flip scatterings, which are repressed in the InGaAs

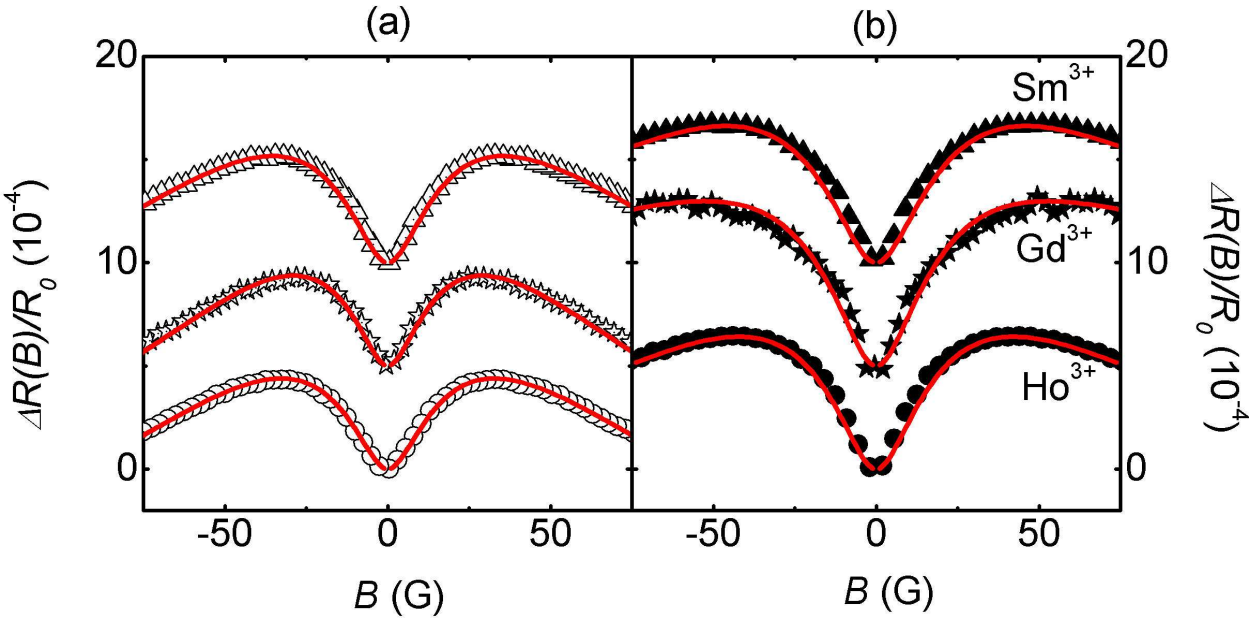


Figure 4.1: (a) Magnetoresistance due to AL at 0.4 K on the bare mesas twinned with the $Sm^{3+}$(up triangles)-, $Gd^{3+}$(stars)- and $Ho^{3+}$(circles)-covered mesas in (b). (b) Magnetoresistance due to AL at 0.4 K on the covered mesas twinned with the bare mesas in (a) (1 out of 6 experimental points are plotted, curves offset by $5.0\times10^{-4}$). Solid lines are theoretical fits. (Ref. [6])

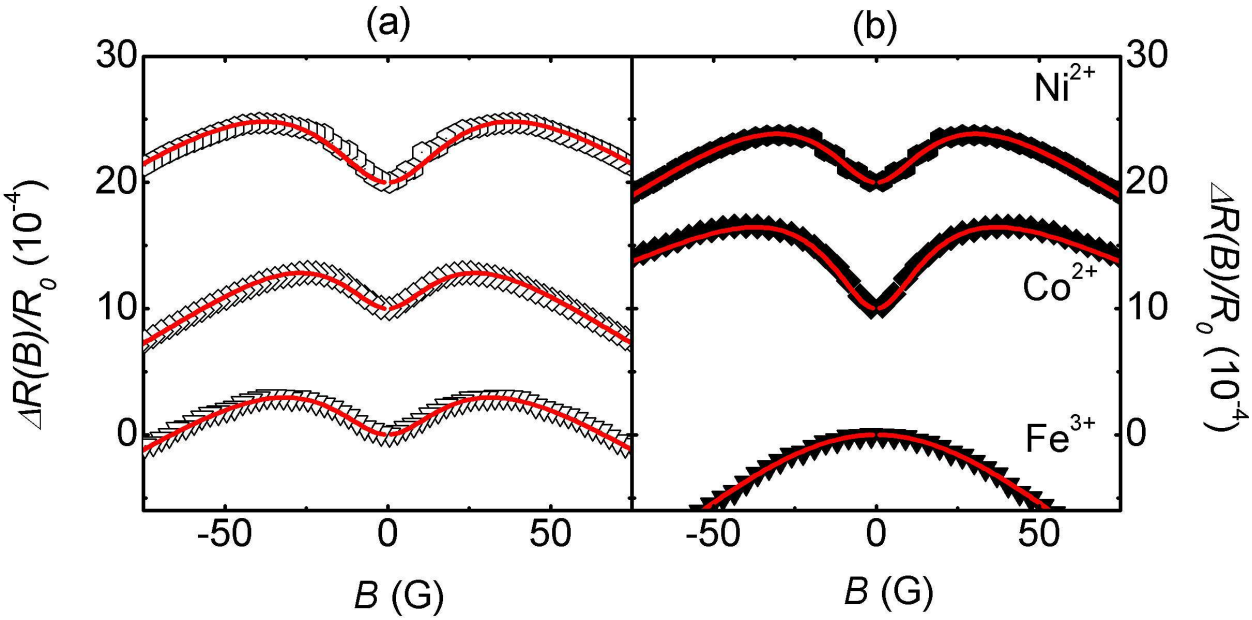


Figure 4.2: (a) Magnetoresistance due to AL at 0.4 K on the bare mesas twinned with the $Ni^{2+}$(hexagons)-, $Co^{2+}$(diamonds)- and $Fe^{3+}$(down triangles)-covered mesas in (b). (b) Magnetoresistance due to AL at 0.4 K on the covered mesas twinned with the bare mesas in (a) (1 out of 6 experimental points are plotted, curves offset by $1.0\times10^{-3}$). Solid lines are theoretical fits. (Ref. [4])

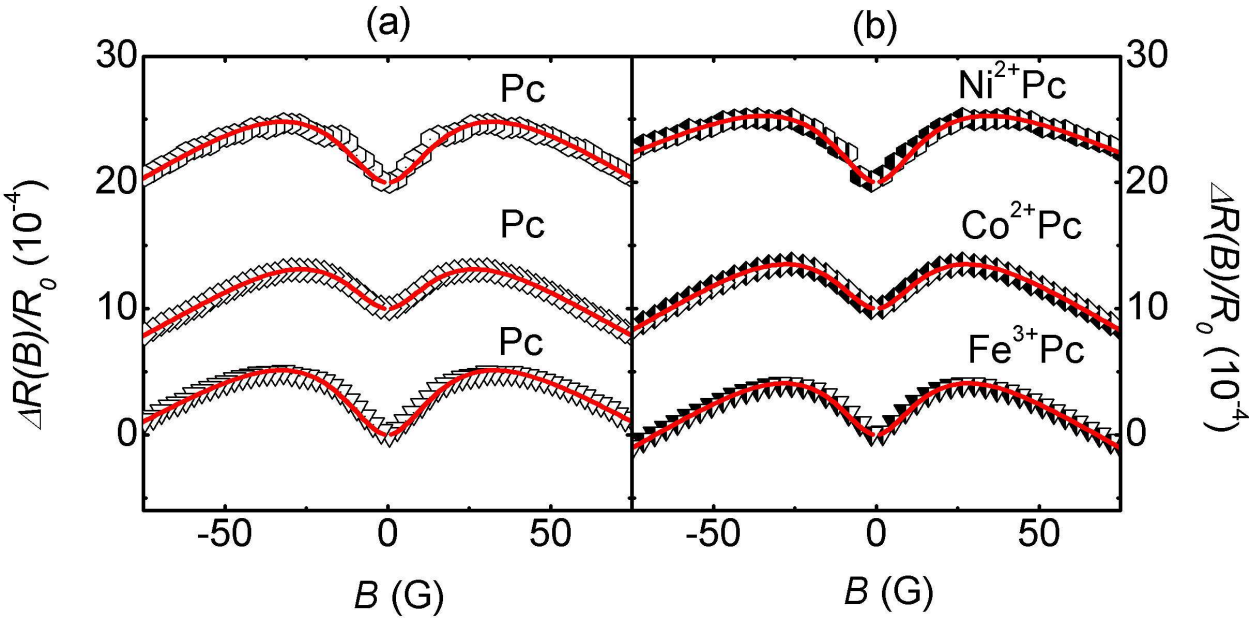


Figure 4.3: (a) Magnetoresistance due to AL at 0.4 K on the Pc-covered mesas twinned with the $Ni^{2+}$Pc(hexagons)-, $Co^{2+}$Pc(diamonds)- and $Fe^{3+}$Pc(down triangles)-covered mesas in (b). (b) Magnetoresistance due to AL at 0.4 K on the covered mesas twinned with the Pc-covered mesas in (a) (1 out of 6 experimental points are plotted, curves offset by $1.0\times10^{-3}$). Solid lines are theoretical fits.

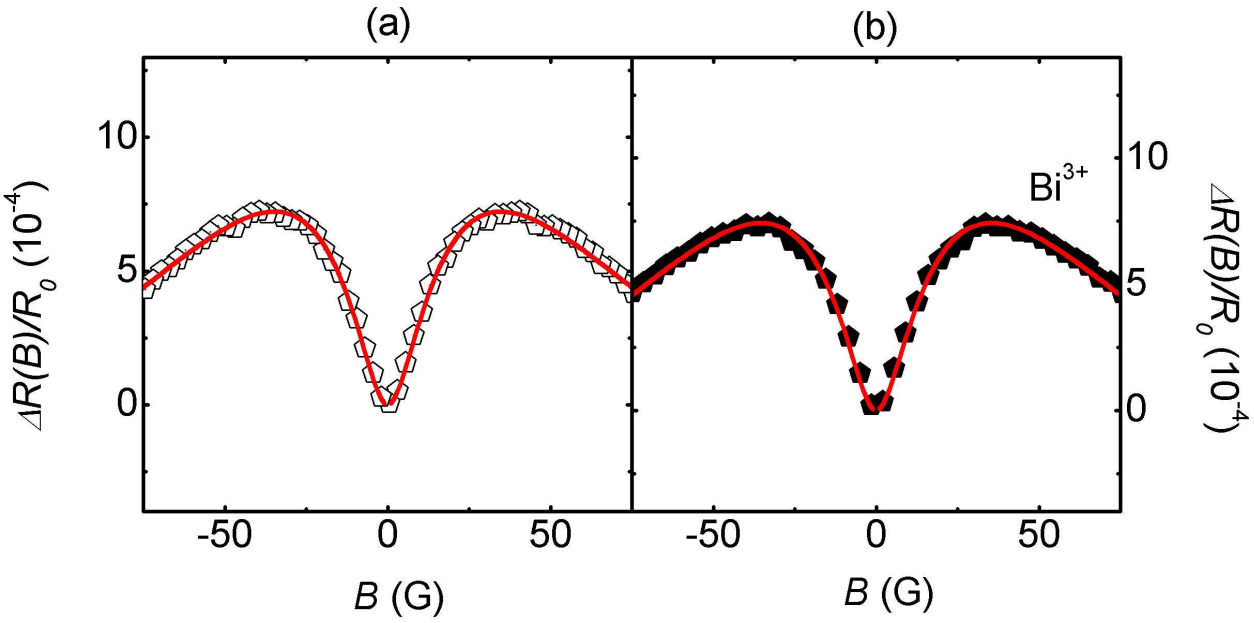


Figure 4.4: (a) Magnetoresistance due to AL at 0.4 K on the bare mesa twinned with the $Bi^{3+}$(pentagon)-covered mesa in (b). (b) Magnetoresistance due to AL at 0.4 K on the covered mesa twinned with the bare mesa in (a) (1 out of 6 experimental points are plotted). Solid lines are theoretical fits.

sample discussed in Chapter 3. Prior to a detailed discussion of the method, its capabilities and its assumptions, in Figs. 4.1, 4.2, and 4.3, we demonstrate the sensitivity of AL to surface species by comparing low-$B$ AL data obtained at a temperature $T = 0.4$ K for twin mesa samples. Clearly differences are observed between the mesa bare of magnetic moments (Figs. 4.1(a), 4.2(a), and 4.3(a)), and the mesa covered with a solution of surface magnetic species and then dried (Figs. 4.1(b), 4.2(b), and 4.3(b)). The air-dried solutions leave a residual film with defined edges. The film forms a visual indication of the surface species concentration on the InAs surface, and reveals a higher concentration (and thus higher surface species effective areal density) at the edge of the deposited area. Atomic force microscopy shows no cluster formation, however. Since the AL results from an average over the serpentine mesas, we infer that the difference in AL between bare and covered mesas reflects a surface species areal density averaged over the covered mesa. While the averaging

limits a detailed study of the dependence on surface species density, the method does allow for a comparative understanding of the interaction between surface electrons and the different surface species, discussed later. In the case of RE and TM ions, the average surface species density is estimated at $n_{SS} \approx 10^6/\mu\text{m}^2$. The solutions are prepared by dissolving nitrate salts in deionized water, and the starting nitrate solutions have the RE and Fe ions in their +3 oxidation states, and Co and Ni in +2 oxidation states. All these states are relatively stable [70, 7]. Given the low concentration of the solutions ($6 \times 10^{-4}$ M) and the complete solubility of the nitrate salts, RE and TM nitrates are appreciably hydrated, reducing the probability that RE and TM ions will approach each other, interact and bond or hybridize with the substrate. Contributions to the AL signal from the fabrication process, exposure to deionized water, as well as from the nitrate ions, were evaluated. The twin serpentine patterns are fabricated simultaneously, with a deionized water rinse as the final mesa fabrication step. Thus, bare and solution covered mesas experience the same environments and are both exposed to deionized water. Further, a control sample with one bare mesa and one covered by deionized water, and subsequently air-dried, was characterized, and no difference in the AL signal was observed. To assess the contributions of the nitrate ions, a $Bi^{+3}$ nitrate solution of the same concentration as other solutions ($6 \times 10^{-4}$ M) was used. $Bi^{+3}$ ions have a spin angular momentum quantum number $S$=0, and thus any comparative changes in the AL data measured between the $Bi^{+3}$-ion covered versus bare mesa may be attributed solely to the presence of nitrate ions (Fig. 4.4). Inspection of Figs. 4.4(a) and 4.4(b), we do not observe any significant differences in the AL data and thus conclude that the nitrate does not influence our subsequent measurements. Moreover, we do not observe marked differences among the bare mesa MR data, e.g. Fig. 4.1(a). Hence our measurements probe the interactions between the magnetic ions (RE and TM) and the InAs surface electrons. In the case of TM phthalocyanine, one mesa is covered with phthalocyanine (Pc), rather than being left bare, and the other covered with TM-Pc. Both compounds are dissolved in

chloroform, thus the differences in the AL arise from the TM ions contained in the TM-Pc. The twin mesas are part of the same sample, experience the same processing apart from solution coverage, and experience the same cooldown to the experiment $T$ (0.4 K$\leq T \leq$6 K). The AL signals are comparatively measured on the bare and covered twin mesas, and it is from the comparative (rather than absolute) data that conclusions are drawn. Before we present the interpretation of the comparative AL data, we discuss how Figs. 4.1, 4.2, and 4.3 were generated.

Figures 4.1, 4.2, and 4.3 depict comparative AL data — between each bare and covered mesas — of RE, TM, and TM-Pc covered samples respectively. In each case the sequence — bottom to top — is determined by highest effective moment $\mu_{\text{eff}}$ to lowest. Next, we arbitrarily set $\Delta R(B)/R_0 = 0$ at $B = 0$ for the highest $\mu_{\text{eff}}$ metal in each series, e.g. for $Ho^{3+}$ in the RE series (Fig. 4.1(b)). Then, the other traces are offset from the first by a fixed offset value, as indicated in each figure caption. The aim of these plots is to present difference among each series and between series.

RE ions were first chosen as surface species because of their large magnetic moments [71]. All of the RE ions applied increase the spin-orbit scattering and induced spin-flip scattering. Good agreements between data and theoretical fits were achieved. TM ions were then considered. While the RE ions have buried 4f shell electrons responsible for their paramagnetic behavior, the TM ions have their outermost (and not buried) 3d shell electrons responsible for their magnetic properties. Using the same InAs surface, we expect stronger interactions between TM ions and the accumulation electrons. Unlike RE ions enhancing the AL signals (Fig. 4.1), TM ions alter the AL signals in various ways (Fig. 4.2). While $Co^{2+}$ broadens the AL signal, $Ni^{2+}$ and $Fe^{3+}$ reduce the signal. Particularly in the case of $Fe^{3+}$ ions, the AL signal is in fact changed into WL. The significant differences in the AL signal observed for

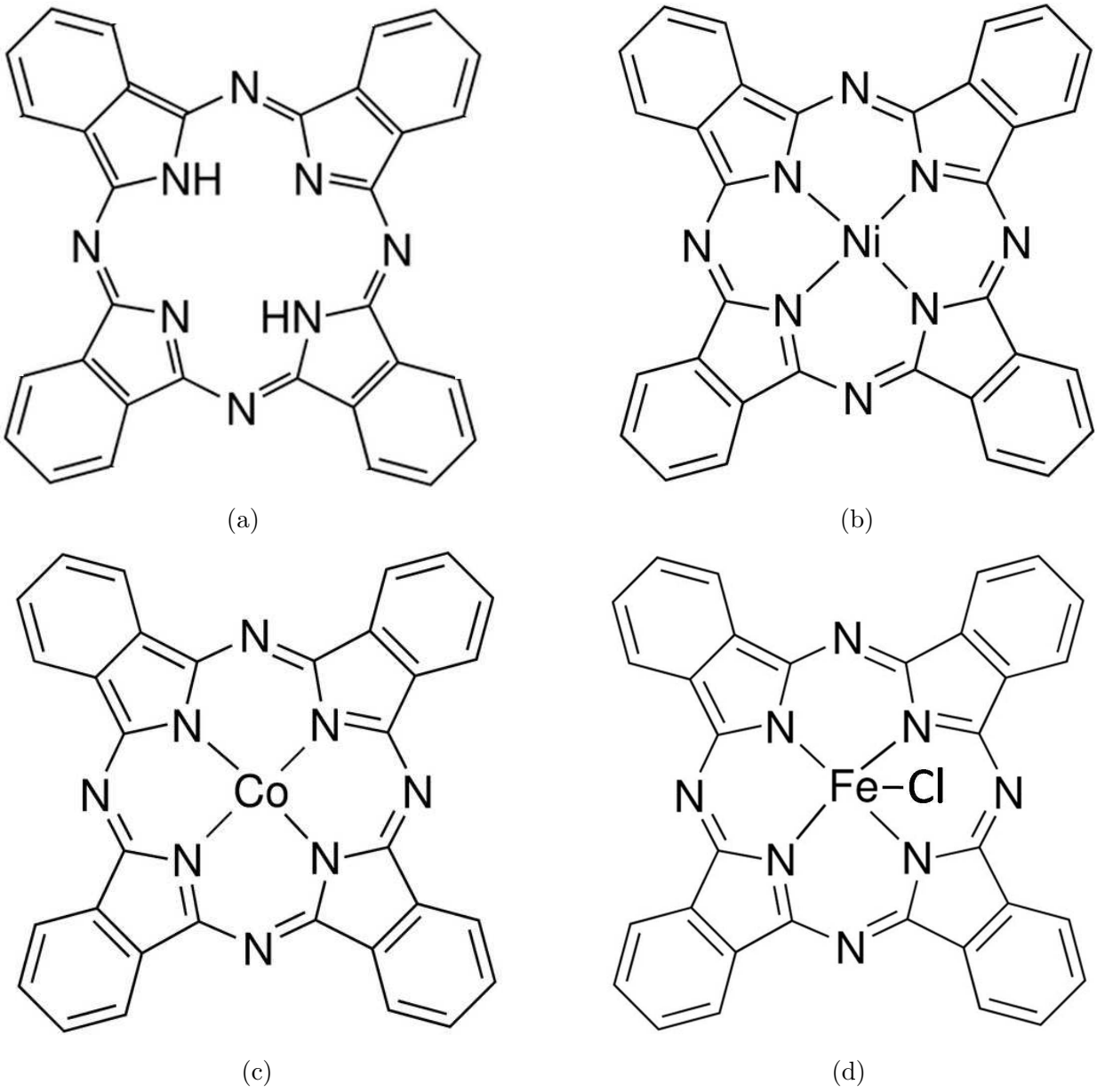


Figure 4.5: Molecular structures of (a) Pc, (b) $Ni^{2+}$-Pc, (c) $Co^{2+}$-Pc, and (d) $Fe^{3+}$-Pc. The molecular formula of Pc is $C_{32}H_{18}N_8$.

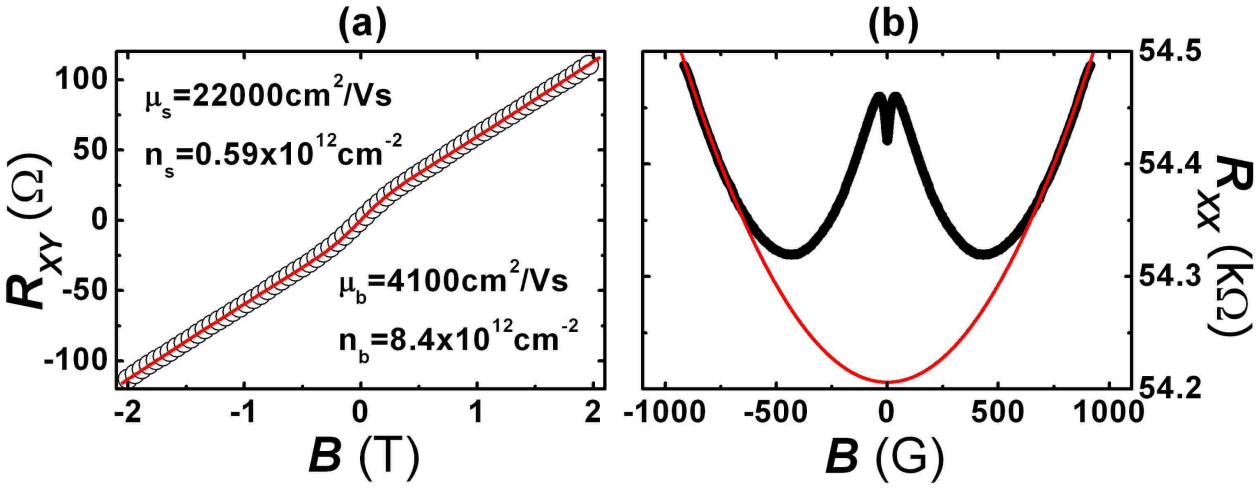


Figure 4.6: (a) $R_{xy}$ and (b) $R_{xx}$ data of a bare InAs accumulation layer at 0.4 K. The circles (a) and the bold line (b) are experimental values (in (a) 1 out of 60 experimental points only are plotted). Fine color lines are fitted curves from the two-carrier analysis, which in (b) leads to a parabolic background in $R_{xx}$.

TM ions may allow probing the interaction of distant local magnetic moments with surface electrons. Thus modified TM ions, here TM-Pc compounds, which have TM ions enclosed within an organic molecule, were also studied. We assume that the phthalocyanine molecules sit roughly flat on the surface, and extrapolate that the TM ions are separated from the surface electrons by a couple of Å. Further, because of the shape of the Pc molecule (Fig. 4.5) and size, 1 nm in length, the areal density is lower. Experimentally, weaker influences on the AL signals are observed (Fig. 4.3); nonetheless, we are able to probe spin-flip scattering.

The transport properties of the InAs accumulation electrons are first discussed before we present quantitative analysis of the AL data. From high-field magnetotransport measurements, the transverse ($R_{XY}$, Hall) and longitudinal ($R_{XX} = R$) transport coefficients can be obtained. Figs. 4.6(a) and (b) display the measurements of $R_{XY}$ and $R_{XX}$ of a bare InAs film, and indicate the presence of two carrier types with different carrier density $n$ and mobility $\mu$. By applying a two-band model (Section 1.3), we assign one type of carrier to the surface accumulation layer electrons with surface density $n_s \sim 0.6 \times 10^{12}$ cm$^{-2}$ and surface mobility

$\mu_s \sim 20000$ cm$^2$/Vs, and the other to the bulk electrons with bulk density $n_b \sim 10^{13}$ cm$^{-2}$ and bulk mobility $\mu_b \sim 5000$ cm$^2$/Vs. Table 4.1 shows the transport properties of surface electrons for each sample studied. For a given sample, mobilities and densities do not vary in the range of the experimental temperatures measured. While mobilities and densities vary among samples, no significant systematic variation caused by solution coverage is observed. The values of $n_s$ are consistent with previous studies [26, 29]. The assignation is confirmed by a self-consistent calculation, using quasi-relativistic dispersion in the InAs, with a Γ-point effective mass of 0.024 and low $T$ band gap of 418 meV (Section 1.6).

From $n_b$ and the InAs layer thickness, the numerical value of $n_{b3\mathrm{D}}$ is calculated to be $\sim 3\times10^{16}$ cm$^{-3}$. Plugging the numerical value of $n_{b3\mathrm{D}}$ into Eq. 1.21, the Fermi level is at 3 meV above $E_C^b$ (Fig. 1.9), indicating a degenerate bulk, and one which exhibits electrical properties similar to those of a metal. The InAs film is unintentionally doped with shallow donors. Therefore, even at low $T$ the donors are still ionized. Bohr radii of the dopant electrons overlap and a splitting of the donor level spreads out into a whole donor band. When the donor band becomes so broad that it merges with the conduction band minimum, $E_F$ then is located inside the conduction band. The trace $E_C^s$ to $E_C^b$ in Fig. 1.9 forms a triangular quantum well close to the surface. Within the triangular quantum well approximation, we use the $n_s$ value obtained from the two-band fitting, and from Eqs. 1.22 and 1.23 locate $E_1$ below $E_F$. $E_2$ falls above $E_F$ indicating a single subband system, consistent with the two-band fit. $E_1$ and $E_2$ are derived to be 43 meV below and 1 meV above $E_F$ respectively. From Eqs. 1.22, 1.23, and 1.24, the electric field $F$ is calculated to be $3.0 \times 10^4$ V/cm, a value reasonably below the breakdown field of InAs ($\sim 5.0 \times 10^4$ V/cm). We then find the width of the triangular well $w_T$ to be $\sim 30$ nm. A good correspondence is observed between $w_T$ and the surface electron Fermi wavelength $\lambda_F^s$ in Table 4.1. $w_T \simeq \lambda_F$ and can be taken as the thickness of the surface layer. Figure 1.9 depicts a schematic band structure and the

probability density ($|\Psi|^2$) associated with the surface electron wavefunction. A downward band bending of 96 meV toward the surface is obtained from the above analysis, pinning the conduction band at $E_C^s$ at the surface, close with the value of 130 meV calculated based on previous studies [29]. The two-band fit is performed for each individual mesa and values of $n_s$ and $\mu_s$ determined, and summarized in Table 4.1.

Table 4.1: Surface accumulation layer electron transport properties: $n_s$, $\mu_s$, $D$, $E_F$, and $\lambda_F^s$ at $T$=0.4 K.

| | | $n_s$ ($10^{12}$ cm$^{-2}$) | $\mu_s$ ($10^4$ cm$^2$/Vs) | $D$ ($10^4$ cm$^2$/s) | $E_F$ (meV) | $\lambda_F^s$ (nm) |
|---|---|---|---|---|---|---|
| $Ho^{3+}$ sample | Covered | 0.61 | 2.4 | 0.12 | 60 | 30 |
| | Bare | 0.55 | 2.1 | 0.09 | 49 | 34 |
| $Gd^{3+}$ sample | Covered | 0.61 | 3.0 | 0.15 | 54 | 32 |
| | Bare | 0.69 | 2.1 | 1.1 | 60 | 30 |
| $Sm^{3+}$ sample | Covered | 0.63 | 2.5 | 0.12 | 55 | 32 |
| | Bare | 0.59 | 2.2 | 0.1 | 52 | 33 |
| $Fe^{3+}$ sample | Covered | 0.6 | 1.7 | 0.08 | 53 | 32 |
| | Bare | 0.69 | 2.2 | 0.12 | 60 | 30 |
| $Co^{2+}$ sample | Covered | 0.75 | 2.2 | 0.13 | 65 | 29 |
| | Bare | 0.8 | 2.3 | 0.14 | 69 | 28 |
| $Ni^{2+}$ sample | Covered | 0.65 | 2.2 | 0.11 | 57 | 31 |
| | Bare | 0.72 | 2.3 | 0.13 | 62 | 30 |
| $Fe^{3+}$Pc sample | $Fe^{3+}$Pc | 0.7 | 2.3 | 0.12 | 61 | 30 |
| | Pc | 0.75 | 2.4 | 0.14 | 65 | 29 |
| $Co^{2+}$Pc sample | $Co^{2+}$Pc | 0.75 | 2.3 | 0.13 | 65 | 29 |
| | Pc | 0.85 | 2.4 | 0.15 | 72 | 27 |
| $Ni^{2+}$Pc sample | $Ni^{2+}$Pc | 0.69 | 2.2 | 0.12 | 60 | 30 |
| | Pc | 0.74 | 2.3 | 0.13 | 64 | 29 |

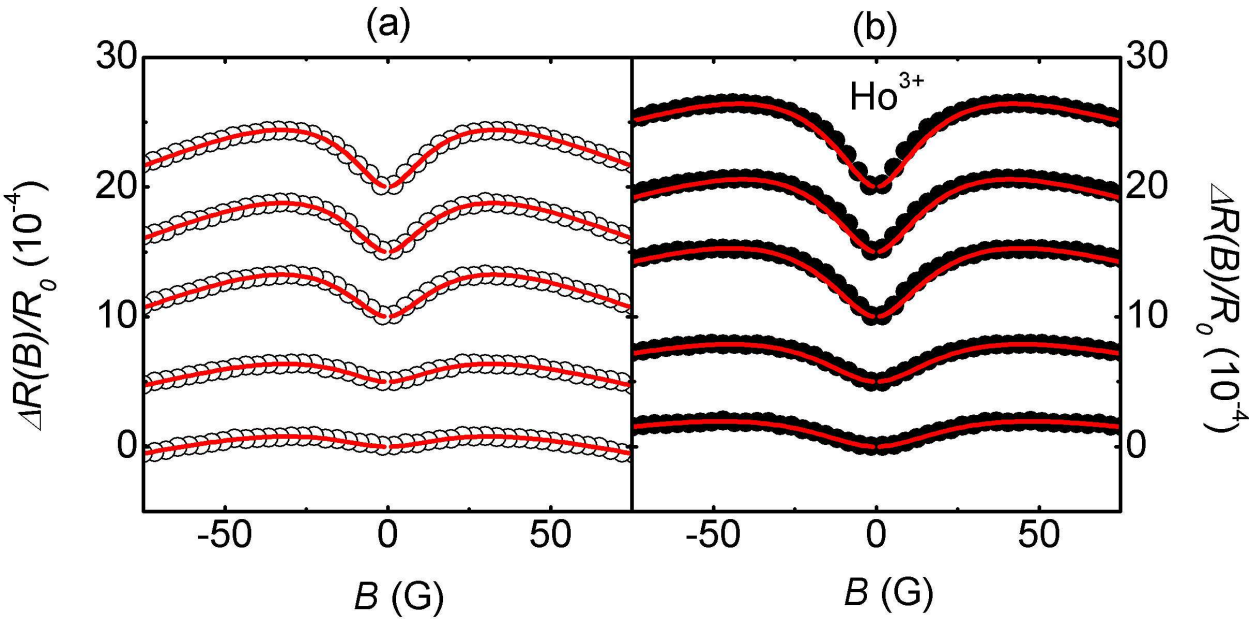


Figure 4.7: (a) Magnetoresistance due to AL on bare mesa and (b) on covered mesa, both of the $Ho^{3+}$ sample at (from top to bottom) $T$=0.4, 0.7, 1.3, 3.0 and 5.0 K (1 out of 6 experimental points are plotted, curves offset by $5.0\times10^{-4}$). Solid lines are theoretical fits.

Experimentally obtained magnetoresistance (MR) data is treated, where the parabolic background due to the classical two-band MR is subtracted (Fig. 4.6(b)). The expression used for the AL correction to the conductivity is given by Eq. 1.16. On the bare mesas, no intentional magnetic impurities are introduced, and we assume $B_s \to 0$, resulting in $B_i$ and $B_{SO}$ being determined from the data. From experiments on metal systems [12, 18, 19, 20, 14] it is known that magnetic impurities introduce spin-flip scattering and additional spin-orbit scattering, but do not affect inelastic scattering. Thus $\tau_i$ can be assumed the same for bare and covered twin mesas fabricated on the same sample. This $\tau_i$ yields a value for $B_i$ for the corresponding covered mesa by using $B_i = \hbar/4eD\tau_i$, where $D$ is as measured in the covered mesa (Table 4.1). Next $B_{SO}$ and $B_s$ are determined for the covered mesa by fitting Eq. (1.16). By this method $\tau_i$, $\tau_{SO}$ and $\tau_s$ are obtained for the covered mesas and $\tau_i$ and $\tau_{SO}$ for the bare mesas with $\tau_s \to \infty$.

Figure 4.7 uses the $Ho^{3+}$ sample as example to show the correspondence between the data and the theoretical fit for both bare and covered mesas at different $T$. A 7% variation in $\tau_i$, $\tau_{SO}$ and $\tau_s$ can be applied to the values obtained from the fits and still obtain a good correspondence with the data, and thus 7% error bars are applied to the remainder of the work. Different fitting models apart from Eq. (1.16) also lead to different values, varying by up to 30%. However, it is important to note that the relative values of $\tau_i$, $\tau_{SO}$ and $\tau_s$ between bare and solution-covered twin mesas, and between different $T$ values, do not vary significantly if the same model is applied consistently. Likewise, the uncertainty in transport parameters (such as $D$), will not affect the relative values of $\tau_i$, $\tau_{SO}$ and $\tau_s$. Hence reliable information can be drawn from the comparative trends related to the RE ion and under varying $T$, although absolute values for the scattering times cannot be quoted to better than 30%. Experimental data and associated fits for the RE ions $Sm^{3+}$ and $Gd^{3+}$, as a function of $T$, are presented in Figs. 4.8 and 4.9 respectively. Scattering rates for the 3 RE ions, as a function of $T$, are presented in Fig. 4.10 and in Fig. 4.11, and where the spin-flip rate for the RE covered mesas is plotted as a function of square root of $T$ (Fig. 4.11). The modification of the scattering rates due to the presence of the RE ions is assigned predominantly to the single-subband surface electrons and not to the bulk electrons, since the proximity of the surface electrons to the surface local moments enhances the interactions. The AL analysis also proceeds under the approximation that we may neglect the AL contribution from the bulk layer without introducing substantial distortion of the results. This approximation rests on the fact that SOI in the bulk is small compared to the strong Rashba SOI at the surface, and hence the bulk contribution to the AL signal is expected to be smaller than the surface contribution. Moreover, the twin-mesa comparative approach (bare *vs* covered mesas) emphasizes the difference in AL signal due to RE ion coverage, a difference likely to be dominated by the surface contribution. In the AL analysis we have also neglected the electron-electron scattering between surface and bulk electrons,

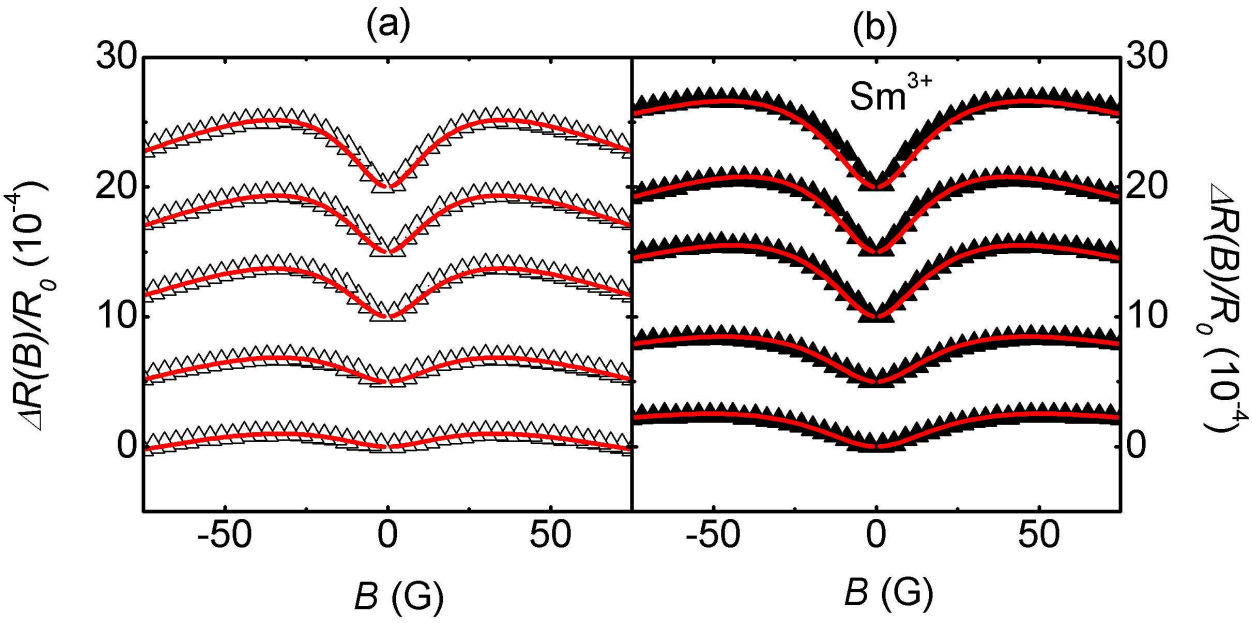


Figure 4.8: (a) Magnetoresistance due to AL on bare mesa and (b) on covered mesa, both of the $Sm^{3+}$ sample at (from top to bottom) $T$=0.4, 0.7, 1.3, 3.0 and 5.0 K (1 out of 6 experimental points are plotted, curves offset by $5.0\times10^{-4}$). Solid lines are theoretical fits.

because an upper bound for the electron-electron scattering rate $\tau_{ee}^{-1}$ can be estimated [72] to lie in the range $0.3 \times 10^{10}$ s$^{-1}$< $\tau_{ee}^{-1}$ < $5 \times 10^{10}$ s$^{-1}$ for 0.4 K≤ $T$ ≤6 K. The rate $\tau_{ee}^{-1}$ is thus expected to be about an order of magnitude slower than other scattering rates, $10^{11}$ s$^{-1}$< $\tau_{\alpha}^{-1}$ < $10^{12}$ s$^{-1}$ ($\alpha = i, SO, s$), and thus neglecting electron-electron scattering, especially between spatially separated surface and bulk electrons, is justified.

## 4.1 Rare Earth Samples

Prior to discussing the scattering rates derived from the AL data of the RE samples, the fitting results are demonstrated in Figs. 4.8, 4.9, and 4.7 for the $Sm^{3+}$, $Gd^{3+}$, and $Ho^{3+}$ samples respectively. Qualitatively, the differences in the resistance minimum dip of AL data between the bare and the covered mesas are almost unvaried for the $Sm^{3+}$ sample and

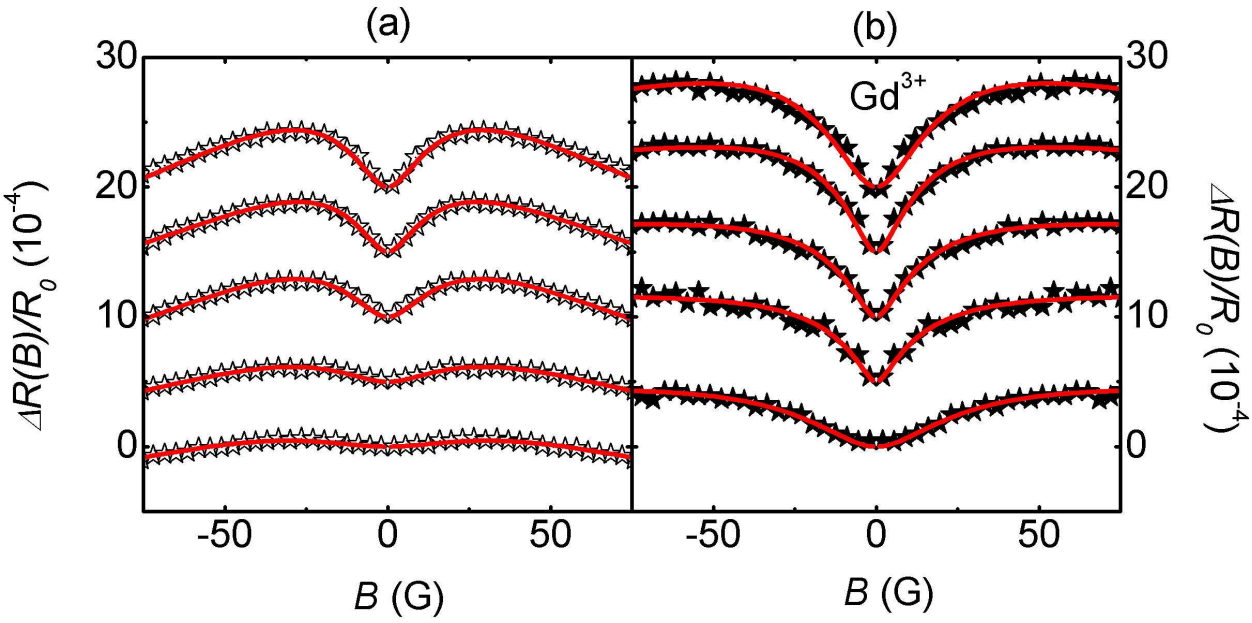


Figure 4.9: (a) Magnetoresistance due to AL on bare mesa and (b) on covered mesa, both of the $Gd^{3+}$ sample at (from top to bottom) $T$=0.4, 0.7, 1.3, 3.0 and 5.0 K (1 out of 6 experimental points are plotted, curves offset by $5.0\times10^{-4}$). Solid lines are theoretical fits.

the $Gd^{3+}$ sample. This difference is mainly determined by spin-flip scattering rate $\tau_s^{-1}$, and roughly $\sim \tau_s^{-1}$. Yet in the $Ho^{3+}$ sample, the differences decrease as $T$ increases, suggesting an increase in $\tau_s^{-1}$ as $T$ increases.

Four different dephasing processes coexist in metal and semiconductor mesoscopic structures. Typically only one or two mechanisms may dominate depending on the system dimensionality, the level of disorder, and the measurement temperature. In three-dimensional weakly disordered conductors, electron–phonon scattering is the sole dominant inelastic dephasing process [73, 74], where $\tau_i^{-1} \propto T^3$. In three-dimensional strongly disordered conductors, electron-electron scattering dominate over the electron-phonon scattering [75], where $\tau_i^{-1} \propto T$. In metals and semiconductors at low $T$ (a few kelvin), the Nyquist decoherence mechanism, which has different $\tau_i^{-1}(T)$ relations depending on dimensionality, is the dominant dephasing process. In mesoscopic systems at very low temperatures, the dephasing

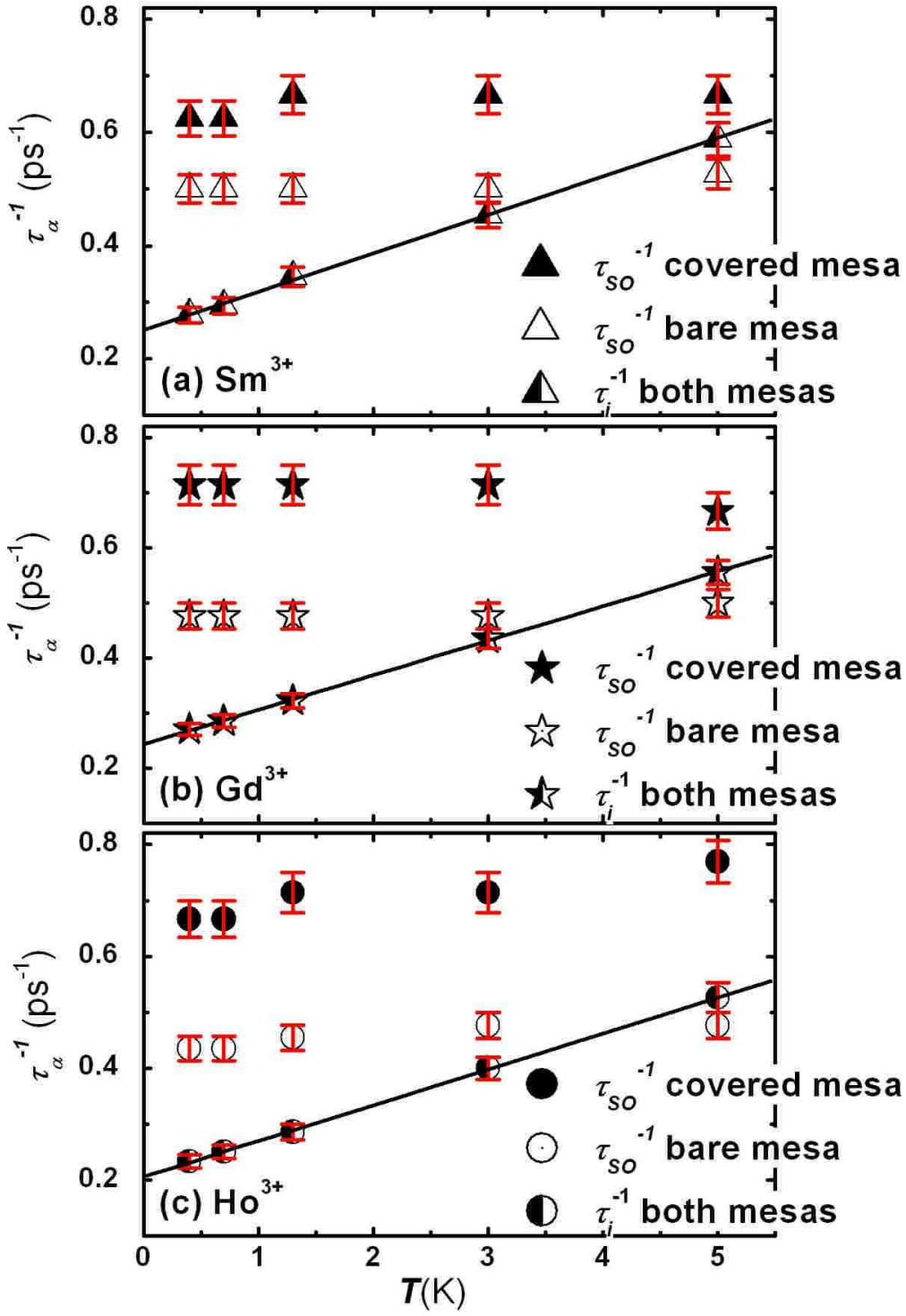


Figure 4.10: Different scattering rates $\tau_\alpha^{-1}$ ($\alpha = SO$ or $i$) *vs* $T$ for (a) $Sm^{3+}$(triangles) sample; (b) $Gd^{3+}$(stars) sample; (c) $Ho^{3+}$(circles) sample. In all the graphs solid symbols stand for $\tau_{SO}^{-1}$ of the ion-covered mesa; open symbols stand for $\tau_{SO}^{-1}$ of the bare mesa; half-solid symbols stand for $\tau_i^{-1}$ of both mesas, sharing the same value. Solid lines form guides to the eye. Error bars are indicated.

is saturated, and the $T$-independent $\tau_i^{-1}$ may be caused by magnetic spin-flip scattering [76, 77]. Within our experiment temperature range (0.4 – 6 K) and our sample InAs, the Nyquist decoherence mechanism is assumed to be the predominant one. This mechanism is a small-energy-transfer electron-electron scattering, and physically such electron-electron collisions are equivalent to the interaction of an electron with the fluctuating electromagnetic field produced by all the other electrons [78]. Nyquist decoherence has $\tau_i^{-1} \propto T^{2/3}$ in one dimension, $\tau_i^{-1} \propto T$ in two dimensions [60], and $\tau_i^{-1} \propto T^{3/2}$ in three dimensions [79]. The accumulation layer at the surface is a 2DES, therefore, $\tau_i^{-1} \propto T$ is expected. Figure 4.10 shows the $T$ dependence of $\tau_i^{-1}$, adopted as common for both bare and RE ion-covered mesas. The linear dependence $\tau_i^{-1} \sim T$ is consistent with dominant Nyquist decoherence in lower dimensions at low temperatures.

The spin-orbit scattering rate $\tau_{SO}^{-1}$ increases in the presence of RE ions, demonstrated by comparisons in Fig. 4.10 (bare *vs* covered). SOI might be influenced by atomic weight, and Fig. 4.10 demonstrates that heavy elements such as the REs can increase the average SOI experienced by carriers in their proximity, leading to the observed experimental result. The increase by adatom coverage has been observed in metal systems [12] and has been proposed as a means of increasing the average SOI in low-SOI systems like graphene [80]. The magnitude of the SOI is determined by the charge on the atomic nucleus, which in turn depends on the atomic number $Z$. In the reference frame of an electron with angular momentum, the nucleus is orbiting around it, and behaves like a circulating electric current proportional to the nucleus charge. In fact the SOI is proportional to $Z^4$ [81]. However, the AL measurements of the sample with heavy $Bi^{3+}$ ions as surface species do not show an increase in $\tau_{SO}$, contradicting the atomic weight argument. The measured SOI arises from the directional electric fields generated by the atomic nucleus of the ions, and the InAs surface electrons, albeit distance-dependent in strength. Therefore, the increase in SOI is

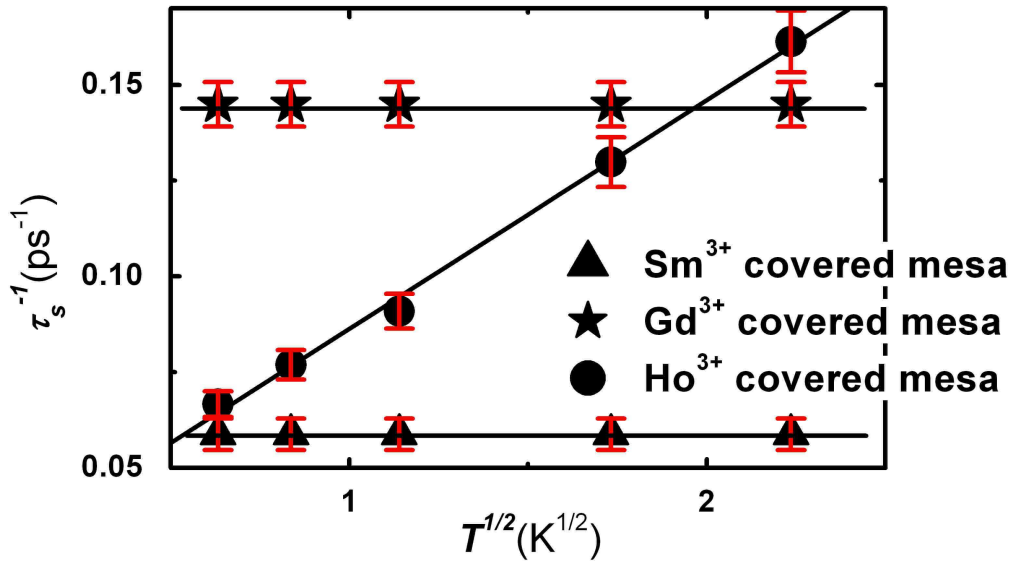


Figure 4.11: The spin-flip rate $\tau_s^{-1}$ of ion-covered mesas *vs* $T^{1/2}$. Solid lines form guides to the eye. Error bars are indicated.

correlated with the electric field determined by $Z$ and the distance between the nucleus and the surface electrons. In the case of $Bi^{3+}$, all of its electron shells are filled completely, and thus they entirely shield the above described electric fields. Accordingly, no increase in $\tau_{SO}^{-1}$ is observed. The RE ions with their 4f shell partially filled are more unshielded than $Bi^{3+}$ ions, and hence the observed SOI. Compared with the magnetic scattering which requires short distances between local moments and the surrounding electrons, the magnitude of the electric field could still be considerable at longer distances, and thereby its influence on the spin-orbit scattering is a long-range interaction. Figure 4.10 indicates that for both bare and covered mesas $\tau_{SO}^{-1}$ is not strongly $T$-dependent within the experiment range of $T$, consistent with previous discussions [61]. The residual $T$-dependence and the small differences in relative magnitudes of the increase in $\tau_{SO}^{-1}$ dependent on RE ion, are the result of several competing effects such as electric field strengths, electron configurations, interaction distances, etc, and must be relegated to a detailed study of their chemical properties.

Figure 4.11 indicates that the spin-flip rate $\tau_s^{-1}$ is strongly influenced by the type of RE ion

deposited. A magnetic interaction $\boldsymbol{\sigma} \cdot \mathbf{S}$ between local RE moments $\mathbf{S}$ and electron spins $\boldsymbol{\sigma}$ hence exists, where $\mathbf{S}$ denotes the total spin of the RE ion 4f electrons. The presence of the interaction is borne out in Fig. 4.11 by the influence of the ions on $\tau_s^{-1}$, showing a modification of the electron spin states in the presence of the RE ions. $Sm^{3+}$, $Gd^{3+}$, and $Ho^{3+}$ differ in the magnitude of the spin-flip rate they impart, as well as its dependence on $T$, properties which are discussed below. Free from a substrate the RE ions are characterized by paramagnetic behavior with $\mu_{\text{eff}}$ due to partially filled 4f shells. The effective moments $\mu_{\text{eff}}$ are expressed in Bohr magnetons ($\mu_B$), with $Sm^{3+}$ having $\mu_{\text{eff}} = 1.5\mu_B$, $Gd^{3+}$ having $\mu_{\text{eff}} = 8.0\mu_B$, and $Ho^{3+}$ having $\mu_{\text{eff}} = 10.4\mu_B$. The spin $S$, orbital $L$ and total angular momentum quantum numbers $J$ of the RE ions in their ground state are as follows, following Hund's rules: $Sm^{3+}$ has $S$=$\frac{5}{2}$, $L$=5 and $J$=$\frac{5}{2}$; $Gd^{3+}$ has $S$=$\frac{7}{2}$, $L$=0 and $J$=$\frac{7}{2}$; $Ho^{3+}$ has $S$=2, $L$=6 and $J$=8. One may expect paramagnetic behavior rather than spin-glass behavior to be maintained on a substrate, since the 4f shells are partially shielded by the outermost s and p shells and crystal field effects will hence be small. To identify the possibility of the paramagnetic system, we have to ascertain how paramagnetic behavior influences $\tau_s^{-1}$.

### 4.1.1 Paramagnetic System

For $Sm^{3+}$ and $Gd^{3+}$ Fig. 4.11 shows a $\tau_s^{-1}$ independent of $T$. The higher spin-flip rate observed for $Gd^{3+}$ correlates with its higher moment (8.0 $\mu_B$, compared to 1.5 $\mu_B$ for $Sm^{3+}$). For $Sm^{3+}$ and $Gd^{3+}$ we observe no $T$ dependence in the data. For $Ho^{3+}$ Fig. 4.11 shows a dependence $\tau_s^{-1} \sim T^n$ with $n \approx \frac{1}{2}$. We note that *paramagnetic* alignment due to the $B$ applied normal to the sample is expected to be negligible. The fraction of the RE ions

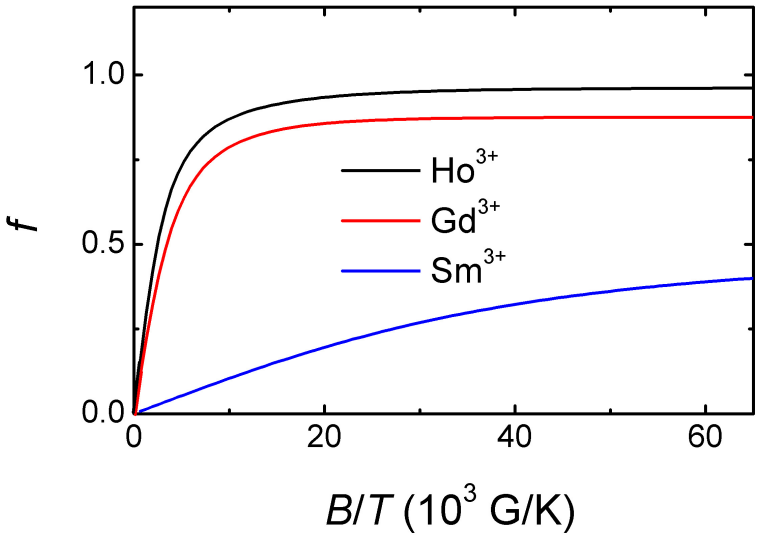


Figure 4.12: The fraction of the RE ions aligned along the applied magnetic field $f$ *vs* $B/T$. The solid lines are calculated curves from Eq. 4.1.

aligned along the applied $B$ can be calculated as

$$f = gJ\mu_B B_J(x)/\mu_{\text{eff}}, \tag{4.1}$$

with $x = gJ\mu_B B/(k_B T)$, and with $g$ the Landé factor given by

$$g = 1 + \frac{J(J+1) + S(S+1) - L(L-1)}{2J(J+1)}, \tag{4.2}$$

$B_J(x)$ the Brillouin function and $k_B$ the Boltzmann constant. In the experimental range analyzed for AL, $B/T$ reaches 300 G/K, at $T = 0.4$ K and $B = 120$ G. A maximal paramagnetic alignment $f$ of 0.32% is then expected for $Sm^{3+}$, 5.2% for $Gd^{3+}$, and 7.2% for $Ho^{3+}$. $g$ is calculated to be 5/4, 2, and 2/7 for $Sm^{3+}$, $Gd^{3+}$, and $Ho^{3+}$ respectively. Equation 4.1 is plotted in Fig. 4.12 for 3 different RE ions, where we can conclude that with $B$ fixed, $f$ decreases as $T$ increases. $f$ is calculated to be 0.025% for $Sm^{3+}$, 0.42% for $Gd^{3+}$, and 0.58% for $Ho^{3+}$ at $T = 5.0$ K and $B = 120$ G. The $f$-values drop substantially between $T = 0.4$

K and $T = 5$ K for $B = 120$ G. This means that at $T = 5$ K we can regard the system as a free-spin system. For a system with 100% paramagnetization transiting into a 100% free-spin system, the spin-slip scattering rate can be maximally increased by $(S+1)/S$ [82]. The effect of the alignment on the average spin-flip rate can be calculated by considering the fraction $f$ of aligned spins and multiplying the rate by $S/(S+1)$ for this fraction. From this calculation, when lowering $T$ from 5 K to 0.4 K paramagnetic alignment is expected at most to reduce $\tau_s^{-1}$ by a factor of 0.999 for $Sm^{3+}$, of 0.988 for $Gd^{3+}$, and of 0.976 for $Ho^{3+}$. The relative reduction in $\tau_s^{-1}$ due to any paramagnetic alignment during the experiment is thus small, and below the measurement threshold for all RE ions. As a consequence, a paramagnetic system is unlikely to be the origin of the observed $T$ dependence of $\tau_s^{-1}$.

### 4.1.2 Kondo Effect

The dependence $\tau_s^{-1} \sim T^{\frac{1}{2}}$ we observe for InAs electrons interacting with $Ho^{3+}$, was also observed in Kondo systems below their Kondo temperature ($T_K$), formed between itinerant electrons and local impurity moments [20, 83]. At low $T$ a single Kondo impurity forms a spin-singlet state with surrounding electrons within a Kondo cloud. Below $T_K$ the moment of the magnetic Kondo impurity is screened by the electrons, and spin-flip scattering is then increasingly suppressed as $T$ is lowered below $T_K$, while reaching a maximum at $T_K$ [47, 19, 14, 84, 85]. The present experiments are limited to $T < 5$ K due to the requirement of quantum coherence for the AL signal. However, from the monotonous decrease in $\tau_s^{-1}$ with decreasing $T$ we deduce that if Kondo physics is indeed active, then the data indicate $T_K > 5$ K [24]. However, in our $n$-InAs system the low electron density and comparatively dense ion coverage, the high spin from the underscreened RE ions, and the strong SOI exclude such a high $T_K > 5$ K. The observed $T$ dependence of $\tau_s^{-1}$ in the $Ho^{3+}$ case can thus not be

explained by the formation of a Kondo system.

### 4.1.3 Spin-Orbit Multiplets

An origin for the $\tau_s^{-1} \sim T^{\frac{1}{2}}$ observed for InAs electrons interacting with $Ho^{3+}$ may lie in the large number of low-lying energy levels generated by the incompletely filled 4f levels of RE ions, leading to characteristically dense energy spectra. For triply ionized RE ions, crystal field effects typically do not lead to a major rearrangement of energy levels [86], and relevant energy levels can thus approximately be identified from $Ho^{3+}$ spectra in various solid-state environments. The existence of spin-flips in the electron system implies a change in $\mathbf{S}$ for the RE ion. We thus want to identify transitions from the $^5I_8$ ground state of $Ho^{3+}$ to states of different $S$, within $k_BT \approx 0.5$ meV from the ground state at our measurement temperatures. The 4f electrons in RE ions form multiplets arising from SOI following the Russell-Saunders approximation, with splitting between multiplet levels of $\lambda \mathbf{L} \cdot \mathbf{S}$, where $\lambda$ is the SOI constant for particular $L$ and $S$ in the RE ion. The multiplet levels are characterized by a $J$ value with $2S+1$ possible values. The energy difference between the ground state $^5I_8$ and the next multiplet member, $^5I_7$, is however 626 meV [87] $\gg 0.5$ meV, and $^5I_8$ and $^5I_7$ share the same $S$=2 value. The excited multiplet $^3K_8$ state of $Ho^{3+}$ however, situated 5.1 meV above $^5I_8$, can answer the criteria for thermally excited spin-flip transitions, especially if the levels are further split or broadened due to proximity to the InAs surface. In previous work [88, 89] it has been noted that the ground state $^5I_8$ has substantial admixture of $^3K_8$ states, reinforcing the possibility of transitions mediated by InAs surface electrons, with accompanying spin-flips. We note that, compared to $Ho^{3+}$, $Sm^{3+}$ has a low $\mu_{\text{eff}} = 1.5\mu_B$ which will reduce the spin-flip rate, while $Gd^{3+}$ has $L$=0, suppressing the splitting due to $\lambda \mathbf{L} \cdot \mathbf{S}$, and hence has a spectrum characterized by a large ($\approx$ 4 eV) gap between its $^8S_{\frac{7}{2}}$ ground state and

the next excited state. Apart from multiplet level splittings, $Ho^{3+}$ is susceptible to other mechanisms leading to finer level structure. From the lifetime of resonance levels, it is known that coupling between crystal electric fields and the hydrated salts of the outlying lanthanide ions such as $Ho^{3+}$ is higher than for mid-series lanthanide ions (here particularly $Gd^{3+}$ but also $Sm^{3+}$) [86, 90]. The higher coupling to the environment for $Ho^{3+}$ may lead to an electric Stark splitting of levels into $2J+1$ closely spaced levels, with a spacing sensitively dependent on the magnitude and symmetry of the environmental electric field. Hyperfine splitting should also be considered [86, 88, 89, 91], particularly again for $Ho^{3+}$ due to the large value for its nuclear magnetic moment (in nuclear magnetons: 4.01 for Ho, compared to -0.21 for Sm and -0.11 for Gd averaged over their isotopes). A splitting of $\sim 1.5$ meV has been quoted [89], in range for thermal excitations in the present experiments although the precise value will depend on environmental factors. An exact quantitative assessment of the transitions responsible for our experimental observation that $\tau_s^{-1} \sim T^{\frac{1}{2}}$ for electrons interacting with $Ho^{3+}$ cannot presently be deduced from the data. It is significant however that the AL measurement of $\tau_s^{-1}$ identifies a pronounced $T$ dependence for $Ho^{3+}$, and a higher spin-flip rate for $Gd^{3+}$ than for $Sm^{3+}$, as these results are indeed borne out from their magnetic moments and energy level spectra.

## 4.2 Transition Metal Samples

Influence of transition metal ions to the AL data is measured for $Ni^{2+}$, $Co^{2+}$, and $Fe^{3+}$ samples, and plotted in Figs. 4.13, 4.14, and 4.15 respectively. Inspecting Figs. 4.1 and 4.2 (RE ions and TM ions), we note that the changes to the AL signal caused by TM ions is varied and more pronounced compared to the influence due to RE ions. In the case of RE ions, they all enlarge the AL signals. However, among the TM samples studied in

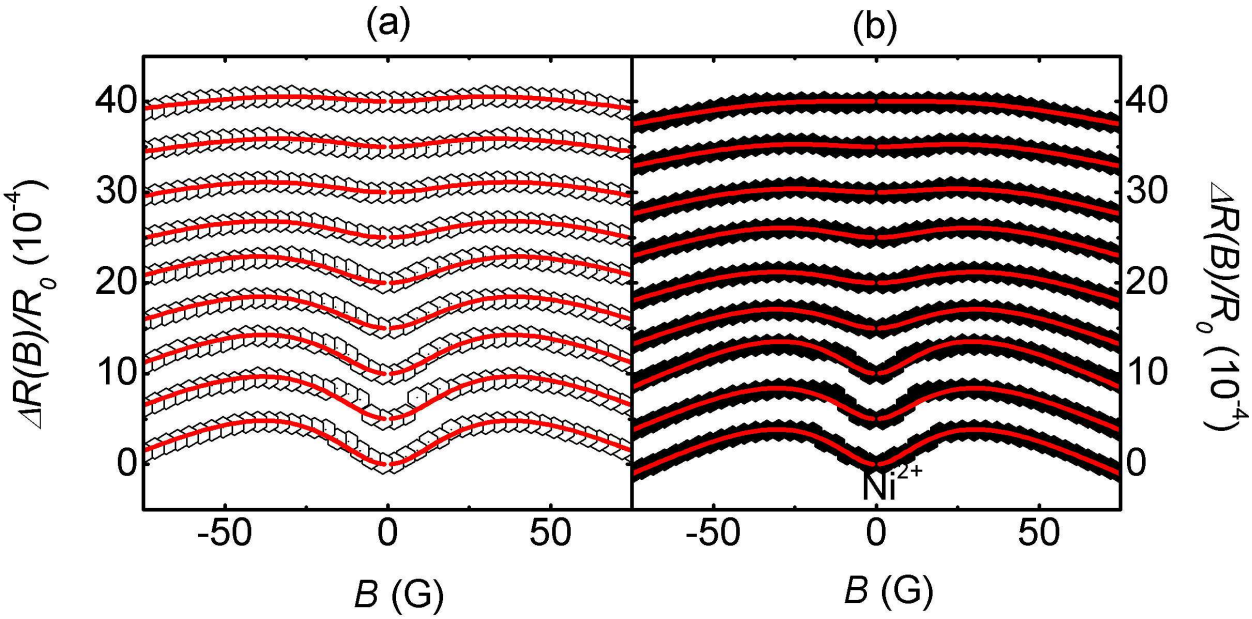


Figure 4.13: (a) Magnetoresistance due to AL on bare mesa and (b) on covered mesa, both of the $Ni^{2+}$ sample at (from bottom to top) $T$ = 0.4, 0.55, 0.7, 1.22, 2.0, 3.0, 4.0, 5.0, and 6.0 K (1 out of 6 experimental points are plotted, curves offset by $5.0\times10^{-4}$). Solid lines are theoretical fits.

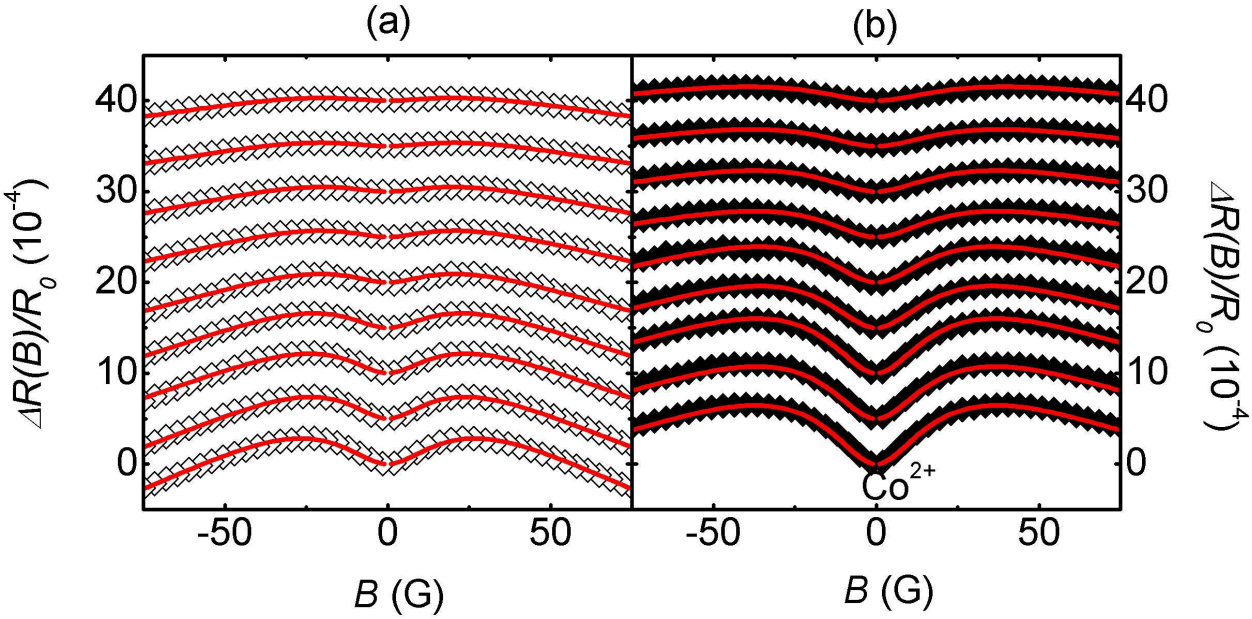


Figure 4.14: (a) Magnetoresistance due to AL on bare mesa and (b) on covered mesa, both of the $Co^{2+}$ sample at (from bottom to top) $T$ = 0.4, 0.55, 0.7, 1.22, 2.0, 3.0, 4.0, 5.0, and 6.0 K (1 out of 6 experimental points are plotted, curves offset by $5.0\times10^{-4}$). Solid lines are theoretical fits.

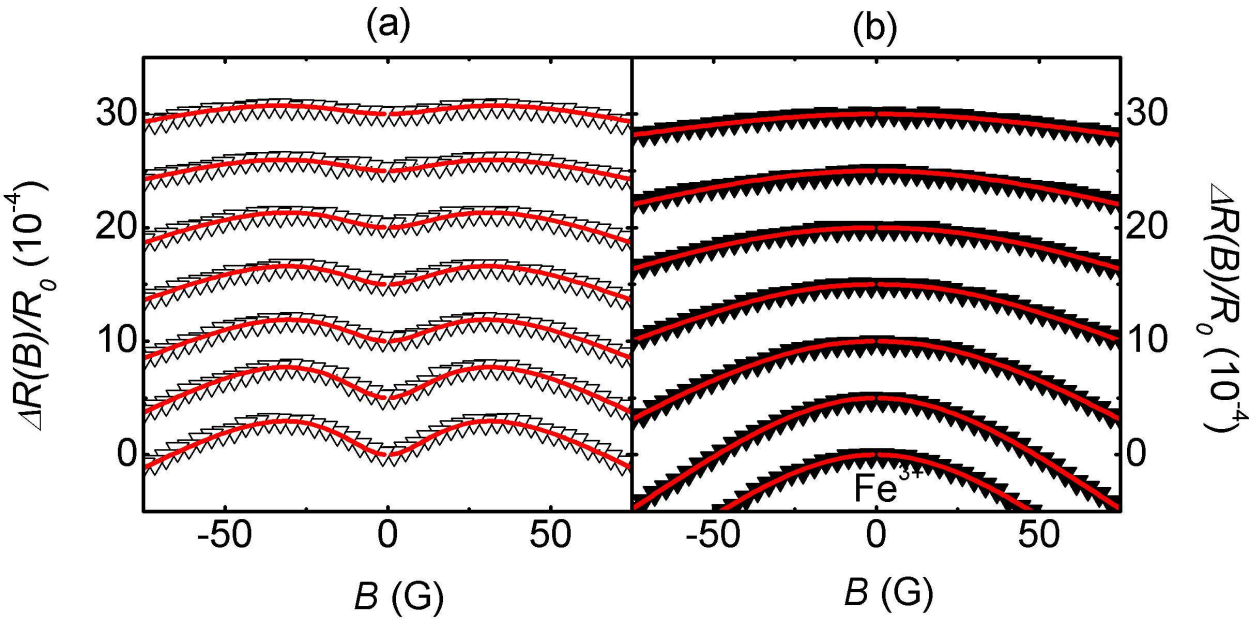


Figure 4.15: (a) Magnetoresistance due to AL on bare mesa and (b) on covered mesa, both of the $Fe^{3+}$ sample at (from bottom to top) $T = 0.4$, 0.55, 1.22, 2.0, 3.0, 4.0, and 6.0 K (1 out of 6 experimental points are plotted, curves offset by $5.0\times10^{-4}$). Solid lines are theoretical fits.

this thesis, only $Co^{2+}$ broadens the signal, while $Ni^{2+}$ and $Fe^{3+}$ reduce the signal. In the case of $Fe^{3+}$ ions, the AL signal is changed to WL. This interesting observation may be explained by considering suppression of SOI due to ferromagnetic ordering on the surface [64]. Alternatively, the high spin-flip scattering of the $Ni^{2+}$ and $Fe^{3+}$ ions may cause fast spin decoherence and thus mask the SOI. Further, the AL fitting results shown later support the validity of spin decoherence screening the SOI. In the absence of further experimental investigations, the latter potential explanation is more reasonable as the former indicates a failure for $Co^{2+}$ ions to be ferromagnetically ordered.

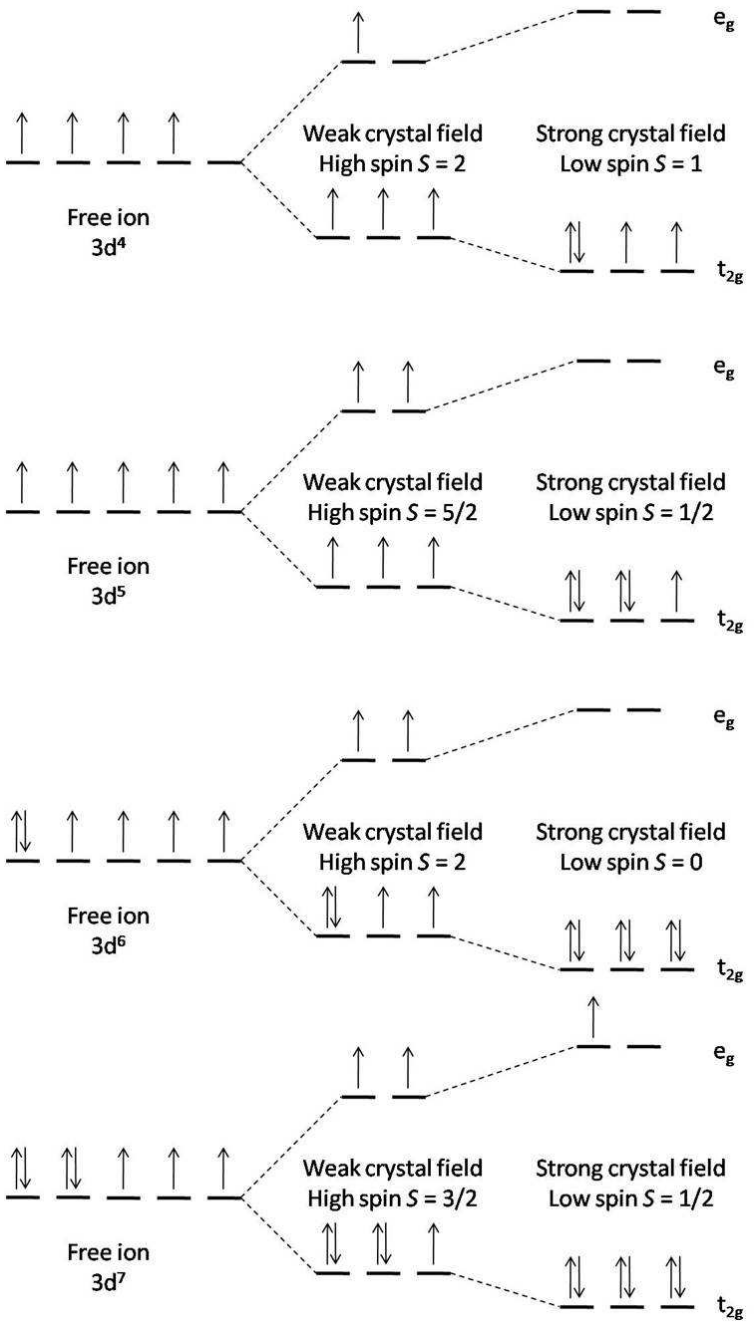


Figure 4.16: Low-spin and high-spin states for a TM ion surrounded by six ligands situated at the corners of an octahedron. From up to bottom, the TM ion configuration is $3d^4$, $3d^5$, $3d^6$, and $3d^7$. (Modified from Ref. [7])

### 4.2.1 Crystal Field

The difference in behavior of the RE and TM ions is that the 4f shell responsible for paramagnetism in the RE ions lies deep inside the 5s and 5p shells, whereas in the TM ions the 3d shell responsible for paramagnetism is in the outermost shell. The 3d shell experiences the intense inhomogeneous electric field produced by a surrounding charge distribution (anion neighbors), which is called the crystal field. The interaction of the paramagnetic ions with the crystal field has two major effects. The coupling of **L** and **S** vectors is largely broken, so that the states are no longer specified by their $J$ values, and as a result the spin-orbit multiplets no longer exist in TM ions. Further, the $2L+1$ sublevels belonging to a given $L$ which are degenerate in the free ion may now be split by the crystal field. In a hydrated TM nitrate complex, the interaction between a TM ion and ligands arises from the attraction between the positively charged metal cation and negatively charged $NO_3^{-1}$ anions, and the non-bonding electrons of water molecules. As any ligand approaches the metal ion, the 3d shell electrons closer to the ligands will have a higher energy than those further away, which results in the d–orbitals splitting in energy. This splitting may be affected by several factors, and results in different complexes: octahedral, tetrahedral, and square planar. The hydrated TM nitrates form octahedral complexes. In octahedral geometry the d-orbitals split into two sets, where the $d_{xy}$, $d_{yz}$, and $d_{xz}$ orbitals are degenerate and lower in energy than the other degenerate state containing $d_{z^2}$ and $d_{x^2-y^2}$, with a crystal field splitting energy of $\Delta_{OCT}$. The three lower-energy orbitals are collectively referred to as $t_{2g}$, and the two higher-energy orbitals as $e_g$. Each of the five states has the capacity of two electrons (spin-up and spin-down), and the energy required to pair a spin-up electron and a spin-down electron is defined as pairing energy $E_P$. By comparing $\Delta_{OCT}$ and $E_P$, a $3d^n$ $(4 \leq n \leq 7)$ TM complex can be classified as high-spin or low-spin. When $\Delta_{OCT} > E_P$, electrons will fill up all the spin-up states in the $t_{2g}$ orbitals first and then occupy the spin-down states of these orbitals before

moving to the $e_g$ orbitals. On the other hand, when $\Delta_{OCT} < E_P$, the electrons will occupy all the orbitals first and then pair up, which follows Hund's rule. Figure 4.16 lists both the low-spin and the high-spin scenarios for TM ions with electron configurations from $3d^4$ to $3d^7$.

### 4.2.2 Spin Transition

Among the TM ions used in the experiment, the electron configurations of $Ni^{2+}$, $Co^{2+}$, and $Fe^{3+}$ are $3d^8$, $3d^7$, and $3d^5$ respectively. In an octahedral geometry (for the metal center), high- or low-spin $Ni^{2+}$ states are not distinguishable. But for $Co^{2+}$ and $Fe^{3+}$, there is a difference between high- and low-spin states, and where all these states have non-zero $S$. In fact, from $3d^4$ to $3d^7$, only the low-spin state of $3d^6$ ($Fe^{2+}$) has $S = 0$. For an investigation of spin exchange mechanism, species with high magnetic moments are essential. This is why the Ni and Co ions are in their +2 oxidation states whereas the Fe ion is in +3 oxidation state. The effective moments of the TM ions are related with their $S$, assuming $Ni^{2+}$, $Co^{2+}$, and $Fe^{3+}$ are all in their high-spin states, and have $\mu_{\text{eff}} = 3.2\ \mu_B$, $4.8\ \mu_B$, and $5.4\ \mu_B$ respectively. The spin-flip scattering is supposed to scale with $\mu_{\text{eff}}$ of each TM ion. However, from the qualitative comparison presented at the beginning of this section, the spin-flip scattering introduced by $Co^{2+}$ is the weakest among the three TM ions used in the study, which indicates that $Co^{2+}$ is in its low-spin state with $\mu_{\text{eff}} = 1.9\ \mu_B$. Actually, $3d^6$ and $3d^7$ materials have a tendency to be in low-spin states due to a relatively small value of $E_P$, compared with $3d^4$ and $3d^5$ materials [92]. Like the $Ho^{3+}$ sample, the difference in the height of AL data between the bare and the covered mesas of the $Co^{2+}$ sample also decreases as $T$ increases, implying the existence of a $T$-dependent $\tau_s^{-1}$. In contrast, the $\tau_s^{-1}$ of the $Ni^{2+}$ sample is predicted to be $T$-invariant due to the almost unchanged AL signal

height difference between the twin mesas. The increase in $\tau_s^{-1}$ of the $Co^{2+}$ sample at higher $T$ suggests a transition of $Co^{2+}$ ions from low-spin to high-spin states. A spin transition has been observed in some $3d^n$ $(4 \leq n \leq 7)$ transition metal compounds [93, 94, 95], which can be induced by changing the temperature or the pressure of the system, and thus are mostly characterized by a function of $T$ as $\rho_H = f(T)$ with $\rho_H$ being the molar fraction of ions in the high-spin state. The transition may be abrupt, occurring within a few kelvins range, or smooth, occurring within a large temperature range. Moreover, the $\rho_H = f(T)$ curves may be strictly identical in the cooling or heating modes, or exhibit a hysteresis. Several techniques are currently used to obtain such curves, like Mössbauer spectroscopy, magnetic susceptibility measurements, optical behavior change, or X-ray spectroscopy [93, 95]. Our experiments hint that it is plausible for the spin transition to be probed by AL measurements. Spin transitions exhibit features similarly observed in magnetic and optical transitions, and a bistability that make them relevant for further investigation as storage media [93].

Figure 4.17 shows the $T$ dependence of $\tau_i^{-1}$ for all TM samples. As noted in the figure caption, in each case the bare and its twinned TM-covered mesa have the same values, and thus the data for each bare mesa is omitted. We thus conclude that the surface species coverage does not change the inelastic scattering. The TM samples also have a linear $T$ dependence of $\tau_i^{-1}$, consistent with Nyquist decoherence arising from fluctuations in the electromagnetic background. Figure. 4.18 demonstrates that $\tau_{SO}^{-1}$ increases in the presence of TM ions, contradicting the formation of a ferromagnetic ordering proposed for explaining the reduction of the AL signals. The SOI in the TM ion-covered mesas are actually all strengthened rather than suppressed, and this is understandable if we consider SOI produced by electric fields from the nuclei of TM ions, consistent with the RE case. Nevertheless, the increase in $\tau_{SO}^{-1}$ for each TM ion and the differences in relative magnitudes of the increase in $\tau_{SO}^{-1}$ caused by the TM ions are both larger than those in the RE samples, indicating a stronger

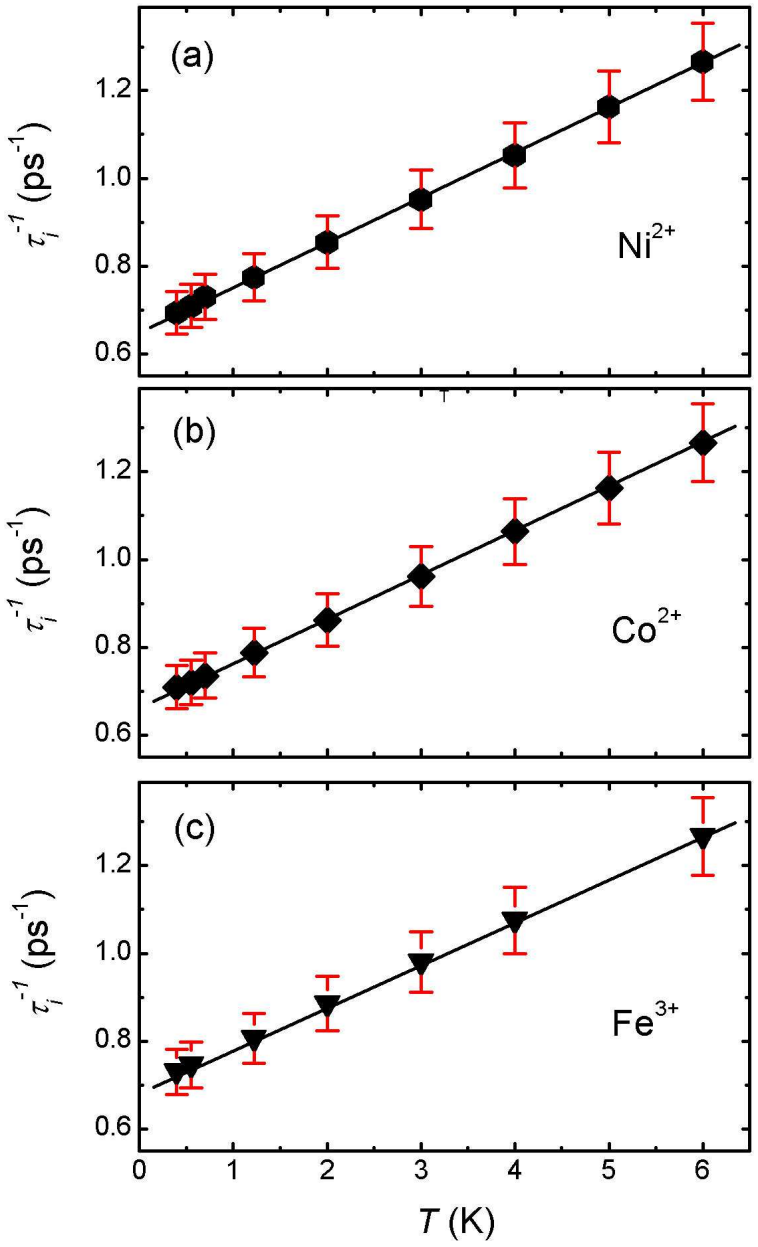


Figure 4.17: Inelastic scattering rates $\tau_i^{-1}$ *vs* $T$ for (a) $Ni^{2+}$(hexagons) sample; (b) $Co^{2+}$(diamonds) sample; (c) $Fe^{3+}$(down triangles) sample. The ion-covered mesa and the bare mesa share the same value, and thus values for bare mesas are omitted. Solid lines form guides to the eye. Error bars are indicated.

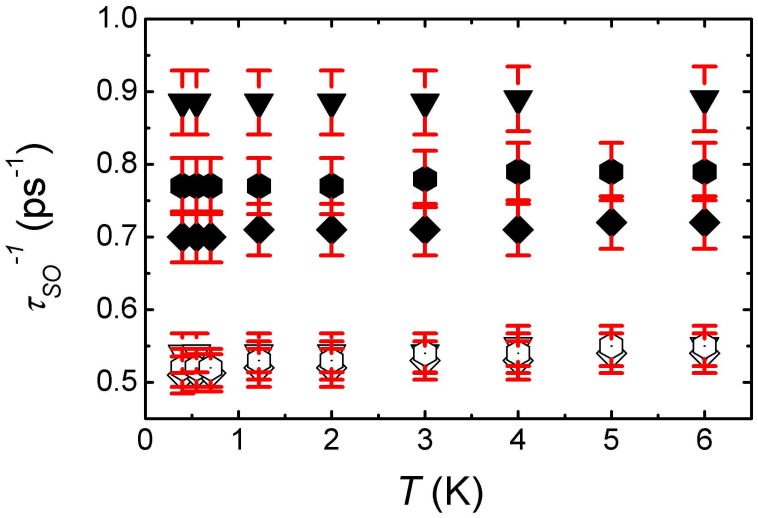


Figure 4.18: Spin-orbit scattering rates $\tau_{SO}^{-1}$ *vs* $T$ for the $Ni^{2+}$(hexagons) sample, the $Co^{2+}$(diamonds) sample, and the $Fe^{3+}$(down triangles) sample. In all the graphs solid symbols stand for the ion-covered mesa; open symbols stand for the bare mesa. Error bars are indicated.

long-range interaction as expected from the analysis of their electron configurations. In fact, with 3d electrons being on the outermost shell, TM ions are more likely to interact with the itinerant electrons, or with the substrate atoms. In addition, the crystal field, hindered by the 5s and 5p electrons in RE ions, is robust in the case of TM ions. Accordingly, stronger SOI is generated by the TM ions and scaled with the electric field. In Fig. 4.18, $Fe^{3+}$ causes the largest increase in $\tau_{SO}$, which could be explained by its +3 oxidation state. In the case of $Ni^{2+}$ and $Co^{2+}$, both in their +2 oxidation state, the more active $Ni^{2+}$ causes the slightly larger increase of the spin-orbit scattering. The modifications to the SOI are a result of long-range interactions between surface magnetic impurities and the electrons, and may be modified by the nature of the ion, and the distance of the ion to the surface, or coverage density. In Section 4.3 we discuss TM phthalocyanine complexes where the distance of the TM ions to the surface electrons may be different than in the TM nitrate case, and where coverage density is also different due to the size of the phthalocyanine molecule.

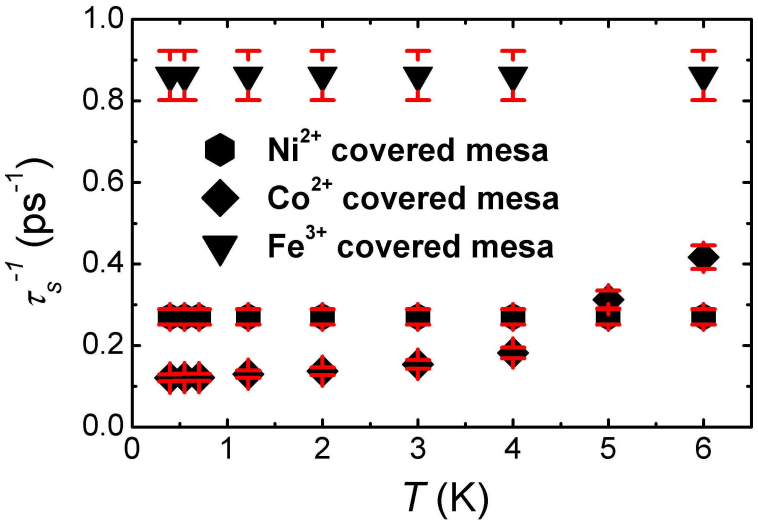


Figure 4.19: The spin-flip rate $\tau_s^{-1}$ of ion-covered mesas *vs* $T$. Error bars are indicated.

Before discussing the difference of spin-orbit scattering between bare ($\tau_{SO}^{-1}|_{bare}$) and ion-covered ($\tau_{SO}^{-1}|_{cov}$) mesas, and the difference of spin-flip scattering between bare ($\tau_s^{-1}|_{bare} = 0$) and ion-covered ($\tau_s^{-1}|_{cov} = \tau_s^{-1}$) mesas, we define

$$\begin{aligned} \Delta\tau_{SO}^{-1} &= \tau_{SO}^{-1}|_{cov} - \tau_{SO}^{-1}|_{bare}, \\ \Delta\tau_s^{-1} &= \tau_s^{-1}|_{cov} - \tau_s^{-1}|_{bare} = \tau_s^{-1}. \end{aligned} \tag{4.3}$$

The increased spin-orbit scattering $\Delta\tau_{SO}^{-1}$ is supposed to lead to stronger AL signals. However, when $\tau_s^{-1}$ is comparable with $\Delta\tau_{SO}^{-1}$, the spin flips disturb the spin phase in the AL interference, and thus mask the effect of spin-orbit scattering. The electron waves are less coherent at the incident point in AL, resulting in weaker AL signals. Hence, the shape of the AL signals are changed in opposing directions due to $\Delta\tau_{SO}^{-1}$ and $\tau_s^{-1}$: while $\Delta\tau_{SO}^{-1}$ broadens the signal, $\tau_s^{-1}$ shrinks it. From Fig. 4.18, the spin-flip rate caused by $Fe^{3+}$, $Ni^{2+}$, and $Co^{2+}$ ions are arranged from high to low. The ratios of $\tau_s^{-1}/\Delta\tau_{SO}^{-1}$ at $T = 0.4$ K are 2.5, 1.1, and 0.5 for the $Fe^{3+}$, $Ni^{2+}$, and $Co^{2+}$ samples respectively. From Fig. 4.15, the AL signal changes to WL, indicating that the spin-flip scattering influences the $Fe^{3+}$ sample the most,

and counter and suppress the influence of SOI in this sample. In the $Ni^{2+}$ and $Co^{2+}$ samples the SOI is less suppressed, inferred from the observation that the AL signal in these two cases does not change to WL. In the $Ni^{2+}$ sample the AL signal is narrowed and lowered, while for the $Co^{2+}$ sample, it is broadened and increased, indicating a neutral position of the signal variation is between $\Delta\tau_s^{-1}/\Delta\tau_{SO}^{-1} = \tau_s^{-1}/\Delta\tau_{SO}^{-1} = 1.1$ and 0.6.

Comparing Fig. 4.19 and Fig. 4.11, the spin-flip scattering introduced by TM ions are much stronger than those by RE ions, and hence cause a stronger $\boldsymbol{\sigma}\cdot\mathbf{S}$ interaction between local TM moments from the 3d electrons and the electron spins of the surface. Clearly indicated from the two $\tau_s^{-1}$ *vs* $T$ figures, the influence on $\tau_s^{-1}$ strongly depends on the type of ions deposited. As observed in Fig. 4.19, magnetic scattering caused by $Ni^{2+}$ and $Fe^{3+}$ are independent of $T$, and a saturation region of $\tau_s^{-1}$ exists in the $Co^{2+}$ sample below 2 K. Within this saturation range, the spin-flip scattering scales with $\mu_{\text{eff}}$ of the ion, indicating a correlation between them. It is realized that $Fe^{3+}$ and $Co^{2+}$ have bistability in spin states with $Fe^{3+}$ having high-spin $\mu_{\text{eff}} = 5.9\mu_B$ and low-spin $\mu_{\text{eff}} = 1.9\mu_B$, and $Co^{2+}$ having high-spin $\mu_{\text{eff}} = 4.8\mu_B$ and low-spin $\mu_{\text{eff}} = 1.9\mu_B$. $Ni^{2+}$ has a single spin state with $\mu_{\text{eff}} = 3.2\mu_B$. To further discuss the $T$ dependence of $\tau_s^{-1}$, we have to identify which of the two spin states is at play for $Fe^{3+}$ and $Co^{2+}$. From Fig. 4.19, we note that the $\tau_s^{-1}$ for the $Ni^{2+}$ sample stays roughly the same as a function of $T$, and thus we use $Ni^{2+}$ as the reference against which we compare $Co^{2+}$ and $Fe^{3+}$. $Fe^{3+}$ has a higher $\mu_{\text{eff}}$ than $Ni^{2+}$ concluded from a higher $\tau_s^{-1}$, which ascertains that $Fe^{3+}$ stays in its high-spin state. The spin-flip rate of the $Co^{2+}$ sample is below that of $Ni^{2+}$ at lower temperatures, suggesting that the majority of $Co^{2+}$ ions stay in their low-spin state. When $T$ increases, the $Co^{2+}$-covered mesa has higher $\tau_s^{-1}$ than the $Ni^{2+}$-covered mesa, indicating a portion of the $Co^{2+}$ ions experience a spin crossover from low-spin to high-spin state. We notice that $\mu_{\text{eff}}$ of $Ni^{2+}$ is $\sim$ the average of the high-spin $\mu_{\text{eff}}$ and the low-spin $\mu_{\text{eff}}$ of $Co^{2+}$. Thereby, when most of the $Co^{2+}$ ions complete the spin

transition from low to high, the value of $\tau_s^{-1}$ for the $Co^{2+}$-covered mesa is anticipated to be $\tau_s^{-1}(Co^{2+})|_{\text{high-spin}} \sim 2\tau_s^{-1}(Ni^{2+}) - \tau_s^{-1}(Co^{2+})|_{\text{low-spin}} = 0.42$ ps$^{-1}$ if a linear relation between $\mu_{\text{eff}}$ and $\tau_s^{-1}$ is assumed. Figure 4.19 shows that $\tau_s^{-1}(Co^{2+}) = 0.41$ ps$^{-1}$ at $T = 6$ K, implying $\rho_H(6\text{ K}) \sim 100\%$.

Transitions from a low-spin to a high-spin state are due to an increase in the bond distances between the $Co^{2+}$ ion and the $NO_3^{-1}$ and $H_2O$ ligands, or between the metal cation and the substrate anions (here the surface electrons). There are two equilibrium distances for the bond, which result in two stable values for $\Delta_{OCT}$. The low-spin state has a smaller equilibrium distance, meaning a larger bond strength and a stronger crystal field ($\Delta_{OCT} > E_P$, low-spin). As $T$ increases, the metal-ligand bond distances increase, therefore the interaction between the $Co^{2+}$ ion and the ligand becomes weak, and so does the crystal field ($\Delta_{OCT} < E_P$, high-spin). The energy required for the transition between the two bonds must fall within a thermal range $k_B\Delta T$, where $\Delta T$ is the crossover window of the $Co^{2+}$ ion spin states. According to Fig. 4.19, $\Delta T \sim 6$ K $\rightarrow k_B\Delta T = 0.52$ meV. Assuming the molar fraction function of $Co^{2+}$ ions in its high-spin state can be written as

$$\rho_H(T) = \frac{1}{e^{\alpha(T_{1/2}-T)} + 1}, \tag{4.4}$$

where $\alpha$ is a fitting parameter and $T_{1/2}$ denotes the temperature for a coexistence of 50% of low-spin and 50% of high-spin $Co^{2+}$ ions, we can obtain the expression for the $T$ dependence of the spin-flip rate of the $Co^{2+}$-covered mesa [96] as

$$\tau_s^{-1}(T) = \tau_s^{-1}|_{\text{low-spin}} + \Delta\tau_{s,H-L}^{-1}\rho_H(T), \tag{4.5}$$

where $\Delta\tau_{s,H-L}^{-1} = \tau_s^{-1}|_{\text{high-spin}} - \tau_s^{-1}|_{\text{low-spin}}$.

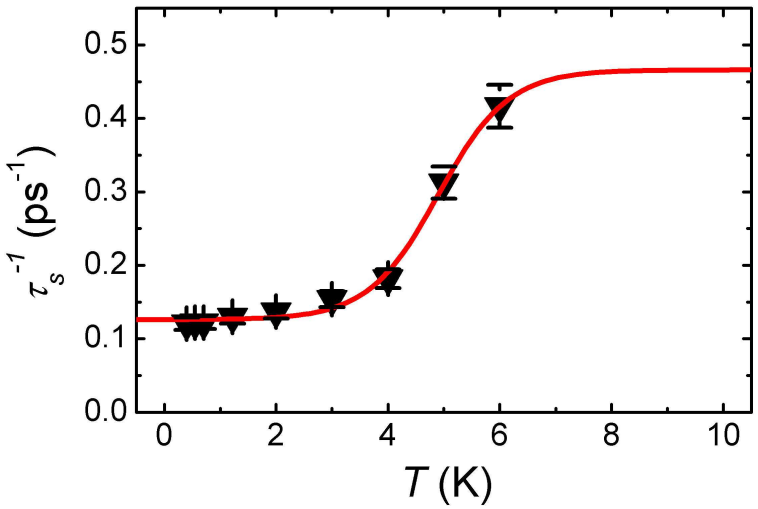


Figure 4.20: Simulation of $\tau_s^{-1}$ *vs* $T$. Down triangles are experiment data with error bars indicated. The red solid line is the theoretical fit.

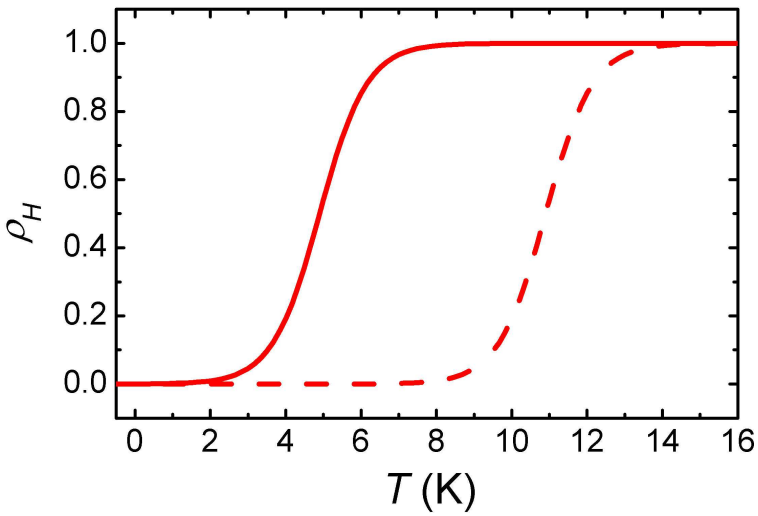


Figure 4.21: Theoretical calculation of the molar fraction of $Co^{2+}$ ions in high-spin state as a function of $T$ with $T$ varying from low to high (red solid line). Predicted $T$ dependence of the molar fraction when $T$ varies from high to low (red dashed line). Two curves form a thermal hysteresis loop.

Figure 4.20 demonstrates the fitting result of applying Eq. 4.5 to simulate the spin-flip rate data of the $Co^{2+}$-covered mesa. From the fitting $\alpha$, $T_{1/2}$, $\tau_s^{-1}|_{\mathrm{low-spin}}$, and $\Delta\tau_s^{-1}$ are derived to be 1.6 $K^{-1}$, 4.9 K, 0.13 $ps^{-1}$, and 0.34 $ps^{-1}$. Accordingly, the spin-flip rate in high-spin state is 0.47 $s^{-1}$, consistent with the expectation of $\tau_s^{-1}(Co^{2+})|_{\mathrm{high-spin}} = 0.42$ $ps^{-1}$ and the observed spin-flip rate of $Co^{2+}$ of 0.41 $ps^{-1}$ at 6 K. The agreement between experimental data and the theoretical calculation strongly suggests the existence of a spin transition. The plot of Eq. 4.4 is displayed in Fig. 4.21, indicating the fraction of $Co^{2+}$ ions that stay in the high-spin state. Normally, this spin crossover occurs with a thermal hysteresis [93, 94]. Our data is obtained with $T$ varying from 0.4 K to higher $T$. However, if another set of experiments are obtained with $T$ varying from high to low, we may attain another similar $T$ dependence of the molar fraction curve with $T_{1/2}$ shifted to higher $T$ as illustrated in Fig. 4.21. This is future work beyond the scope of this dissertation.

### 4.2.3 Spin-Glass System

Knowing that at low $T$ $Fe^{3+}$ is in its high-spin state and $Co^{2+}$ is in its low-spin state, the $S$, $L$ and $J$ of these TM ions in their ground state can be then determined as follows, following Hund's rules: $Ni^{2+}$ has $S = 1$, $L = 3$ and $J = 4$; $Co^{2+}$ has $S = \frac{1}{2}$, $L = 4$ and $J = \frac{9}{2}$; $Fe^{3+}$ has $S = \frac{5}{2}$, $L = 0$ and $J = \frac{5}{2}$. The 3d electrons are in the outermost shell, and thus unlikely to form a paramagnetic system. With an external magnetic field applied, the TM ions will spontaneously align or anti-align relative to $B$, resulting in ferromagnetic or antiferromagnetic systems. Paramagnetic behavior may be observed in ferromagnetic materials that are above their Curie temperature $T_C$, where thermal energy overcomes the interaction between the neighbouring spins [97]. However, $T_C$ of the materials studied in this thesis are far above the experiment temperature range (0.4 K $\sim$ 6 K). Consequently, we rule

out the presence of a paramagnetic system as a potential explanation for the $T$ dependence of $\tau_s^{-1}$ ($Co^{2+}$).

Spin-glasses can occur where the axes of the moments are distributed isotropically (Heisenberg spin-glass), or are aligned parallel or antiparallel (Ising spin-glass). Under the present case of strong spin-orbit scattering ($\tau_{SO}^{-1} \gtrsim \tau_i^{-1}$), both spin-glasses are predicted to lead to the same reduction in $\tau_s^{-1}$ by $S/(S+1)$ compared to the free-spin case [82, 20]. The smaller $S$ is, the more the scattering rate is reduced. There is a possibility for the magnetic moments of the TM ions to be locked to specific orientations by interaction with the substrate atoms, or by Rudermann-Kittel-Kasuya-Yosida (RKKY) interaction with each other [98, 99, 82, 100], leading to a spin-glass system with remanent magnetization, which in turn reduces the spin-flip scattering compared to a free-spin system. For the $Co^{2+}$ sample, the surface ions in the low-spin state yield $S = 1/2$, and hence the largest reduction of the magnetic scattering is 1/3 if free-spin and spin-glass are assumed at $T = 6$ K and 0.4 K respectively. When no external fields are applied, the magnetization of the spin glass is at its remanent value, which lowers the magnetic scattering. From Fig. 4.19, a saturation in $\tau_s^{-1} = 0.13$ ps$^{-1}$ is observed when $T$ is below 2 K, indicating a complete alignment due to spin-glass formation at this transition temperature. If the free-spin case occurs at higher $T$, the spin-flip rate is expected to be 0.39 ps$^{-1}$, consistent with $\tau_s^{-1} = 0.41$ ps$^{-1}$ at $T = 6$ K in Fig. 4.19. Another saturation of $\tau_s^{-1}$ is then anticipated above 6 K, demonstrated by the fitting curve in Fig. 4.20. Unfortunately, experimentally the AL signal is already quite small at 6 K (Fig. 4.14) and thus performing experiments at higher $T$ may not result in a sufficient signal to extract information. The consistency between the physics model of spin-glass and the simulation based on the experimental data of $\tau_s^{-1}$ provides us with yet another potential explanation to our observations.

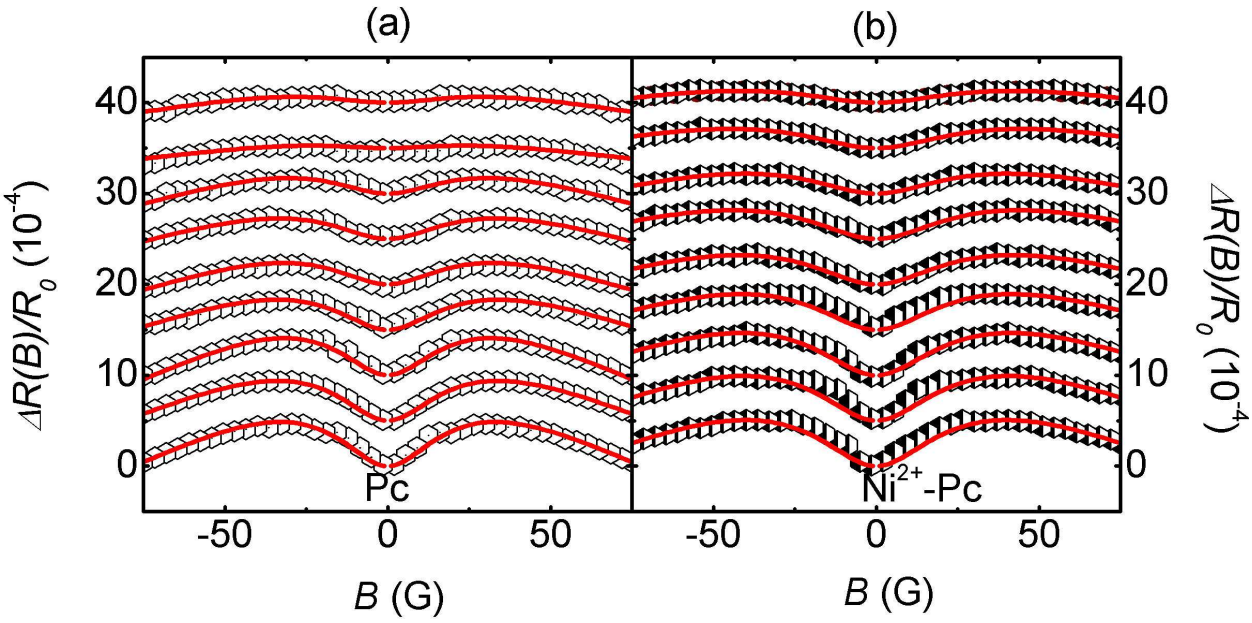


Figure 4.22: (a) Magnetoresistance due to AL on Pc-covered mesa and (b) on TM-Pc covered mesa, both of the $Ni^{2+}$-Pc sample at (from bottom to top) $T = 0.4$, 0.55, 0.7, 1.22, 2.0, 2.5, 3.0, 4.0, and 5.0 K (1 out of 6 experimental points are plotted, curves offset by $5.0\times10^{-4}$). Solid lines are theoretical fits.

So far, we propose two plausible explanations, spin-transition and spin-glass, to explain the $Co^{2+}$ behavior. Further experiments may differentiate between these two explanations.

## 4.3 Transition Metal Phthalocyanine Samples

TM-phthalocyanine compounds have TM ions sitting at the center of the organic Pc molecule, as seen in Fig. 4.5. The Pc molecule itself is almost flat, and consists of a conjugated aromatic tire. The TM cations nestle in the hole of the tire. In the case of the $Fe^{3+}$-Pc, the iron is further coordinated to a chloride ligand. The length of the Pc molecule is $\sim 1$ nm, and thus when TM-Pc molecules are deposited on a surface, the density of TM ions is less than when TM nitrate solution of same molarity are used. This reduction in effective TM ion areal

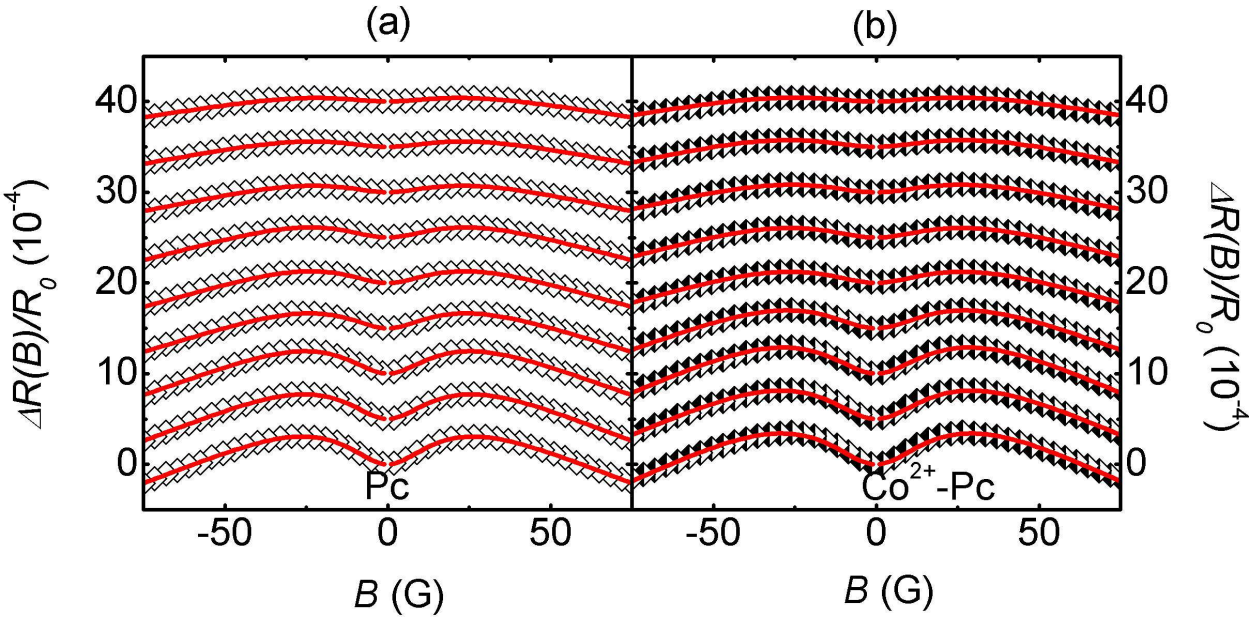


Figure 4.23: (a) Magnetoresistance due to AL on Pc-covered mesa and (b) on TM-Pc covered mesa, both of the $Co^{2+}$-Pc sample at (from bottom to top) $T = 0.4$, 0.55, 0.7, 1.22, 2.0, 2.5, 3.0, 4.0, and 5.0 K (1 out of 6 experimental points are plotted, curves offset by $5.0\times10^{-4}$). Solid lines are theoretical fits.

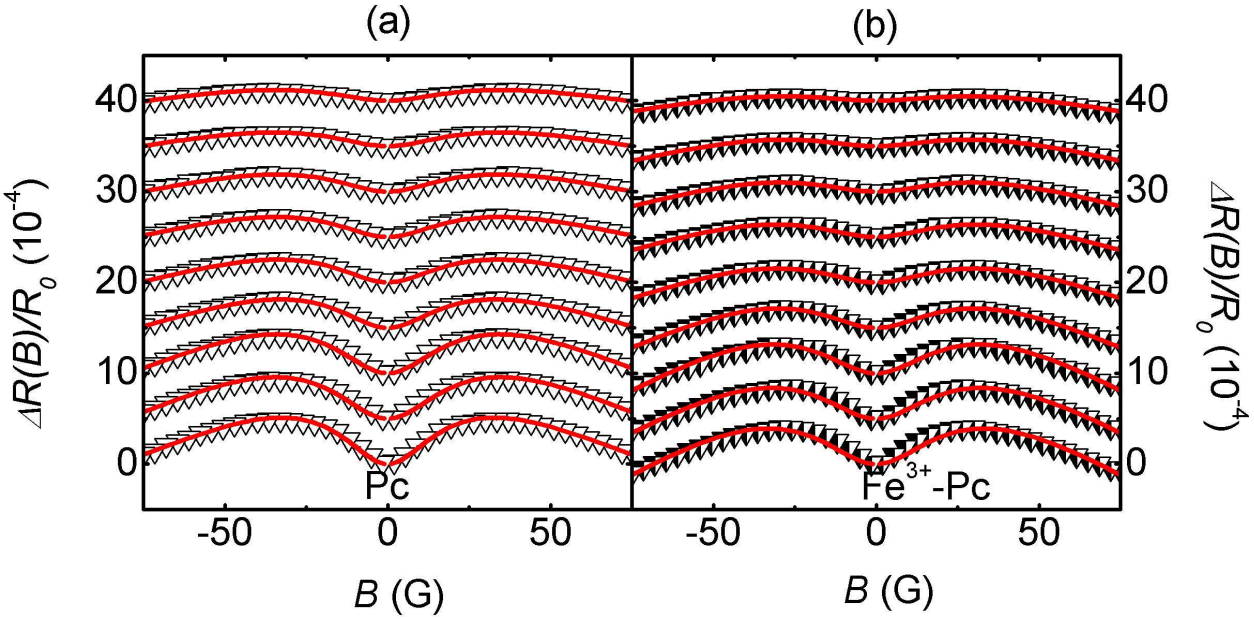


Figure 4.24: (a) Magnetoresistance due to AL on Pc-covered mesa and (b) on TM-Pc covered mesa, both of the $Fe^{3+}$-Pc sample at (from bottom to top) $T = 0.4$, 0.55, 0.7, 1.22, 2.0, 2.5, 3.0, 4.0, and 5.0 K (1 out of 6 experimental points are plotted, curves offset by $5.0\times10^{-4}$). Solid lines are theoretical fits.

density influences the AL signal. TM-Pc and Pc molecules lie $\sim$ flat on metallic surfaces [101]. The InAs surface here is metallic and thus our assumption that in our experiments the TM-Pcs are laying $\sim$ flat is reasonable. As these molecules are rigid, and the TM ions are strongly held in the hole of the Pc, the effective distance between the TMs and the surface is different than in the case of TM nitrate coverage. The effective TM areal density and the distance of the TM ions from the surface influence $\tau_{SO}^{-1}$ and $\tau_s^{-1}$.

The solubility of TM-Pcs in water is fairly low, nonetheless they can be dissolved in chloroform. Unlike other InAs samples where one serpentine was left bare, here, one mesa is covered with Pc, and the other with TM-Pc to exclude the effect of Pc molecules. We first inspect the MR data, as a function of $T$, for the $Ni^{2+}$-, $Co^{2+}$-, and $Fe^{3+}$-Pc samples, Figures 4.22, 4.23, and 4.24 respectively. We note that the value of $\Delta R(B)/R_0$ for each trace at 0.4 K (lowest traces in Figs. 4.22, 4.23, and 4.24) is the actual measured value, and the traces at the other higher $T$ are offset from the 0.4 K value for each TM-Pc sample. Looking closely at the 0.4 K traces, we notice that $Fe^{3+}$-Pc reduces the AL signal, indicating considerable spin-flip scattering. For both $Ni^{2+}$-Pc and $Co^{2+}$-Pc samples, $\tau_s^{-1}$ is negligible compared to $\tau_{SO}^{-1}$, so the increase in $\tau_{SO}^{-1}$ broadens the AL signal. The symmetry of the TM in the TM-Pc complexes, in a non–solvated or surface deposited situation, differs. In the case of an isolated $Ni^{2+}$- and $Co^{2+}$-Pc molecule, the metal center is in a square planar geometry (Fig. 4.28). This geometry may change upon solvation and proximity to a metallic surface. The $Fe^{3+}$-Pc is actually a chloride salt and the $Fe^{3+}$ center is in a square pyramidal geometry. The fifth bond to $Fe^{3+}$ changes the $\sim$ planar and flat TM-Pc complex to a 3-dimensional one, potentially affecting how the $Fe^{3+}$-Pc sits on the InAs surface; $\sim$ flat or as a top. The high spin-flip rate indicates stronger interactions between electrons and $Fe^{3+}$ ions than between electrons and $Co^{2+}$ ions or $Ni^{2+}$ ions (Fig. 4.27). Hence most $Fe^{3+}$-Pc molecules lie flat, otherwise the spin-flip rate would be smaller than that of the $Ni^{2+}$- and $Co^{2+}$-Pc samples because

of increased interacting distance (distance $\sim$ the fifth bond length). The decreased surface densities in these TM-Pc samples cause less modifications on the AL signals compared with the TM samples as displayed in Figs. 4.22, 4.23, and 4.24. Consistent with the TM samples, $Ni^{2+}$-Pc generates a stronger crystal field than $Co^{2+}$-Pc, and hence causes a slightly larger increase of the SOI, supported by a slightly more broadened AL signal (indicated in Figs. 4.22 and 4.23).

The linear $T$ dependence of $\tau_i^{-1}$ in Fig. 4.25 implies that the Nyquist mechanism is dominant in phase decoherence for the TM-Pc samples as well, consistent with the RE and the TM samples. Figure 4.26 shows that the increase of $\tau_{SO}^{-1}$ is scaled in the same manner as in the TM samples (Fig. 4.18), which can be explained by the varied strengths of the crystal fields from the TM ions. But, the magnitude of the increase for $\tau_{SO}^{-1}$ is not as much as in the TM samples, resulting from the different ion areal density and different interaction distance in the TM-Pc samples. The values of spin-flip rate are displayed in Fig. 4.27. As anticipated from the AL measurements, at $T = 0.4$ K, $\tau_s^{-1}(Fe^{3+}\text{-Pc}) \sim \tau_s^{-1}(Co^{2+})$, which is the only magnetic scattering compatible with the spin-orbit scattering among the three TM-Pc samples. Most of the spin-flip rates are $T$ independent in the presence of TM-Pc compounds except for the $Co^{2+}$-Pc sample which shows a slight increase in $\tau_s^{-1}$ as $T$ increases. Since the spin-flip rate correlates with the effective moment $\mu_{\text{eff}}$, we can deduce that the spin state of $Fe^{3+}$ is larger than that of $Co^{2+}$ and $Ni^{2+}$. We notice that while TM ions and the surrounding ligands form octahedral geometry, different geometries are followed by the TM-Pcs. $Ni^{2+}$-Pc and $Co^{2+}$-Pc are square planar complexes, where as $Fe^{3+}$-Pc is square pyramidal. Consequently the high-spin and low-spin states of the TM ions discussed in Sec 4.2.2 are changed due to the different geometries. In the case of square planar, the d shell electrons are more likely to pair up and occupy the lowest three energy levels indicated in Fig. 4.28. With the $d_{xy}$ level occupied by electrons, one for $Co^{2+}$ and two for $Ni^{2+}$, $Co^{2+}$-Pc has $S = 1/2$ and $Ni^{2+}$-Pc has

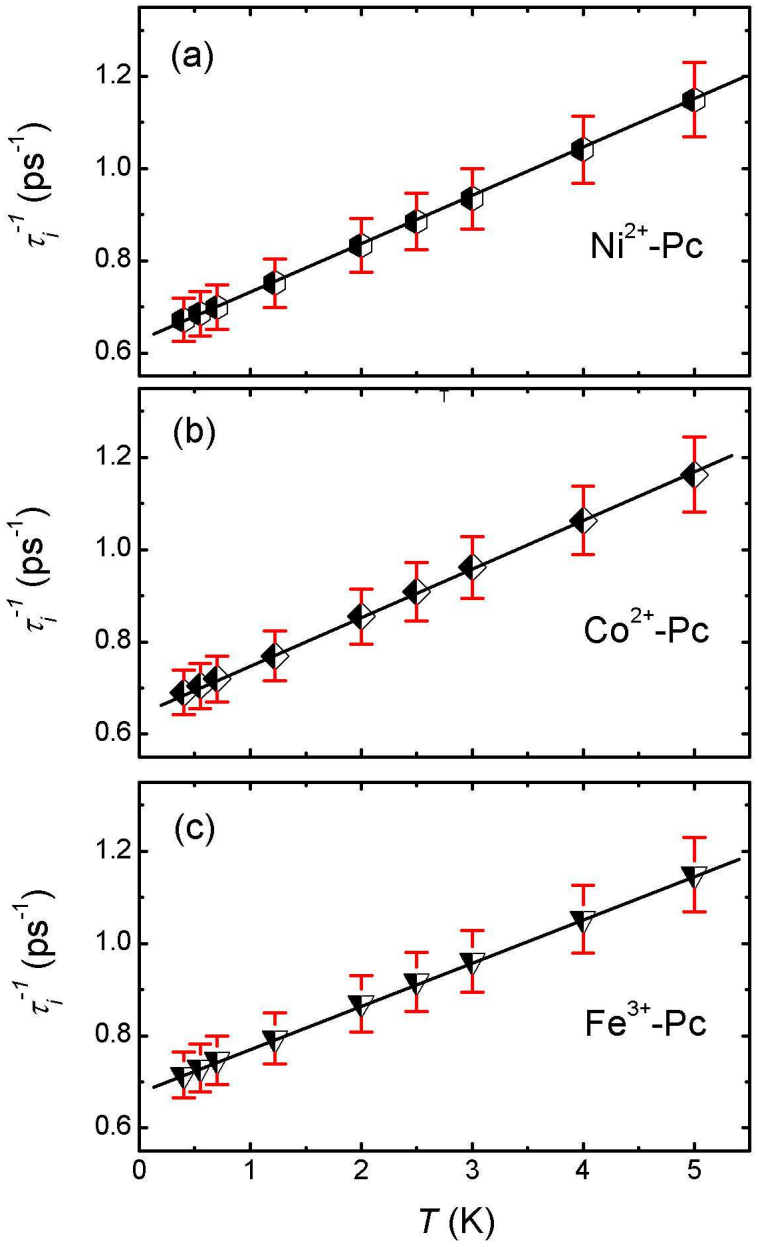


Figure 4.25: Inelastic scattering rates $\tau_i^{-1}$ *vs* $T$ for (a) $Ni^{2+}$-Pc(hexagons) sample; (b) $Co^{2+}$-Pc(diamonds) sample; (c) $Fe^{3+}$-Pc(down triangles) sample. The TM-Pc covered mesa and the Pc-covered mesa share the same value. Solid lines form guides to the eye. Error bars are indicated.

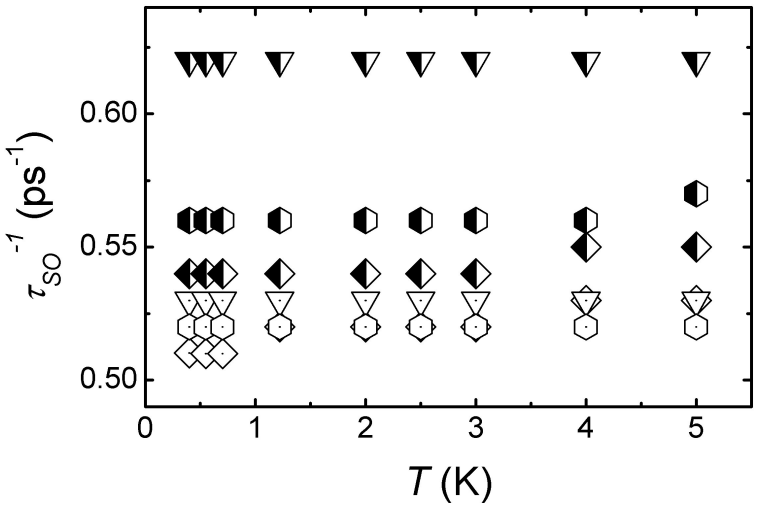


Figure 4.26: Spin-orbit scattering rates $\tau_{SO}^{-1}$ *vs* $T$ for the $Ni^{2+}$-Pc(hexagons) sample, the $Co^{2+}$-Pc(diamonds) sample, and the $Fe^{3+}$-Pc(down triangles) sample. In all the graphs half-solid symbols stand for the TM-Pc covered mesa; open symbols stand for the Pc-covered mesa. For clarity, 7% error bars are not indicated.

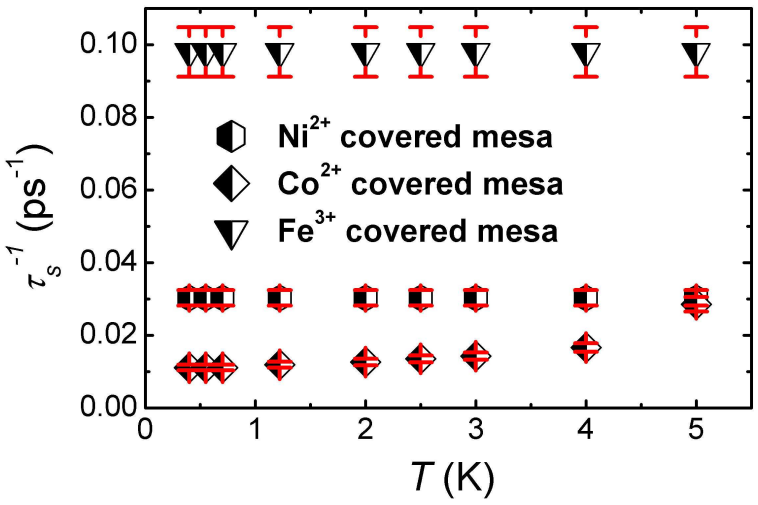


Figure 4.27: The spin-flip rate $\tau_s^{-1}$ of TM-Pc covered mesas *vs* $T$. Error bars are indicated.

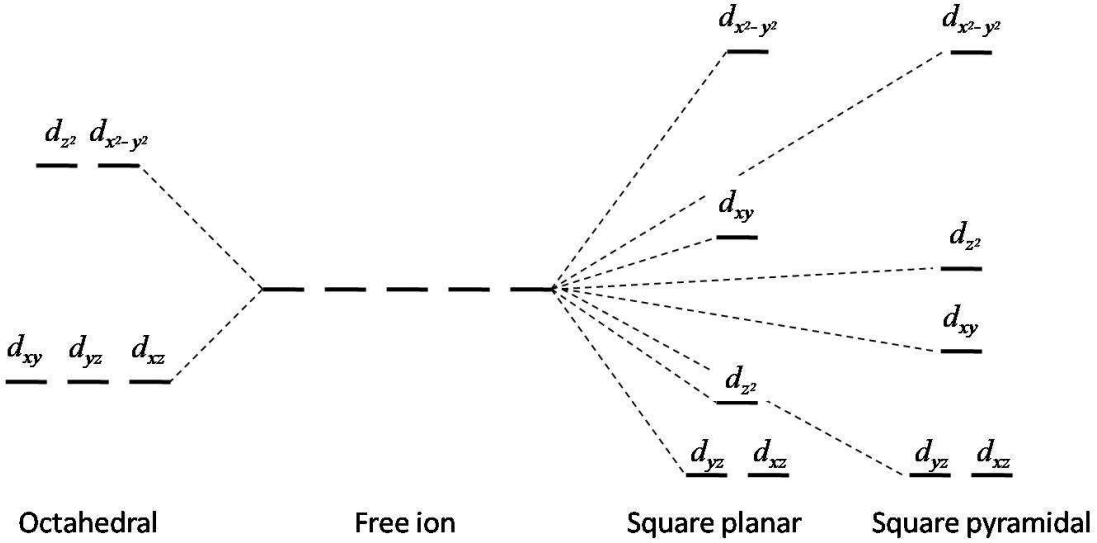


Figure 4.28: Energy level diagrams for octahedral, square planar, and square pyramidal complexes. Modified from Ref. [7].

$S = 0$. However, in square pyramidal complexes, the lowest four energy levels are close in energy as demonstrated in Fig. 4.28. As a result, the 5 d shell electrons of $Fe^{3+}$ will occupy different levels first, then start pairing up. Thus $Fe^{3+}$-Pc has a high spin state of $S = 3/2$. Spin states explained by the different geometries are consistent with the values of spin-flip rates shown in Fig. 4.27.

We notice that the variation of the AL signals between the Pc-covered and the TM-Pc covered mesas are less compared with the $Ni^{2+}$ and $Co^{2+}$ TM samples. As a result, the values of $\tau_s^{-1}/\Delta\tau_{SO}^{-1}$ of the TM-Pc samples are expected to fall in the range between 0.5 and 1.1. In fact $\tau_s^{-1}/\Delta\tau_{SO}^{-1}$ are calculated to be 1.05, 0.75, and 0.65 respectively for the $Fe^{3+}$-Pc, $Ni^{2+}$-Pc, and $Co^{2+}$-Pc samples based on the values in Figs. 4.26 and 4.27.

In a typical symmetrized AL signal, the maxima of MR, $\Delta R_{\max}$, occur at $B_{\max}$ as demonstrated in Fig. 4.29. We make the following two approximations. If the AL signal of the ion-covered mesa is increased compared to the mesa bare of ions $\dfrac{\Delta R_{\max}|_{cov}}{\Delta R_{\max}|_{bare}} > 1$, otherwise

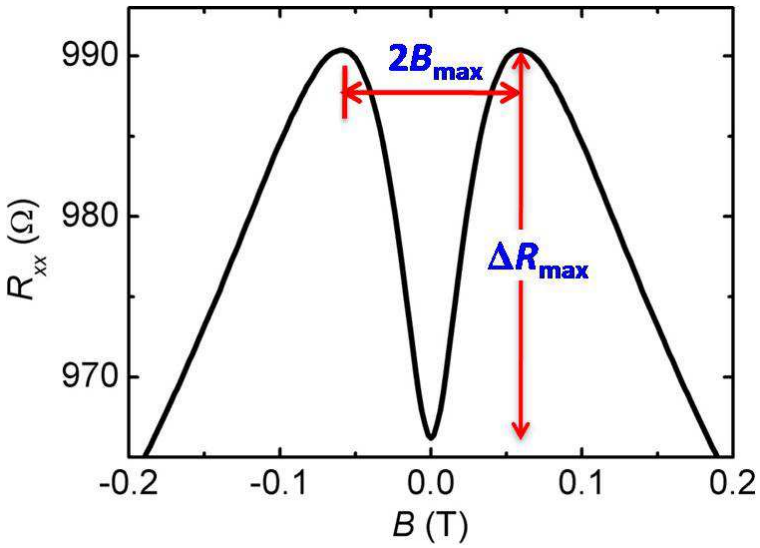


Figure 4.29: AL signal with parameters related with two local maxima.

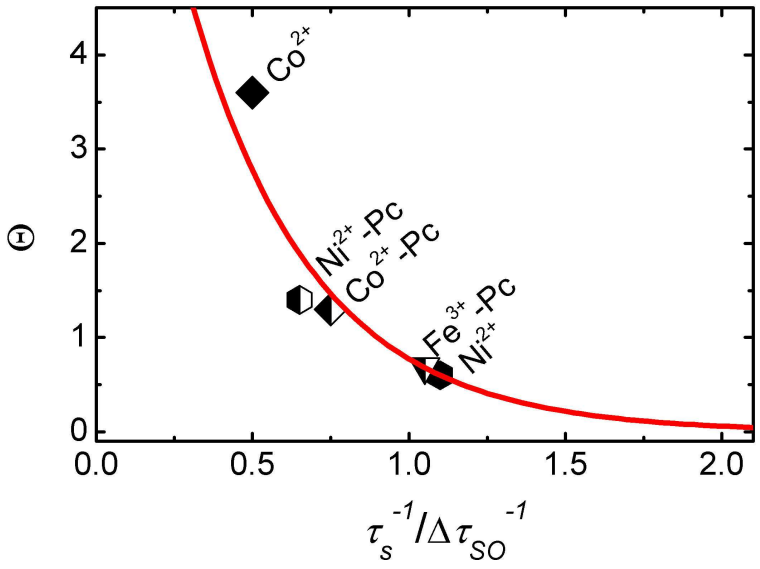


Figure 4.30: The increasing ratio of the AL signals due to the presence of TM ions *vs* $\tau_s^{-1}/\Delta\tau_{SO}^{-1}$ at $T = 0.4$ K. Each data point is from a different sample differentiated by the symbols: $Ni^{2+}$-Pc sample (half-solid hexagons), $Co^{2+}$-Pc sample (half-solid diamonds), $Fe^{3+}$-Pc sample (half-solid down trangles), $Ni^{2+}$ sample (solid hexagons), and $Co^{2+}$ sample (solid diamonds).

$\frac{\Delta R_{\max}|_{cov}}{\Delta R_{\max}|_{bare}} < 1$. And, $\frac{B_{\max}|_{cov}}{B_{\max}|_{bare}}$ determines whether the AL signal is broadened due the presence of ions. The product of the two ratios $\Theta$ describes the difference in the AL signal strengths caused by ions *vs* the bare mesa in a good manner as discussed below.

In order to compare the influence of TM and TM-Pc on the AL signal, we define $\Theta$ as

$$\Theta = \frac{(\Delta R_{\max} B_{\max})|_{\text{cov}}}{(\Delta R_{\max} B_{\max})|_{\text{bare}}}, \tag{4.6}$$

and are calculated to be 3.6, 1.4, 1.3, 0.69, 0.6 for the $Co^{2+}$, $Ni^{2+}$-Pc, $Co^{2+}$-Pc, $Fe^{3+}$-Pc, and $Ni^{2+}$ samples respectively. Figure 4.30 is a plot of $\Theta$ as function of $\tau_s^{-1}/\Delta\tau_{SO}^{-1}$. The data follows an exponential relation plotted as the red solid line in Fig. 4.30. The expression of the exponential relation is obtained from the fitting of the 5 data points in Fig. 4.30 as

$$\Theta = e^{-2.6\left(\frac{\tau_s^{-1}}{\Delta\tau_{SO}^{-1}} - 0.9\right)}, \tag{4.7}$$

where 2.6 and 0.9 are fitting parameters. Equation 4.7 indicates that $\Theta = 1$ when $\tau_s^{-1}/\Delta\tau_{SO}^{-1} = 0.9$. The surface magnetic impurities influence the surface electrons in two ways; increasing their spin-orbit scattering, and introducing magnetic scattering, which both in turn modify the shape of the AL signal. $\Delta\tau_{SO}^{-1}$ broadens and increases the signal, whereas $\tau_s^{-1}$ shrinks the signal. The inelastic scattering rate is set to be the same for both bare and ion-covered mesas. Thus the changes in the AL signal are only determined by $\Delta\tau_{SO}^{-1}$ and $\tau_s^{-1}$. The competition between $\Delta\tau_{SO}^{-1}$ and $\tau_s^{-1}$ determines whether the AL signal is strengthened or weakened in the presence of surface species. When $\Theta < 1$, the AL signal is reduced under the condition of $\tau_s^{-1} > 0.9\Delta\tau_{SO}^{-1}$. When $\Theta > 1$, the AL signal is enlarged, $\tau_s^{-1} < 0.9\Delta\tau_{SO}^{-1}$. The AL signal will be suppressed at $\Theta = 0$, which occurs for $\sim \tau_s^{-1}/\Delta\tau_{SO}^{-1} \geq 2.0$, consistent with the $Fe^{3+}$ sample, where $\tau_s^{-1}/\Delta\tau_{SO}^{-1} = 2.5$. We note that the values for $\Theta$ for the RE ions

(omitted from Figure 4.30) lie above that of $Co^{2+}$, and do fit the exponential curve shown in the figure. Equation 4.7 is only valid in the AL model applied within this thesis (Eq. 1.16); the fitting parameter 0.9 would change depending on the different theoretical model used.

## 4.4 Conclusion

The increased spin-orbit scattering and the induced spin-flip scattering due to deposited surface species are both observed for InAs accumulation layer electrons. A series of comparative antilocalization measurements are performed by using rare ions ($Sm^{3+}$, $Gd^{3+}$, and $Ho^{3+}$), transition metal ions ($Ni^{2+}$, $Co^{2+}$, and $Fe^{3+}$), or transition metal phthalocyanines ($Ni^{2+}$-, $Co^{2+}$-, and $Fe^{3+}$-phthalocyanine) as surface magnetic moments. The spin-orbit scattering is observed to be temperature independent and an increase was observed for all the magnetic species studied in this dissertation. The spin-flip scattering does not change as a function of temperature except for the $Ho^{3+}$ and $Co^{2+}$ samples. The spin-flip rate of the $Ho^{3+}$ sample correlates with the spin-orbit energy level structure and the magnetic moment of $Ho^{3+}$. For the $Co^{2+}$ sample, the data may be explained by spin crossover or by spin-glass phenomena; more experiments are required to differentiate between the two. The transition metal phthalocyanine samples show that the spin interactions also depend on the areal density of the deposited species and interaction distance between the species and the itinerant electrons. From the literature, other groups have only investigated how the shape of the AL signal is determined by the ratio of $\tau_i/\tau_{SO}$ and the magnitude of $\tau_{SO}$, omitting the contribution of the spin-flip rate $\tau_s$. In this dissertation, we include the influence of $\tau_s$ in our fits to our experimental data, resulting in a more refined and true interpretation of the AL signal.

# Chapter 5

# Conclusion

The spin-exchange mechanisms between electrons and local magnetic moments are crucial for both fundamental and applied physics in spintronics. The interaction determines the spin coherence time of the electrons, which is a key parameter for many spintronic devices such as spin-transfer torque magnetoresistive random-access memory, quantum computer, etc. In particular, the model of magnetic moments in proximity with a non-magnetic host has been widely studied in metal systems, and is being explored in emerging novel materials such as graphene and topological insulators. However, there is a lack of investigations about III-V semiconductors as host systems, and about low-dimensional systems. In this thesis, we carefully characterized the interactions between surface magnetic species and two different two-dimensional electron systems, an $In_{0.53}Ga_{0.47}As$ quantum well and a InAs surface accumulation layer. The variations of the quantum properties related with electron spins, due to the presence of the magnetic impurities, are successfully probed by comparative antilocalization measurements. These low-temperature (between 0.4 K and 6 K) measurements are performed in a $^3$He cryostat with lock-in techniques and applied external magnetic fields.

Concerning the two-dimensional antilocalization theoretical model, we adopt the expression developed by Hikami, Larkin, and Nagaoka [11]. The surface magnetic moments affect the itinerant electrons by increasing spin-orbit scattering and inducing spin-flip scattering, which together determine the spin coherence time. The spin-orbit scattering correlates with the spin-orbit interaction, and its increase results from the electric fields generated by surface species. The spin-flip scattering originates from scattering of conduction electrons off magnetic impurities, and scales with their effective moments. Relatively speaking, the spin-flip scattering of electrons requires a close proximity to the species, and decreases more rapidly than the spin-orbit scattering as distance increases.

In the case of the InGaAs quantum well, an array of $Co_{0.6}Fe_{0.4}$ nanopillars were deposited on the surface of the InGaAs/InAlAs heterostructure as surface magnetic moments. Since the QW is buried inside the heterostructure, the magnetic scattering is repressed by the distance between the quantum well and the surface. Only an increase of the spin-orbit scattering is observed. Another control sample with Al nanopillars deposited on top indicates that the system follows the Elliott-Yafet spin-orbit decoherence mechanism. Therefore, the increased spin-orbit interaction can be explained by the fluctuation from the spatially varying fringing fields produced by CoFe nanopillars. This pseudorandom field model is in analogy to the Elliott-Yafet spin-orbit scattering. In addition, the fringing field also generates an average field at the quantum well. The average fringing field is due to both the low coercive field and the high saturation magnetization of the CoFe nanopillars. The value of $\sim$ 35 G of the average field can be derived from the data analysis, in a good agreement with a simple micromagnetic simulation.

For the InAs samples, rare earth ions ($Sm^{3+}$, $Gd^{3+}$, and $Ho^{3+}$), transition metal ions ($Ni^{2+}$, $Co^{2+}$, and $Fe^{3+}$), and transition metal phthalocyanines ($Ni^{2+}$-, $Co^{2+}$-, and $Fe^{3+}$-

phthalocyanine) are used as surface magnetic moments. The species are in direct contact with the surface accumulation layer, hence increasing spin-flip scattering. For all the species, the spin-orbit scattering is observed to increase. Reductions of both the spin-flip rate and the spin-orbit scattering rate are detected in the transition metal phthalocyanine samples compared with the transition metal ions samples, possibly due to the increased interacting distance caused by the phthalocyanine molecules. Within the experiment temperature range, the spin-orbit scatterings are almost temperature-independent, with a slight increase as temperature increases. In the case of the spin-flip rate, most of the surface species induce a temperature-independent scattering rate except $Ho^{3+}$ and $Co^{2+}$. $Ho^{3+}$ yields spin-flip rate proportional to the square root of temperature, which has been observed in Kondo systems before. However in our case, the observed temperature dependence is due to the non-zero orbital number and the large effective moment. The orbital number provides closely spaced energy levels of spin-orbit multiplets. The transition between these energy levels stimulated by thermal energy causes spin-flips due to the large effective moment. The spin-flip scattering caused by $Co^{2+}$ transits from a low saturation value to a high saturation value as temperature increases. The transition can be explained by the spin crossover from the low-spin to the high-spin state for $Co^{2+}$, or by a transition from a spin-glass to a free-spin system.

# Bibliography


[1] N. Grote, M. Möhrle, and W. Hofmann. Laser components. In *Fibre optic communication (2012)*, pages 99–137. Springer Berlin Heidelberg, Berlin, Germany.

[2] C. W. J. Beenakker and H. van Houten. Quantum transport in semiconductor nanostructures. *Solid State Phys.*, 44:1, 1991.

[3] G. Bergmann. Physical interpretation of weak localization: A time-of-flight experiment with conduction electrons. *Phys. Rev. B*, 28:2914, 1983.

[4] Yao Zhang and J. J. Heremans. Effects of ferromagnetic nanopillars on spin coherence in an InGaAs quantum well. *Solid State Commun.*, 177:36, 2014.

[5] Yao Zhang, V. Soghomonian, R. L. Kallaher, and J. J. Heremans. Antilocalization sensing of interactions between two-dimensional electrons and surface species. *Chin. Sci. Bull.*, 59:133, 2014.

[6] Yao Zhang, R. L. Kallaher, V. Soghomonian, and J. J. Heremans. Measurement by antilocalization of interactions between InAs surface electrons and magnetic surface species. *Phys. Rev. B*, 87:054430, 2013.

[7] E. Crabb, E. Moore, and L. Smart. *Concepts in transition metal chemistry.* The Open University, Cambridge, England, 2010.

[8] B. Crothers. End of Moore's Law: It's not just about physics. . http://www.cnet.com/news/end-of-moores-law-its-not-just-about-physics/.

[9] D. E. Nikonov and I. A. Young. Overview of beyond-CMOS devices and a uniform methodology for their benchmarking. *Proc. IEEE*, 101, 2013.

[10] I. Žutić, J. Fabian, and S. Das Sarma. Spintronics: Fundamentals and applications. *Rev. Mod. Phys.*, 76:323, 2004.

[11] S. Hikami, A. I. Larkin, and Y. Nagaoka. Spin-orbit interaction and magnetoresistance in the two dimensional random system. *Prog. Theor. Phys*, 63:707, 1980.

[12] G. Bergmann. Weak localization in thin films: a time-of-flight experiment with conduction electrons. *Phys. Rep.*, 107:1, 1984.

[13] S. McPhail, C. E. Yasin, A. R. Hamilton, M. Y. Simmons, E. H. Linfield, M. Pepper, and D. A. Ritchie. Weak localization in high-quality two-dimensional systems. *Phys. Rev. B*, 70:245311, 2004.

[14] W. Wei and G. Bergmann. CuCo: A new surface Kondo system. *Phys. Rev. B*, 37:5990, 1988.

[15] H. He, G. Wang, T. Zhang, I. Sou, G. K. L Wong, J. Wang, H. Lu, S. Shen, and F. Zhang. Impurity effect on weak antilocalization in the topological insulator $Bi_2Te_3$. *Phys. Rev. Lett.*, 106:166805, 2011.

[16] H. Lu, J. Shi, and S. Shen. Competition between weak localization and antilocalization in topological surface states. *Phys. Rev. Lett.*, 107:076801, 2011.

[17] T. Gang, M. Deniz Yilmaz, D. Atac, S. K. Bose, E. Strambini, A. H. Velders, M. P. de Jong, J. Huskens, and W. G. van der Wiel. Tunable doping of a metal with molecular spins. *Nat. Nanotechnol.*, 7:232, 2012.

[18] G. Bergmann. Magnetic screening of Fe impurities in Mg. *Phys. Rev. Lett.*, 57:1460, 1986.

[19] R. P. Peters, G. Bergmann, and R. M. Mueller. Kondo maximum of magnetic scattering. *Phys. Rev. Lett.*, 58:1964, 1987.

[20] R. P. Peters, G. Bergmann, and R. M. Mueller. Quenching of interacting moments and anomalous Fermi-liquid behavior in disordered Kondo alloys at low temperatures. *Phys. Rev. Lett.*, 60:1093, 1988.

[21] M. Liu, J. Zhang, C. Chang, Z. Zhang, X. Feng, K. Li, K. He, L. Wang, X. Chen, X. Dai, Z. Fang, Q. Xue, X. Ma, and Y. Wang. Crossover between weak antilocalization and weak localization in a magnetically doped topological insulator. *Phys. Rev. Lett.*, 108:036805, 2012.

[22] M. Z. Hasan and C. L. Kane. *Colloquium*: Topological insulators. *Rev. Mod. Phys.*, 82:3045, 2010.

[23] H. Zhu, C. A. Richter, E. Zhao, J. E. Bonevich, W. A. Kimes, H. Jang, H. Yuan, H. Li, A. Arab, O. Kirillov, J. E. Maslar, D. E. Ioannou, and Q. Li. Topological insulator $Bi_2Se_3$ nanowire high performance field-effect transistors. *Sci. Rep.*, 3:1757, 2013.

[24] Yao Zhang, R. L. Kallaher, J. J. Heremans, and V. Soghomonian. Spin interactions between InAs two-dimensional surface electrons and local magnetic moments determined by antilocalization measurements. *AIP Conf. Proc.*, 1416:168, 2011.

[25] D. C. Tsui. Landau-level spectra of conduction electrons at an InAs surface. *Phys. Rev. B*, 12:5739, 1975.

[26] M. Noguchi, K. Hirakawa, and T. Ikoma. Intrinsic electron accumulation layers on reconstructed clean InAs(100) surfaces. *Phys. Rev. Lett.*, 66:2243, 1991.

[27] L. Ö. Olsson, C. B. M. Andersson, M. C. Håkansson, J. Kanski, L. Ilver, and U. O. Karlsson. Charge accumulation at InAs surfaces. *Phys. Rev. Lett.*, 76:3626, 1996.

[28] T. D. Veal and C. F. McConville. Profiling of electron accumulation layers in the near-surface region of InAs (110). *Phys. Rev. B*, 64:085311, 2001.

[29] L. F. J. Piper, T. D. Veal, M. J. Lowe, and C. F. McConville. Electron depletion at InAs free surfaces: Doping-induced acceptorlike gap states. *Phys. Rev. B*, 73:195321, 2006.

[30] T. Mochizuki, R. Masutomi, and T. Okamoto. Evidence for two-dimensional spin-glass ordering in submonolayer Fe films on cleaved InAs surfaces. *Phys. Rev. Lett.*, 101:267204, 2008.

[31] C. Schierholz, T. Matsuyama, U. Merkt, and G. Meier. Weak localization and spin splitting in inversion layers on $p$-type InAs. *Phys. Rev. B*, 70:233311, 2004.

[32] H. H. Wieder. Transport coefficients of InAs epilayers. *Appl. Phys. Lett.*, 25:206, 1974.

[33] D. A. Anderson L. L. Taylor M. J. Kane, N. Apsley and T. Kerr. Parallel conduction in GaAs/$Al_xGa_{1-x}$As modulation doped heterojunctions. *J. Phys. C: Solid State Phys.*, 18:5629, 1985.

[34] IQE. Official website of IQE company. http://www.iqep.com/.

[35] N. Miura. *Physics of semiconductors in high magnetic fields*. Oxford University Press, New York, NY, 2008.

[36] S. Datta. *Electronic transport in mesoscopic systems*. Cambridge University Press, Cambridge, England, 1995.

[37] S. Chakravarty and A. Schmid. Weak localization: The quasiclassical theory of electrons in a random potential. *Phys. Rep.*, 140:193, 1986.

[38] T. Tsuzuki. Log E dependence of the conductivity in a two-dimensional random system. *Physica B+C*, 107:679, 1981.

[39] R. G. Wheeler, K. K. Choi, A. Goel, R. Wisnieff, and D. E. Prober. Localization and electron-electron interaction effects in submicron-width inversion layers. *Phys. Rev. Lett.*, 49:1674, 1982.

[40] C. W. J. Beenakker and H. van Houten. Boundary scattering and weak localization of electrons in a magnetic field. *Phys. Rev. B*, 38:3232, 1988.

[41] K. K. Choi, D. C. Tsui, and K. Alavi. Dephasing time and one-dimensional localization of two-dimensional electrons in GaAs/$Al_xGa_{1-x}As$ heterostructures. *Phys. Rev. B*, 36:7751, 1987.

[42] M. Kohda, T. Bergsten, and J. Nitta. Manipulating spinorbit interaction in semiconductors. *J. Phys. Soc. Jpn.*, 77:031008, 2008.

[43] B. L. Altshuler, D. Khmel'nitzkii, A. I. Larkin, and P. A. Lee. Magnetoresistance and hall effect in a disordered two-dimensional electron gas. *Phys. Rev. B*, 22:5142, 1980.

[44] R. S. Markiewicz and C. J. Rollins. Localization and electron-interaction effects in a two-dimensional metal with strong spin-orbit scattering: Pd films. *Phys. Rev. B*, 29:735, 1984.

[45] H. Rauch, A. Zeilinger, G. Badurek, and A. Wilfing. Verification of coherent spinor rotation of fermions. *Phys. Lett. A*, 54:425, 1975.

[46] S. V. Iordanskii, Yu. B. Lyanda-Geller, and G. E. Pikus. Weak localization in quantum wells with spin-orbit interaction. *Pisma Zh. Eksp. Teor. Fiz.*, 60:199, 1994.

[47] C. Van Haesendonck, J. Vranken, and Y. Bruynseraede. Resonant kondo scattering of weakly localized electrons. *Phys. Rev. Lett.*, 58:1968, 1987.

[48] J. C. Licini, G. J. Dolan, and D. J. Bishop. Weakly localized behavior in quasi-one-dimensional li films. *Phys. Rev. Lett.*, 54:1585, 1985.

[49] W. Zawadzki and B. Lax. Two-band model for Bloch electrons in crossed electric and magnetic fields. *Phys. Rev. Lett.*, 16:1001, 1966.

[50] W. Zawadzki, S. Klahn, and U. Merkt. Semirelativistic behavior of electrons in InSb in crossed magnetic and electric fields. *Phys. Rev. Lett.*, 55:983, 1985.

[51] W. Zawadzki. Zitterbewegung and its effects on electrons in semiconductors. *Phys. Rev. B*, 72:085217, 2005.

[52] E. O. Kane. Band structure of indium antimonide. *J. Phys. Chem. Solids.*, 1:249, 1957.

[53] J. H. Davies. *The physics of low-dimensional semiconductors: An introduction.* Cambridge University Press, New York, NY, 1997.

[54] Ioffe Physical Technical Institute. InAs electrical properties . http://www.ioffe.ru/SVA/NSM/Semicond/InAs/electric.html.

[55] S. A. Wolf, Lu J., M. R. Stan, E. Chen, and D. M. Treger. The promise of nanomagnetics and spintronics for future logic and universal memory. *Proc. IEEE*, 98:2155, 2010.

[56] T. Matsuoka, E. Kobayashi, K. Taniguchi, C. Hamaguchi, and S. Sasa. Temperature dependence of electron mobility in InGaAs/InAlAs heterostructures. *Jap. J. Appl. Phys.*, 29:2017, 1990.

[57] E. Diez, Y. P. Chen, S. Avesque, M. Hilke, E. Peled, D. Shahar, J. M. Cerveró, Sivco D. L., and A. Y. Cho. Two-dimensional electron gas in InGaAs/InAlAs quantum wells . *Appl. Phys. Lett.*, 88:052107, 2006.

[58] R. J. Elliott. Theory of the effect of spin-orbit coupling on magnetic resonance in some semiconductors. *Phys. Rev.*, 96:266, 1954.

[59] Y. Yafet. *Solid State Physics*. Vol. 14 ed. by F. Seitz and D. Turnbull, Academic, New York, NY, 1963.

[60] B. L. Altshuler, A. G. Aronov, and D. E. Khmelnitsky. Effects of electron-electron collisions with small energy transfers on quantum localisation. *J. Phys. C: Solid State Phys.*, 15:7367, 1982.

[61] R. L. Kallaher and J. J. Heremans. Spin and phase coherence measured by antilocalization in $n$-InSb thin films. *Phys. Rev. B*, 79:075322, 2009.

[62] P. H. Song and K. W. Kim. Spin relaxation of conduction electrons in bulk III-V semiconductors. *Phys. Rev. B*, 66:035207, 2002.

[63] J. N. Chazalviel. Spin relaxation of conduction electrons in $n$-type indium antimonide at low temperature. *Phys. Rev. B*, 11:1555, 1975.

[64] M. M. Glazov, E. Ya. Sherman, and V. K. Dugaev. Two-dimensional electron gas with spinorbit coupling disorder. *Physica E*, 42:2157, 2010.

[65] D. J. Monsma and S. S. P. Parkin. Spin polarization of tunneling current from ferromagnet/$Al_2O_3$ interfaces using copper-doped aluminum superconducting films. *Appl. Phys. Lett.*, 77:720, 2000.

[66] D. V. Berkov, C. T. Boone, and I. N. Krivorotov. Micromagnetic simulations of magnetization dynamics in a nanowire induced by a spin-polarized current injected via a point contact. *Phys. Rev. B*, 83:054420, 2011.

[67] R.M. Bozorth. *Ferromagnetism*. IEEE Press, Piscataway, NJ, 1993.

[68] T. P. Pareek and P. Bruno. Spin coherence in a two-dimensional electron gas with Rashba spin-orbit interaction. *Phys. Rev. B*, 65:241305, 2002.

[69] M. I. D'yakonov and V. I. Perel. On spin orientation of electrons in interband absorption of light in semiconductors. *Sov. Phys. JETP*, 33:1053, 1971.

[70] B. G. Wybourne. *Spectroscopic properties of rare earths*. Interscience, New York, NY, 1965.

[71] C. Kittel. *Introduction to solid state physics*. John Wiley & Sons, Inc, Hoboken, NJ, 2005.

[72] J. J. Lin and J. P. Bird. Recent experimental studies of electron dephasing in metal and semiconductor mesoscopic structures. *J. Phys.: Condens. Matter*, 14:R501, 2002.

[73] J. Rammer and A. Schmid. Destruction of phase coherence by electron-phonon interactions in disordered conductors. *Phys. Rev. B*, 34:1352, 1986.

[74] D. Belitz and M. N. Wybourne. Eliashberg function of amorphous metals. *Phys. Rev. B*, 51:689, 1995.

[75] D. Belitz and K. I. Wysokinski. Electronic inelastic lifetime near a mobility edge. *Phys. Rev. B*, 36:9333, 1987.

[76] A. Kaminski and L. I. Glazman. Electron energy relaxation in the presence of magnetic impurities. *Phys. Rev. Lett.*, 86:2400, 2001.

[77] G. Göppert and H. Grabert. Nonequilibrium electron distribution in the presence of kondo impurities. *Phys. Rev. B*, 64:033301, 2001.

[78] Y. Imry. *Introduction to mesoscopic physics*. Oxford University Press, New York, NY, 1997.

[79] D. E. Beutler and N. Giordano. Localization and electron-electron interaction effects in thin Bi wires and films. *Phys. Rev. B*, 38:8, 1988.

[80] C. Weeks, J. Hu, J. Alicea, M. Franz, and R. Wu. Engineering a robust 1uantum spin Hall state in graphene via adatom deposition. *Phys. Rev. X*, 1:021001, 2011.

[81] P. W. Atkins and R. S. Friedman. *Molecular quantum mechanics*. Oxford University Press, New York, NY, 1999.

[82] W. Wei, G. Bergmann, and R. Peters. Weak localization in spin-glass systems. *Phys. Rev. B*, 38:11751, 1988.

[83] R. Schäfer and G. Bergmann. Effects of ferromagnetic nanopillars on spin coherence in an InGaAs quantum well. *Solid State Commun.*, 98:45, 1996.

[84] G. M. Alzoubi and N. O. Birge. Phase coherence of conduction electrons below the Kondo temperature. *Phys. Rev. Lett.*, 97:226803, 2006.

[85] F. Mallet, J. Ericsson, D. Mailly, S. Ünlübayir, D. Reuter, A. Melnikov, A. D. Wieck, T. Micklitz, A. Rosch, T. A. Costi, L. Saminadayar, and C. Bäuerle. Scaling of the low-temperature dephasing rate in Kondo systems. *Phys. Rev. Lett.*, 97:226804, 2006.

[86] G. H. Dieke and H. M. Crosswhite. The spectra of the doubly and triply ionized rare earths. *Appl. Opt.*, 2:675, 1963.

[87] B. R. Judd. The structures of the ground multiplets of certain rare-earth ions. *Proc. Phys. Soc. A*, 69:157, 1956.

[88] D. St. P. Bunbury, C. Carboni, and M. A. H. McCausland. Field dependence of the hyperfine splitting of holmium in holmium hydroxide. *J. Phys.: Condens. Matter*, 1:1309, 1989.

[89] B. G. Wybourne. Nuclear moments and intermediate coupling. *J. Chem. Phys.*, 37:1807, 1962.

[90] G. H. Dieke and L. A. Hall. Fluorescent lifetimes of rare earth salts and ruby. *J. Chem. Phys.*, 27:465, 1957.

[91] J. Pelzl, S. Hfner, and S. Scheller. Hyperfine structure in holmium ethylsulfate and holmium trichloride. *Z. Phys.*, 231:377, 1970.

[92] F. de Groot. Multiplet effects in X-ray spectroscopy. *Coord. Chem. Rev.*, 249:31, 2005.

[93] O. Kahn and C. J. Martinez. Spin-transition polymers: From molecular materials toward memorydevices. *Science*, 279:44, 1998.

[94] C. L. Zilverentanta, G. A. van Albadaa, A. Bousseksoub, J. G. Haasnoota, and J. Reedijka. Infrared detection of the hysteresis in the thermally induced spin-crossover in bis(4,4-bis-1,2,4-triazole)bis(thiocyanato-N)iron(II) monohydrate. *Inorg. Chim. Acta.*, 303:287, 2000.

[95] J. Tuchagues, A. Bousseksou, Gábor Molnár, J. J. McGarvey, and F. Varret. The role of molecular vibrations in the spin crossover phenomenon. *Top. Curr. Chem.*, 235:85, 2004.

[96] C. P. Slichter and H. G. Drickamer. Pressure-induced electronic changes in compounds of iron. *J. Chem. Phys.*, 56:2142, 1972.

[97] S. W. Biernacki. Ferromagnetic-paramagnetic phase transition in manganite perovskites: Thermal hysteresis. *Phys. Rev. B*, 68:174417, 2003.

[98] L. Zhou, J. Wiebe, S. Lounis, E. Vedmedenko, F. Meier, S. Blügel, P.H. Dederichs, and R. Wiesendanger. Strength and directionality of surface Ruderman-Kittel-Kasuya-Yosida interaction mapped on the atomic scale. *Nat. Phys.*, 6:187, 2010.

[99] M. A. Ruderman and C. Kittel. Indirect exchange coupling of nuclear magnetic moments by conduction electrons. *Phys. Rev.*, 96:99, 1954.

[100] J. J. Zhu, D. X. Yao, S. C. Zhang, and K. Chang. Electrically controllable surface magnetism on the surface of topological insulators. *Phys. Rev. Lett.*, 106:097201, 2011.

[101] Y. Wang, K. Wu, J. Kröger, and R. Berndt. Review Article: Structures of phthalocyanine molecules on surfaces studied by STM. *AIP Adv.*, 2:041402, 2012.